Steam Reforming and Oxidative Steam Reforming of Isobutanol Over Supported Metal Catalysts

A Thesis Submitted to
Indian Institute of Technology Hyderabad
In Partial Fulfillment of the Requirements for
The Degree of

Doctor of Philosophy
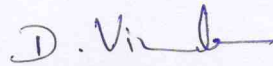
By

Vimala Dhanala

Roll No. CH10P010

Department of Chemical Engineering

December 2014

Declaration

I declare that this written submission represents my ideas in my own words, and where other's ideas or words have been included, I have adequately cited and referenced the original sources. I also declare that I have adhered to all principles of academic honesty and integrity and have not misrepresented or fabricated or falsified any idea/data/fact/source in my submission. I understand that any violation of the above will be a cause for disciplinary action by the Institute and can also evoke penal action from the sources that have thus not been properly cited, or from whom proper permission has not been taken when needed.
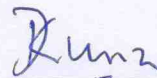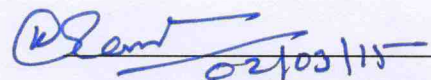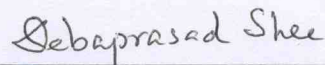

Vimala Dhanala

Roll No.: CH10P010

Approval Sheet

This thesis entitled Steam Reforming and Oxidative Steam Reforming of Isobutanol Over Supported Metal Catalysts by Vimala Dhanala is approved for the degree of Doctor of Philosophy from IIT Hyderabad.

Prof. Deepak Kunzru
Department of Chemical Engineering
Indian Institute of Technology
Kanpur 208016, India
External Examiner

Prof. K. K. Pant
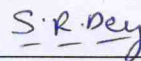Department of Chemical Engineering
Indian Institute of Technology Delhi
Hauz Khas, New Delhi INDIA 110016
External Examiner

Dr. Debaprasad Shee
Department of Chemical Engineering, IIT Hyderabad
Internal Examiner

Dr. Sunil Kumar Maity
Department of Chemical Engineering, IIT Hyderabad
Adviser

Dr. Suhash Ranjan Dey
Department of Materials Science and Metallurgical Engineering, IIT Hyderabad
Chairman

Acknowledgements

First and foremost, I take this opportunity to express my sincere gratitude for the contribution made by my advisor Dr. Sunil Kumar Maity. I would like to thank him for giving me such an interesting research topic to work on, freedom to explore on my own, and at the same time guidance which led me to the right way when my steps faltered. This thesis would not have been possible without his motivation, aspiring guidance, invaluably constructive criticism and friendly advice during the course of my work. I appreciate the time he spent reviewing my work, his continuous support and valuable suggestions. I am so delighted for the opportunity to work with him and to learn many things from him. I would like to thank Dr. Debaprasad Shee for collaborating with us and grateful to him for his fruitful discussions and sharing truthful and illuminating views on a number of issues in implementation of the work.

I am also indebted to my doctoral committee members - Dr. Saptarshi Majumdar, Dr. Debaprasad Shee, and Dr. Suhash Ranjan Dey for their brilliant comments and invaluable suggestions throughout my research work. I thank previous and present head of the department, Dr. Vinod Janardhanan and Dr. Kirti Chandra Sahu and every faculty member of chemical engineering department for their constant encouragement in every possible way. I am very much thankful to my institute, Indian Institute of Technology Hyderabad and the Director, Prof. U.B Desai, for providing good research facilities despite all problems involved in a temporary campus. I thank MHRD for providing scholarship during my PhD and IITH for granting financial aid to attend the national and international conferences.

My group mates Vishnu, Chandrashekar, Sudhakar, Pankaj, Anup, and other colleagues, Hari kishan, Ravikumar, Srinivas, Lakshmi, Bala Raju, Teja are very cooperative and supportive. I am very much thankful to them. I owe my gratitude to all my friends Prasanna, Anusha, Vandana, Vasavi, Anitha, Dayamani, Unnisa, Vijaya, Meenakshi, Deepika and Asha kumari because of whom my experience at IITH has been one that I will cherish forever. I thank each and every staff members of the institute - administration, academics, accounts, stores, library, hostel staff,

security, care takers, warden, bus and cab drivers etc. for their service to achieve smooth, secured, and peaceful stay at IIT Hyderabad.

I would be very happy to acknowledge my beloved father and husband, for their moral support, love and constant encouragement to complete my PhD work. I am extremely grateful to my father and mother for everything that they have made on my behalf and I would like to express heartfelt thanks to my husband for his cooperation in finishing my PhD and for being such a best half always cheering me up. Last, but not the least, none of this would have been possible without my family members who have been the constant source of love, concern, support and strength all these years. I appreciate the generosity and understanding of my extended family that has been aided and encouraged me throughout this endeavor.

Dedicated to

My parents

Venkateshwarlu Dhanala and Padmavathi Dhanala

&

My husband

Lepakshi Chowdary Medasani

Synopsis

The human civilization is deeply reliant on fossil fuels to meet societal needs of energy and organic chemicals. The fossil fuels reserves are however diminishing continuously to meet growing demands of energy and organic chemicals of the world's mounting population with improved standards of living. The increased usages of fossil fuels have also vast impact on earth environment due to emissions of greenhouse gases (CO_2 and CH_4) which are responsible for global warming. Therefore, there is a strong need of finding carbon-neutral renewable resources for sustainable production of energy and organic chemicals while preserving earth environment. In recent times, the bio-*n*-butanol has been received widespread attention as bio-fuel because of its superior fuel qualities over biodiesel and bio-ethanol. The isobutanol having lesser toxicity and higher octane number compared to *n*-butanol and same essential fuel potentials as *n*-butanol is deliberated as one of the promising bio-fuels of the future. Once bio-butanols based biorefinery is realized successfully, novel methods of production of synthesis gas (SG) must also be established from bio-butanols. Apprehending tremendous upcoming prospective of bio-butanols based biorefinery, present work initiated to explore experimental and thermodynamic investigation on steam reforming (SR) and oxidative steam reforming (OSR) of isobutanol over supported metal catalysts for production of SG. The SG finds wide ranges of applications in chemical industries, for example, manufacture of hydrogen, ammonia, fertilizers, methanol, and dimethyl ether by Fischer-Tropsch synthesis (FTS). SG also provides a source of highly pure hydrogen for fuel cell applications to generate electric power in an environmentally cleaner manner.

The present works provide (a) a comprehensive structure-activity relationship of various inexpensive transition metals (nickel, cobalt, and molybdenum) and role of supports (γ-Al_2O_3, SiO_2, and ZrO_2) for SR of isobutanol, (b) a systematic investigation of effects of various process parameters on SG composition for SR of isobutanol over γ-Al_2O_3 supported nickel and cobalt catalysts of varying nickel and cobalt contents respectively, (c) detailed study on OSR of

isobutanol over γ-Al_2O_3 supported nickel catalysts, (d) authentication of experimental SR and OSR data with equilibrium products composition, and (e) an understanding of roles of metals and supports on nature of coke formation on spent catalysts and chemical transformation of catalysts during SR and OSR.

The supported metal catalysts were prepared by incipient wetness impregnation method and reduced in-situ prior to the reaction. The surface area (SA), metal dispersion (MD), crystalline phase, and reducibility of the prepared catalysts were determined using BET, chemisorption, powder XRD, and TPR respectively. Furthermore, spent catalysts were characterized by FESEM, powder XRD, and FTIR to elucidate roles of metals and supports on natures of coke formed and chemical transformation of the catalysts during SR and OSR. The SR and OSR were carried out in a down-flow stainless steel fixed-bed reactor (FBR). The products were quantified by gas chromatography (GC) and identified by GC equipped with a mass spectrometer (MS) detector. H_2, CO, CO_2, and CH_4 were observed as gaseous products. Acetaldehyde, propionaldehyde, isobutyraldehyde, 2-propenal, 2-butanone, 1-butanol, 2-butanol, and unreacted isobutanol were identified as products in liquid samples.

The activity of the supported metal catalysts, xMS (x=mmol metal; M=Ni, Co, and Mo; S= Al, Si, and Zr for γ-Al_2O_3, SiO_2, and ZrO_2 respectively) was strongly related to metal-support interactions as reflected by their MD, metal crystallite size, and extents of bulk metal/metal oxides. The catalytic activity increased in the order of 4.3NiZr<4.3NiSi<4.3NiAl and 4.3MoAl<4.3CoAl<4.3NiAl. The shape and quantity of carbon formed on spent catalysts depends strongly on nature of metals. The powder XRD patterns of spent catalysts showed that cobalt and molybdenum transformed to oxides form during SR of isobutanol.

γ-Al_2O_3 supported nickel and cobalt catalysts showed promising catalytic activity for SR of isobutanol. Therefore, effects of various process parameters were further investigated over xNiAl (x=1.9 to 5.7 mmol) (10 to 25 wt%) and xCoAl (x=3.0-7.3 mmol) (15 to 30 wt%) catalysts. The time-on-stream (TOS) study showed that the catalysts remained fairly stable for more than 10 h of TOS. The carbon conversion to gaseous products (CCGP) increased with increasing nickel and

cobalt loading on γ-Al$_2$O$_3$ and temperature and decreasing weight hourly space velocity (WHSV). The hydrogen yield enhanced with increasing temperature and steam-to-carbon mole ratio (SCMR) with concurrent decrease of selectivity to methane. The selectivity to CO declined with increasing SCMR and decreasing temperature.

A systematic investigation of OSR and comparisons with SR of isobutanol over γ-Al$_2$O$_3$ supported nickel catalysts were also carried out for several oxygen-to-carbon mole ratios (OCMR). The hydrogen yield and selectivity to CO and methane dropped steadily with increasing OCMR. The hydrogen yield enhanced and selectivity to methane reduced with increasing temperature and SCMR for both SR and OSR. The selectivity to CO increased with increasing temperature and decreased with increasing SCMR. The hydrogen yield and selectivity to CO and methane were however somewhat lesser for OSR compared to SR. The H$_2$/CO mole ratio in the range of 8-10 was observed under the experimental conditions. The powder XRD patterns of spent catalysts exhibited oxidation of nickel to nickel oxide during OSR. The FESEM images of spent catalysts showed that diameter of carbon nano-fibers reduced with increasing OCMR.

Thermodynamic equilibrium analysis is a valuable tool to foresee viability of process, effects of process parameters on equilibrium products composition, and thermodynamically favourable and optimum operating conditions of the process. Apprehending importance, thermodynamic equilibrium analysis of SR and OSR of isobutanol was carried out under the experimental conditions using Aspen Plus. The experimental results were then compared with equilibrium products composition. The trends of experimental results matched reasonably well with equilibrium products compositions.

Refereed publications

1. Vimala Dhanala, Sunil K. Maity, Debaprasad Shee, Steam Reforming of Isobutanol for Production of Synthesis Gas over Ni/γ-Al$_2$O$_3$ Catalysts. *RSC Advances 3 (2013) 24521-24529*.

2. Vimala Dhanala, Sunil K. Maity, Debaprasad Shee, Oxidative Steam Reforming of Isobutanol over Ni/γ-Al$_2$O$_3$ Catalysts: A Comparison with Thermodynamic Equilibrium Analysis. *Journal of Industrial and Engineering Chemistry (2014). Accepted*

3. Vimala Dhanala, Sunil K. Maity, Debaprasad Shee, Performance of Metals (Ni, Co, Mo) and Roles of Supports (γ-Al$_2$O$_3$, SiO$_2$, ZrO$_2$) for Steam Reforming of Isobutanol. *International Journal of Hydrogen Energy (Under review)*.

Conferences

1. Vimala Dhanala, Sunil K. Maity, Debaprasad Shee, Vinod M. Janardhanan, Steam Reforming of Isobutanol for the Production of Synthesis Gas over Ni/Al$_2$O$_3$ Catalyst. CHEMCON 2012, Dr. B.R. Ambedkar National Institute of Technology, Punjab, India, 27th -30th December, 2012.

2. Vimala Dhanala, Sunil K. Maity, Debaprasad Shee, Steam Reforming of Isobutanol for the Production of Synthesis Gas: Effects of metals, World Congress on Petro Chemistry and Chemical Engineering, Hilton San Antonio Airport, Texas, USA, 18th -20th November, 2013.

3. Vimala Dhanala, Sunil K. Maity, Debaprasad Shee, Cobalt supported γ-Al$_2$O$_3$ catalyst for steam reforming of isobutanol for production of synthesis gas. Seventh Tokyo Conference on Advanced Catalytic Science and Technology (TOCAT7), Kyoto, Japan. June 1-6, 2014.

4. Vimala Dhanala, Sunil K. Maity, Debaprasad Shee, Oxidative Steam Reforming of Isobutanol over Ni/Al$_2$O$_3$ Catalysts. CHEMCON 2014, Chandigarh regional center, Indian Institute of Chemical Engineers, Chandigarh, India, 27th -30th December, 2014 (*Accepted*).

Nomenclature

ΔH_r	standard heat of reaction at 298 K, kJ mol^{-1}
a_{ik}	number of atoms of the kth element present in each molecule of species i
A_k	total mass of kth element in the feed
f_i	fugacity of species i
f_i^0	standard state fugacity of species i
G^t	total Gibbs free energy
G_i^0	standard Gibbs free energy of species i
$\bar{G}_{c(g)}$	partial molar Gibbs free energy of gaseous carbon
$\bar{G}_{c(s)}$	partial molar Gibbs free energy of solid carbon
$G_{c(s)}$	molar Gibbs free energy of solid carbon
$\Delta G_{f_i}^0$	standard Gibbs free energy of formation of species i
$\Delta G_{f_{c(s)}}^0$	standard Gibbs free energy of formation of solid carbon
n_c	moles of carbon
n_i	number of moles of species i
N	number of species
P	pressure
P^0	standard state pressure of 101.3 kPa
R	molar gas constant, J mol^{-1} K^{-1}
T	temperature, K
y_i	mole fraction of species i in gaseous products
μ_i	chemical potential of species i
λ_k	Lagrange multiplier
φ_i	fugacity coefficient of species i

Abbreviations

ABE	Acetone-Butanol-Ethanol
ATSR	autothermal steam reforming
BET	Brunauer–Emmett–Teller
CBE	carbon balance error, %
CCGP	carbon conversion to gaseous products, %
d_c	crystallite size, nm
DR	dry reforming
EDX	energy dispersive X-Ray
FBR	fixed-bed reactor
FESEM	field emission scanning electron microscopy
FTIR	Fourier transform infrared spectroscopy
FWHM	full width half maximum
MD	metal dispersion, %
OSR	oxidative steam reforming
PO	partial oxidation
PV	pore volume, $cm^3 \, g^{-1}$
SA	BET surface area, $m^2 \, g^{-1}$
SCMR	steam-to-carbon mole ratio
OCMR	oxygen-to-carbon mole ratio
SESR	sorption enhanced steam reforming
SM	metallic surface area, $m^2 \, (g \, metal)^{-1}$
SOFC	solid oxide fuel cell
SR	steam reforming
T_{max}	maximum reduction temperature, K
TOS	time-on-stream, min
TPR	temperature programmed reduction
WGSR	water gas shift reaction
WHSV	weight hourly space velocity, h^{-1}
XRD	X-ray diffraction

List of Figures

List of Tables

Contents

Chapter 1

Introduction

1.1   Background

The energy and chemicals security of the globe is extremely important for sustainability of human civilization. At present, the human civilization is deeply reliant on fossil fuels (petroleum, coal, and natural gas) to meet social needs of energy and organic chemicals. At the moment, more than 80% of energy and greater than 90% of organic chemicals of the world are met through fossil fuels alone [1]. The fossil fuels resources are however diminishing continuously to fulfill growing energy and chemicals demands of the world's rising population with improved standards of living. The increased usage of fossil fuels also has a vast impact on the earth's environment because of the emission of harmful and greenhouse gases (CO_2 and CH_4) which are responsible for global warming. Continuous decline of fossil fuels reserves, escalation of crude oils price, and degradation of environmental cleanliness due to large scale usage of fossil fuels forced to explore carbon-neutral renewable resources of energy and organic chemicals.

Therefore, shifting dependency away from finite fossil fuels to carbon-neutral renewable resources like biomass is highly essential for sustainability of human civilization as a whole while maintaining environmental cleanliness. In principle, the biomass being origin of fossil fuels has tremendous potentials of replacing fossil fuels to meet societal needs of both fuels and organic chemicals if technological advancement results competitive production costs. At present, ~10% of total energy or ~50% of renewable energy comes from biomass alone. Therefore, new manufacturing concepts are continuously emerging for manufacture of assembly of bio-fuels and organic chemicals from biomass using complex processing technologies similar to today's integrated petroleum refinery and petrochemical industries commonly known as biorefinery [1–3].

(1)

1.1.1 Importance of bio-butanol

With outstanding efforts of researchers throughout the world, bio-ethanol and biodiesel have been emerged as two promising bio-fuels with properties suitable for blending with petroleum derived fuels to limited extents. In recent times, bio-butanol has been received renewed attention as bio-fuel due to its superior fuel qualities over bio-ethanol and biodiesel such as compatibility with existing internal combustion engines, lesser miscibility with water, lesser vapor pressure, octane rating similar to gasoline (RON=96 and MON=78), higher energy density, and better blending ability with gasoline (Table 1.1) [3-6]. Isobutanol, having lesser toxicity and higher octane number compared to n-butanol and the same essential fuel potential as n-butanol, is considered as one of the promising bio-fuels of the future. Moreover, butanols have wide ranges of potentials as solvent, derivatives, and petrochemical feedstock to fulfill goals of integrated biorefinery (Figure 1.1) [4]. Once bio-butanols based biorefinery is realized successfully, novel methods of production of synthesis gas (SG) from bio-butanols must also be streamlined for shifting dependency away from fossil fuels. Apprehending tremendous upcoming prospects of bio-butanols based biorefinery, present work was initiated on production of SG from isobutanol.

Table 1.1: Comparisons of physicochemical properties of bio-butanol and bio-ethanol with gasoline [5,6].

Properties	Bio-butanol	Bio-ethanol	Gasoline
Caloric value (MJ/kg)	32.5	26.8	42.9
Air–fuel ratio	11.2	9	14.6
Heat of vaporization (MJ/kg)	0.43	0.92	0.36
Research octane number	96	129	91–99
Motor octane number	78	102	81–89
Solubility in water	Immiscible	Miscible	Immiscible

1.1.2 Applications of synthesis gas

SG is a key petrochemical building block chemical for manufacture of extensive ranges of fuels and organic chemicals (Figure 1.2). It is mainly used as raw material for manufacture of hydrogen, ammonia, fertilizers, methanol, and dimethyl ether. SG also provides a source of

highly pure hydrogen for fuel cell applications to generate electric power in an environmentally cleaner manner. SG is generally produced by steam reforming (SR) of fossil fuels derived hydrocarbons such as naphtha and natural gas. With scarcity of crude oils, the novel methods of production of SG from carbon-neutral renewable resources such as biomass must be established. The gasification is a potential thermochemical process for direct conversion of lignocellulosic biomass into SG. However, excessive formation of tars and methane, gigantic size of plant with huge capital investments, and non-concentric nature of biomass make integrated technology of biomass gasification and biomass-to-liquid economically impractical [7]. The reforming of biomass derived oxygenated compounds including bio-oils, bio-ethanol, and bio-butanols are another promising approach for production of SG.
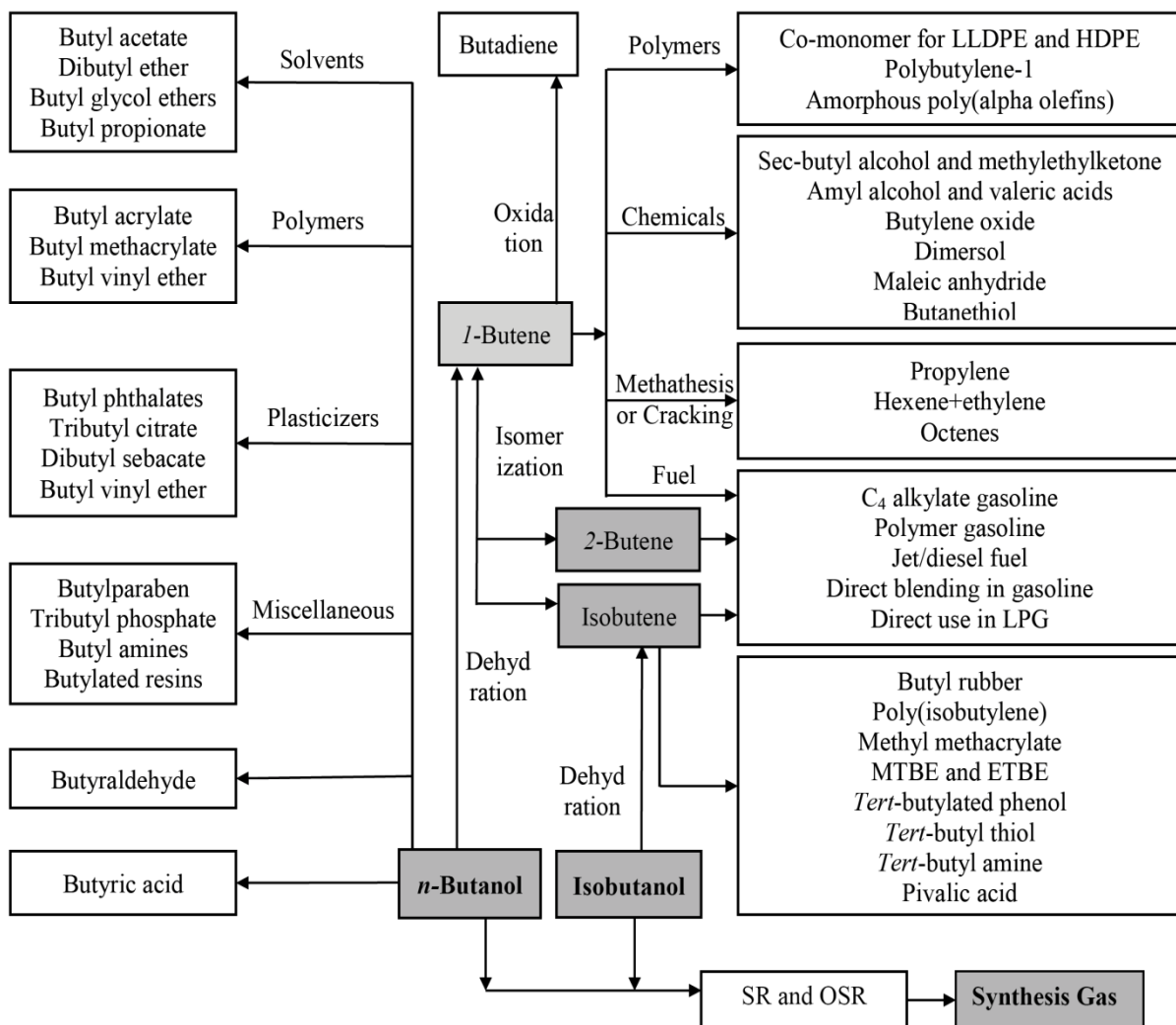
Figure 1.1: Derivative potentials for butanols [8].

SR and partial oxidation (PO) are two possible approaches for production of SG from butanols. SR is however accompanied with external supply of huge quantities heat energy to supplement endothermic reactions. The problem of external heat supply can be circumvented by exothermic PO of butanols. The technology of PO however suffers from drawbacks of low hydrogen yield and H_2/CO mole ratio compared to SR. The oxidative steam reforming (OSR) using sub-stoichiometric level of oxygen is an attractive alternative where exothermic PO reactions provide necessary heat energy for endothermic SR reactions. Moreover, SG obtained from OSR can be used either directly in high temperature fuel cell such as SOFC or in PEM fuel cell for mobile applications after significant reduction of CO below 10 ppm (by membrane coupled reformer or WGS reactor followed by a COPROX reactor) to overcome poisoning of platinum catalyst. Apprehending tremendous upcoming prospective of bio-butanols based biorefinery, present work was initiated on SR and OSR of isobutanol for production of SG.
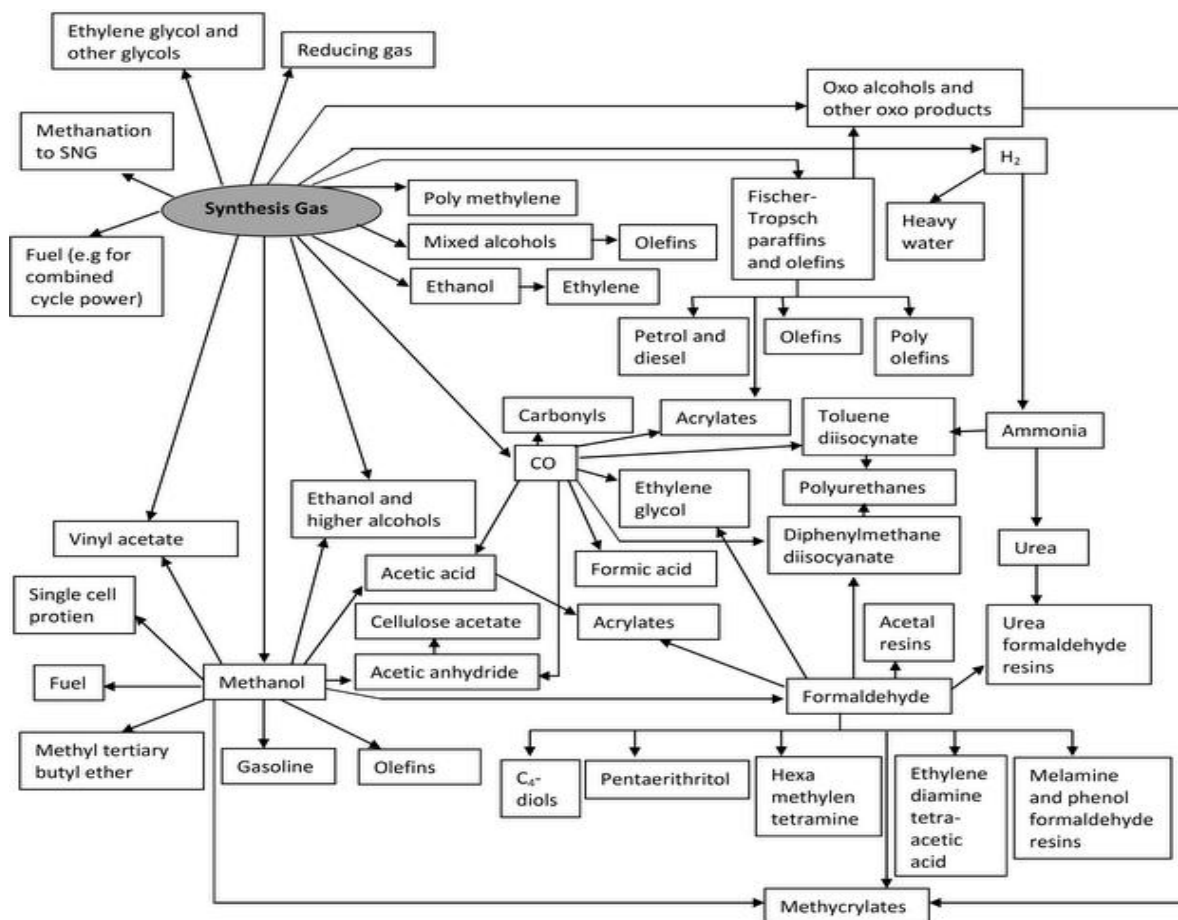
Figure 1.2: Potential avenues of synthesis gas [9].

(4)

1.2   Literature review

1.2.1   Production of bio-butanol by ABE (Acetone-Butanol-Ethanol) fermentation

ABE (Acetone-Butanol-Ethanol) fermentation was first developed by the chemist Chaim Weizmann. The process is similar to traditional yeast fermentation of sugars to ethanol. In 2005, David Ramey first drove his unmodified car across USA fuelled exclusively by n-butanol. Since then bio-butanols have attracted renewed attention as bio-fuel due to its superior fuel qualities over ethanol and biodiesel. The bio-butanol is produced by ABE fermentation of carbohydrates using *Clostridium acetobutylicum.* The process produces n-butanol, acetone, and ethanol in the ratio of 6:3:1. ABE fermentation was used primarily to produce acetone during World War I. Since 1950's, the production of butanol by ABE fermentation declined because of excessive cost of production compared to petrochemical route. The current industrial production of butanol is based on hydroformylation of fossil fuels derived propylene (oxo process) with H_2 and CO over rhodium catalyst to yield butyraldehyde which is subsequently hydrogenated to butanol. In response to the rising cost of crude oils in recent times, the ABE fermentation has been gaining renewed interest [8,10].

The ABE fermentation is usually carried out in a series of batch fermenters (residence time up to 21 days) with periodic addition of seed culture forming acetone, *n*-butanol, and ethanol. Typical solvent concentration in ABE fermentation broth is ~20 kg m^{-3} from 55-60 kg m^{-3} of substrate with butanol concentration of ~13 kg m^{-3} and products yields of ~0.35 kg kg^{-1} of sugar. The hydrogen produced as by-product (typically about $1/10^{th}$ of mass of butanol) in ABE fermentation can be used to generate heat and power or as renewable chemical feedstock. The excessive costs of sugar and starchy biomass, products inhibition of fermenting microorganisms, and energy intensive products recovery are key bottlenecks for commercialization of ABE fermentation. The products inhibition of fermenting microorganisms results low butanol titer in the fermentation broth. Low butanol titer forces reduced sugars loadings and increased water usage which in turn results large processing volumes. The microorganisms with improved solvent titers and butanol-to-solvent ratio, cheap product recovery techniques (e.g. adsorption, gas stripping, liquid–liquid extraction, pervaporation, aqueous two-phase separation, supercritical extraction etc.), and in-situ product removal methods to alleviate end product tolerance will enable ABE fermentation economically feasible in near future.

1.2.2 Importance of Bio-isobutanol as a biofuel

Nowadays bio-isobutanol has been considered as the promising biofuel because of much lower Reid vapor pressure (RVP), about a 30% higher energy content than bio-ethanol [4,11,12]. Moreover, the properties of bio-isobutanol are quite similar to gasoline that allows it's blending with gasoline and/or can replace the gasoline. It is also used as the feed stock to make other transportation fuels (e.g., iso-paraffinic kerosene for use as bio-jet) or other renewable products (e.g., renewable heating oil). It is used as solvent (in paints) and can be converted into materials such as butyl rubber, paraxylene (PX) and other derivatives for use in market applications such as tires, plastic bottles, carpets and clothing by dehydration of isobutanol. Bio-isobutanol can be produced by process of fermentation paired with an integrated separation technology. Fermentation process to isobutanol is almost similar to the current ethanol fermentation process. Traditional yeasts have been modified through biochemistry and microbiology to get higher yields of isobutanol in fermentation process. Moreover, bio-ethanol plants can be retrofitted to fermentation to isobutanol with minor modifications and can have a cost effective fuels value chain. In May 2012, the world's first commercial, bio-based isobutanol production plant was started in Luverne, Minnesota, with a capacity of 18 MMgpy (Million gallon per year). As bio isobutanol has many advantages, the production of synthesis gas from isobutanol has been explored in the present work to achieve goals of integrated biorefinery.

1.2.3 Reforming of oxygenated hydrocarbons

The SR of various oxygenated hydrocarbons derived from biomass such as ethanol [13–36], methanol [37–46], acetic acid [47–53], ethylene glycol [54], dimethyl ether [55], acetol [56], m-cresol [57], acetone, ethyl acetate, m-xylene, glucose [58], glycerol [59,60], fatty acids [61] and vegetable oils [62,63] has been investigated extensively in the past using numerous types of supported metal catalysts in the wide ranges of temperature.

1.2.4 Thermodynamic equilibrium analysis

Thermodynamic equilibrium analysis is a valuable tool to foresee viability of the process, effects of various process parameters on equilibrium products composition, and thermodynamically favourable and optimum operating conditions of the process.

(6)

Apprehending importance, substantial studies have also been devoted to the thermodynamic equilibrium analysis of SR [64], dry reforming (DR) [65], sorption enhanced steam reforming (SESR) (in which CaO or $LiSiO_4$ are used as the CO_2 adsorbents for CO_2 removal from the product gas) [66,67], and PO [68] of butanols to predict equilibrium products composition, elucidate the effect of various process parameters, and recognize the thermodynamically favourable and optimum operating conditions of the process.

Silva and Müller [66] reported thermodynamic equilibrium analysis of SESR and SR of butanol with and without CaO as CO_2 adsorbent. The H_2, CO, CH_4, CO_2 and C (graphite) were considered as products at equilibrium. The highest concentration of H_2 was 68-71 mol% at 973 K in SR. Whereas high purity hydrogen (>97%) was obtained in SESR at 723-873 K and steam-to-carbon ratio of 12:1. Wang and Cao [68] carried out thermodynamic analysis of PO of butanol. The optimized condition for PO of butanol was reported as oxygen-to-carbon mole ratio (OCMR) of 1.6-1.7 and 1115-1200 K at atmospheric pressure. The work was extended to SESR for various calcium oxide to carbon ratios. About 97% pure hydrogen was achieved at the optimized conditions: 800 K and atmospheric pressure with steam-to-carbon ratio of 10, and calcium oxide to carbon ratio of 8 [67]. Wang further extended the thermodynamic analysis to DR of butanol for the production of hydrogen [65]. The optimum conditions were 1150-1200K, 1 bar, and CO_2 to butanol ratio = 3.5-4. SG with 34-37% of H_2 and 57% CO was obtained under optimum conditions.

1.2.5 SR and OSR of butanols

Limited experimental studies are available in open literatures on SR of butanols. Bimbela et al. [69] first reported SR of saturated aqueous solution of n-butanol in the temperature range of 823–1023 K in a quartz tubular reactor using Ni/Al_2O_3 catalysts prepared by the co-precipitation method. The SR of *n*-butanol was also studied in presence of co-precipitated Ni/Al_2O_3 catalysts modified with Cu and Mg and CeO_2 and Al_2O_3 supported nickel catalysts [70,71]. The addition of Cu decreased the SR activity with enhanced stability of the catalyst. The encapsulated carbon decreased and filamentous carbon increased by Cu addition. SR of biomass derived butanol mixture (butanol:acetone:ethanol = 6:3:1 mass ratio) was reported over ZnO, TiO_2, and CeO_2 supported cobalt catalysts [72]. The Co/ZnO catalyst was reported to be most suitable for the SR of *n*-butanol than Co/CeO_2 or Co/TiO_2.

The work was further extended to OSR of biomass derived butanol mixture over cobalt catalysts doped with noble metals like Ru, Rh, Ir, and Pd supported on ZnO and CeO_2-

ZrO_2 [73–76]. The Co–Ir/ZnO catalysts were found to be most promising catalysts. Cai et al. [73] further extended the work to OSR of bio-n-butanol mixture of the ABE fermentation process using bimetallic Co–Ir/ZnO catalysts. Auto thermal steam reforming (ATSR) of isobutanol was also investigated over α-Al_2O_3 supported 1wt.% Rh-1wt.% Ce catalyst in a staged mili second contact reactor [77].

PO of isobutanol was investigated over monolith coated with γ-Al_2O_3 and Rh as the active component. Olefins (isobutene) and paraffins (methane and propane) were identified as gaseous products. The highest observed H_2 selectivity was 62.92% (and product composition of ~30% H_2O, 6-8% olefins, and <1% paraffins) at contact time of 56 mili sec and 1.425 equivalence ratio and ignition back face temperature of 673 K [78]. Some of the representative results available in literature on SR of butanol are listed in Table 1.2.

Table 1.2: Experimental results on SR of butanol.									
Catalyst	Temp., K	WHSV, h^{-1}	Flow rate, mol/hr						
			Bu	H_2O	H_2	CO	CO_2	CH_4	Ref.
33NiAl		911.88	0.0051	0.303	0.0227	0.0025	0.0063	0	[69]
		583.10	0.0051	0.303	0.0299	0.0036	0.0079	0	
	923	387.8	0.0051	0.303	0.037	0.0034	0.0105	0	
		229.17	0.0051	0.303	0.047	0.0031	0.013	0	
		153.05	0.0051	0.303	0.057	0.0030	0.0175	0	
28NiAl	823		0.011	0.706	0.0317	0.0038	0.0082	0.00007	
	923	326	0.011	0.706	0.099	0.0046	0.0266	0	
	1023		0.011	0.706	0.105	0.011	0.0292	0.00029	

1.3   Objectives of the present work

As observed from the previous discussion, limited experimental studies are available in open literatures on SR and OSR of butanols. Comprehending the enormous potential of bio-butanols, the broad objective of the present work is SR and OSR of isobutanol for the production of SG for its applications as feedstock for chemical process industries and fuel cell for generation of electric power in an environmentally cleaner manner. The more specific objectives are shown below.

1.   A comprehensive structure-activity relationship of various inexpensive transition

metals (nickel, cobalt, and molybdenum) and role of supports (γ-Al$_2$O$_3$, SiO$_2$, and ZrO$_2$) for SR of isobutanol for production of SG.

2. A systematic investigation of effects of various process parameters on SG composition for SR of isobutanol over γ-Al$_2$O$_3$ supported nickel and cobalt catalysts of varying nickel and cobalt contents respectively.

3. Detailed experimental study on OSR of isobutanol and comparison with SR over γ-Al$_2$O$_3$ supported nickel catalysts.

4. Authentication of experimental SR and OSR data with equilibrium products composition.

5. An understanding of roles of metals and supports on nature of coke formation on spent catalysts and chemical transformation of catalysts during SR and OSR.

Chapter 2

Methodology

2.1   Chemicals

Nickel (II) nitrate hexahydrate ($Ni(NO_3)_2.6H_2O$, purity $\geq$ 97%) and isobutanol (SG, purity $\geq$ 99%) were procured from Merck India Ltd., Mumbai. Cobalt (II) nitrate hexahydrate ($Co(NO_3)_2.6H_2O$, purity $\geq$ 98%) and ammonium heptamolybdate tetrahydrate ($H_{24}Mo_7N_6O_{24}.4H_2O$) were purchased from Sigma-Aldrich. γ-Al_2O_3 pellets was procured from Alfa Aesar. SiO_2 and ZrO_2 pellets were obtained from Saint Gobain NorPro, USA. All chemicals were used without further purification.

2.2   Catalysts preparation

In the present work, catalysts were prepared by incipient wetness impregnation method (Figure 2.1). Requisite amounts of precursor was first dissolved in distilled water of volume equal to (or slight excess of) pore volume (PV) of support material. The support pellets were then immersed into precursor solution with continuous stirring for about one hour for uniform distribution of precursor over entire surface of the support. The wet materials were finally dried overnight at 353 K followed by calcination at 923 K. Calcined catalyst was reduced in-situ under pure H_2 flow of 30 ml/min at 923 K prior to the SR and OSR reaction. Catalysts obtained after calcination and reduction were referred as cal and red respectively. The catalysts were abbreviated as the xMS where x= mmol of the metal per gram of support, M = metals (Ni, Co, and Mo for nickel, cobalt, and molybdenum respectively), and S = supports (Al, Si, Zr for γ-Al_2O_3, SiO_2, ZrO_2 respectively). For example, 4.3NiAl represents γ-Al_2O_3 supported nickel catalysts with 4.3 mmol (20 wt%) of nickel loaded per gram of γ-Al_2O_3. Similarly 4.3 mmol (20 wt%) of cobalt and 4.3 mmol (29 wt%) of molybdenum were loaded per gram of γ-Al_2O_3 .
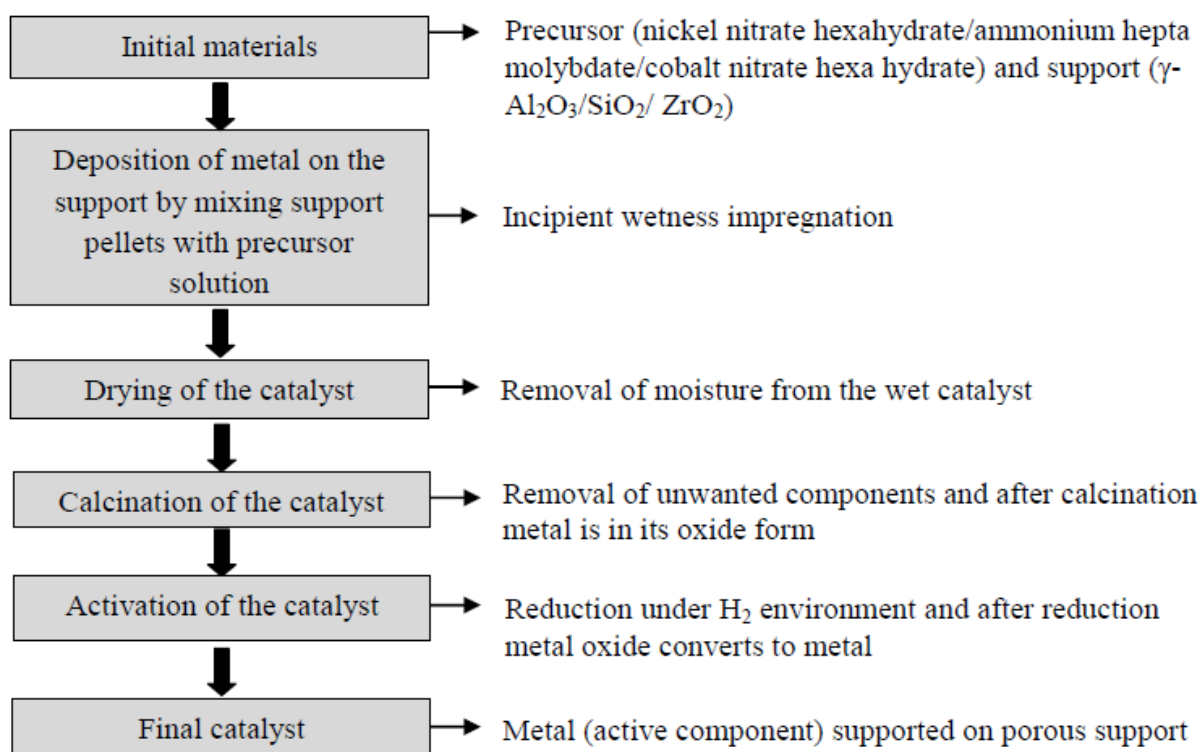
Figure 2.1: Steps involved in the preparation of supported metal catalysts by incipient wetness impregnation method.

2.3   Catalyst characterization

2.3.1   BET surface area measurement

The BET surface area (SA) and PV of the catalysts together with pure supports were obtained using Micromeritics ASAP 2020 physisorption analyzer. The samples were first degassed under vacuum (5×10^{-5} mmHg) at 523 K for 2 h to remove adsorbed moisture and other impurities present, if any. The N_2 adsorption and desorption studies were performed at 77 K in the relative pressure (P/P_0) range of 0.06 to 0.275. The SA of the catalysts was calculated using multipoint BET equation from adsorption isotherm data. The volume of liquid nitrogen adsorbed at P/P_0 = ca.1.0 was considered as PV.

2.3.2 H₂ pulse chemisorption

The H_2 pulse chemisorption studies were performed using Micromeritics AutoChem II 2920 chemisorption analyzer to determine metal dispersion (MD) and active metal surface area (SM). The calcined catalysts were first reduced at 923 K using 10 vol% H_2-Ar gas mixture (20 ml/min) for 3 h. Sample tube was then purged with pure argon at a flow rate of 20 ml/min for one hour while cooling it to 323 K to remove traces of hydrogen present, if any. Chemisorption studies were then carried out at 323 K by periodical injection of measured volume of H_2 pulses until three successive peaks were identical. The amounts of chemisorbed H_2 (moles per gram of sample) was calculated considering surface stoichiometry as $H_2/M=0.5$ where M= Ni, Co, and Mo [79,80].

2.3.3 Powder X-Ray diffraction

Powder XRD patterns of calcined, reduced, and spent catalysts were obtained in the 2θ range of $10\text{-}100^o$ in a Phillips X-pert diffractometer using CuKα radiation ($\lambda =1.541$Å, 30KV) with a scanning speed of 0.09°/s. The metal crystallite sizes were calculated for different planes by Scherrer's equation using full width half maximum (FWHM) of the XRD peaks. The average crystallite sizes of all planes were reported in the present work.

2.3.4 Temperature programmed reduction

The TPR studies of the calcined catalysts were performed in a Micromeritics AutoChem II 2920 chemisorption analyzer to identify various reducible species present. The sample was first degassed under flow of argon (20 ml/min) at 473 K for one h and then cooled down to 323 K. The 10 vol% H_2–Ar gas mixture with a flow rate of 10 ml/min was introduced and sample temperature was steadily increased from 323 K to 1173 K with a ramp rate of 5 K/min. The hydrogen consumption was monitored using thermal conductivity detector (TCD). The temperature corresponding to maximum hydrogen consumption was considered as maximum reduction temperature (T_{max}).

2.3.5   Field emission scanning electron microscopy

FESEM images of spent catalysts were captured using Zeiss Supra 40 FESEM equipped with Energy Dispersive X-Ray detector (EDX). The elemental compositions of selected surface of spent catalysts were determined using EDX analysis

2.3.6   Fourier transform infrared spectroscopy

FTIR spectra of spent catalysts were recorded using Bruker TENSOR 37 FTIR apparatus equipped with air cooled IR source and low noise DLATGS detector. Spent catalyst was first mixed with KBr and pelletized using hydraulic press. IR spectra were acquired in transmission mode in the wave number range of 400-4000 cm^{-1} at ambient temperature with a spectral resolution of 4 cm^{-1} and 128 no of scan using KBr as background acquired separately.

2.3.7   Thermo gravimetric analysis

 All the spent catalysts were characterized by Perkin Elmer Thermo gravimetric analyzer for the quantitative measurement of the coke formed during the reaction. About 6 mg of spent catalyst was taken for the analysis and the sample was purged initially using helium gas at a flow rate of 30 ml/min. Temperature was increased from ambient temperature to 423 K and holds for 10 min to remove the moisture absorbed. And then sample was heated up to 1073 K and hold for 10 minutes. Immediately the carrier gas was switched to air at a flow rate of 30 ml/min. The analysis was carried out for 30 minutes and thermogram was recorded according to the weight loss due to oxidation of the carbon. Amount of coke formed was calculated by the difference in wt% of the sample after the analysis.

2.4   Experimental set up and procedure

The SR of isobutanol was carried out in a down-flow stainless steel fixed-bed reactor (FBR) under atmospheric pressure using nitrogen as the carrier gas. The photograph and schematic of the experimental set up is shown in Figure 2.2. A measured amount (3 gm) of the catalyst in the form of cylindrical pellets (1/8″) diluted with a suitable amount (15 gm) of quartz

beads was first loaded into the stainless steel reactor (L= 40 cm, OD= ½") supported by two layers of quartz wool on either side of the catalyst bed. The reactor was kept inside a tubular furnace and a K-type thermocouple was placed just above the catalyst bed. The temperature of the catalyst bed was controlled within ±1K by a PID temperature controller. The catalysts were first reduced at 923 K by flowing pure hydrogen through a mass flow controller with a flow rate of 30 ml min^{-1} for about 3 h to ensure complete reduction of the metal oxide. The reactor was then cooled down to the steady state desired reaction temperature under a flow of nitrogen gas. Isobutanol and water were then pumped at the desired flow rate using two different metering pumps and vaporized in a pre-mixer maintained at a temperature of 473 K prior to entering the reactor. The nitrogen, introduced at a specified flow rate using another mass flow controller, served as the carrier gas and internal standard for the reaction. The produced gas stream was passed through a condenser maintained at 265–273 K to condense the condensable products present in the gas mixture. Vapor pressure of pure isobutanol calculated using Aspen Plus at different temperature is shown in the Table 2.1. The cumulative flow rates of the non-condensable gases were recorded with time-on-stream (TOS) using a wet gas meter. The total material balance was checked for all the experimental runs and errors were obtained within ±5%.

Table 2.1: Vapour pressure of isobutanol at different temperature

Temperature, K	Vapour pressure of pure isobutanol, bar
268	0.0012
273	0.0019
278	0.0029

(a)

(15)

1. Feed pumps
2. Gas cylinders
3. Mass flow controllers
4. Premixer
5. Pressure gauge
6. Preheater zone
7. Reaction zone
8. Condensor
9. Gas liquid separator
10. Thermo couples
11. Wet gas meter
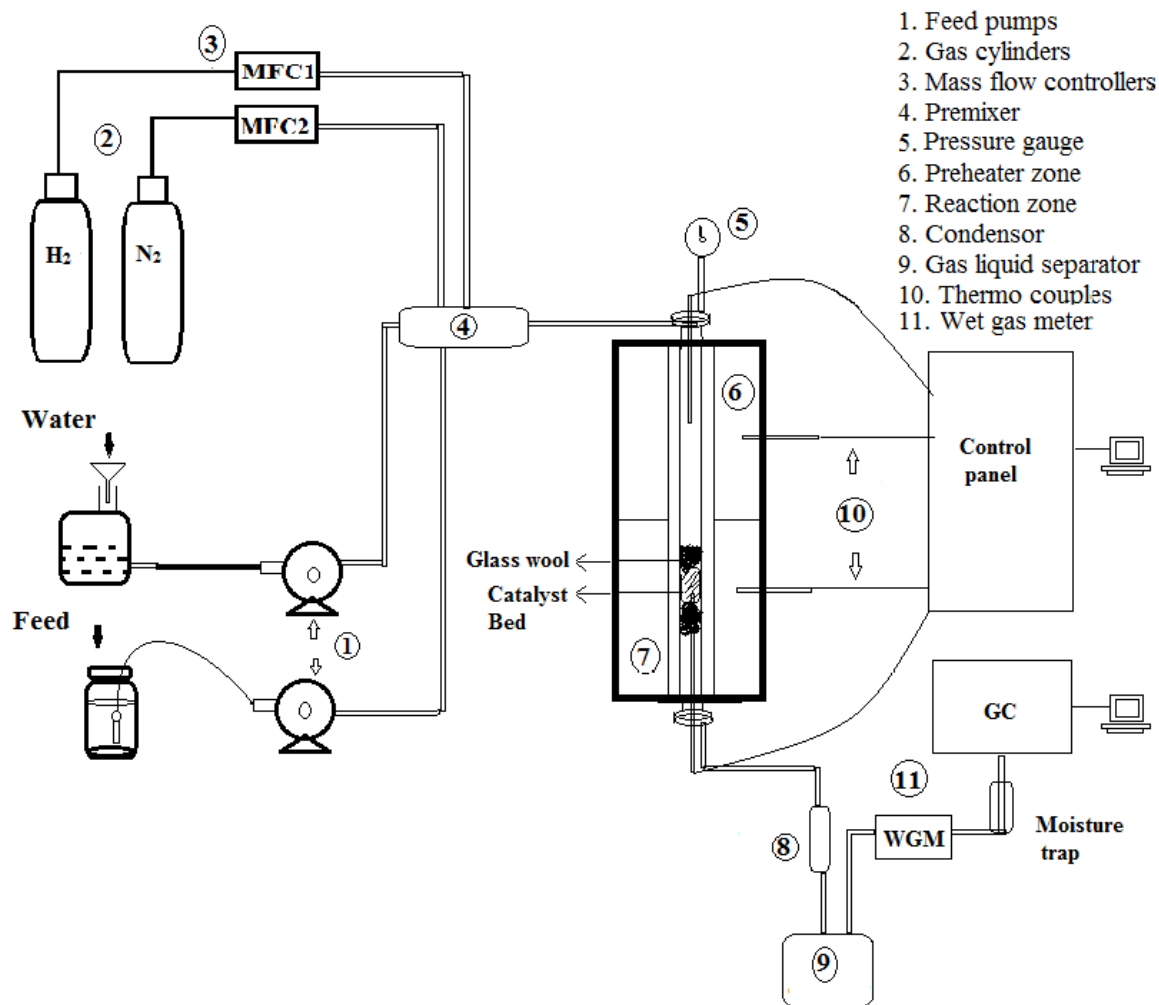
(b)

Figure 2.2: (a) Photograph and (b) schematic of fixed-bed reactor system.

The gas samples were analyzed by online gas chromatography (GC) (Shimadzu GC 2014) equipped with a TCD using a Carbosieve-S-II packed column (Chromatopak, 3m × 1/8") and argon as the carrier gas. Injector and detector temperature was maintained at 373K and 523K respectively. Initially column was maintained at 373 for 15 min and then the temperature was raised to 473K with a ramp rate of 30 K/min and maintained there for 5 min. The gas composition was calibrated with respect to nitrogen as the internal standard. The products of the liquid samples were identified with a GC equipped with a mass spectrometer (MS) detector and quantified by GC equipped with a flame ionization detector (FID) using a ZB wax column (30 m × 0.25 mm × 0.25 mm) using nitrogen as the carrier gas. Injector and detector temperature was maintained at 503K and 523K respectively. Column was maintained at 343K for 5 min initially, then increased to 443K with a ramp rate of 20K/min and maintained for 5 min. Finally, temperature was increased to 473K with a ramp rate of

(16)

30K/min and kept constant for 5 min. The typical chromatograms of gas and liquid samples representing peaks of unreacted reactant and products are shown in Figure 2.3.
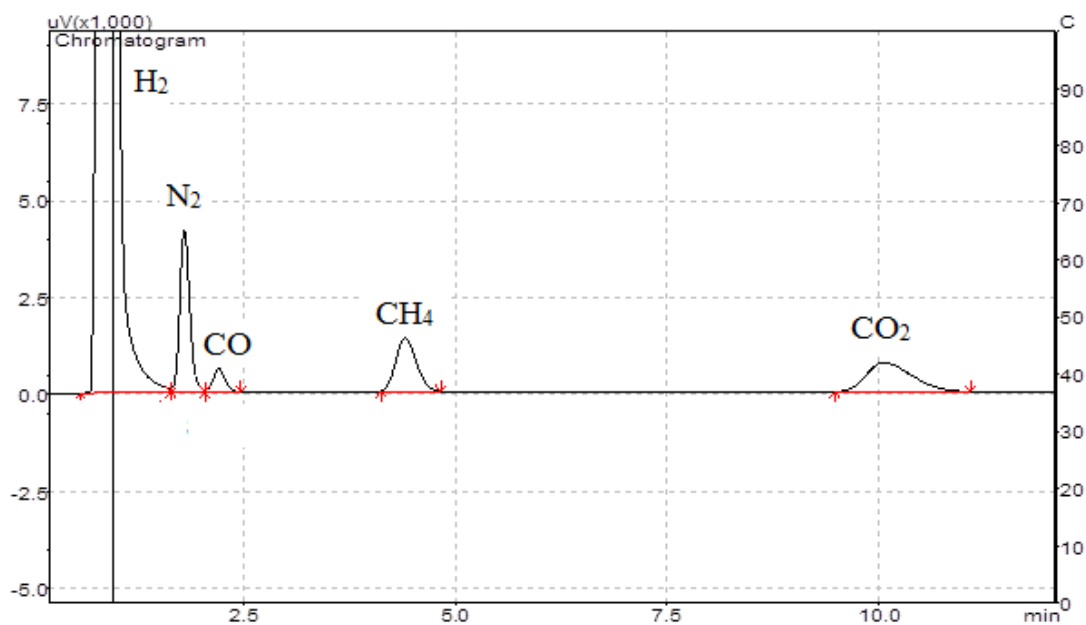
(a)
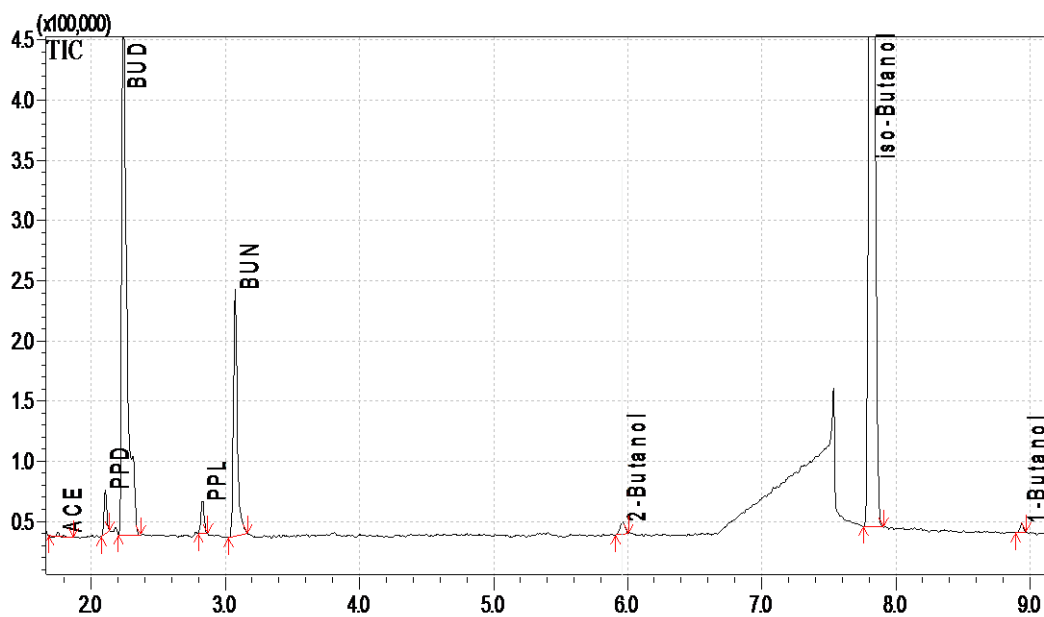
(b)

Figure 2.3: Chromatograms of (a) gas sample and (b) liquid sample. ACE = acetaldehyde, PPD = propionaldehyde, BUD = (*n*- and iso-) butyraldehyde, PPL= 2-propenal, BUN = 2-butanone.

2.5   Reactions involved in SR and OSR of isobutanol

The SR of isobutanol is quite complicated in nature involving enormous number of conceivable chemical reactions. Some of the important chemical reactions involved in SR of isobutanol are presented in **Error! Reference source not found.**. The heat of reactions of Eq.(ii) and Eqs.(iv-x) of Scheme 2.1 were obtained from the literatures [65,81]. The heat of reaction of Eq.(i) and Eq.(iii) were calculated using ASPEN plus.

Steam reforming reaction

$$i-C_4H_{10}O+3H_2O \leftrightarrow 4CO+8H_2 \qquad \Delta H^0_{298K}=558.32 \text{ kJ/mol} \qquad \text{(i)}$$

Water-gas shift reaction

$$CO+H_2O \leftrightarrow CO_2+H_2 \qquad \Delta H^0_{298K}=-41.1 \text{ kJ/mol} \qquad \text{(ii)}$$

Overall reaction

$$i-C_4H_{10}O+7H_2O \leftrightarrow 4CO_2+12H_2 \qquad \Delta H^0_{298K}=394 \text{ kJ/mol} \qquad \text{(iii)}$$

Methanation reactions

$$CO+3H_2 \leftrightarrow CH_4+H_2O \qquad \Delta H^0_{298K}=\text{-205.2 kJ/mol} \qquad \text{(iv)}$$

$$CO_2+4H_2 \leftrightarrow CH_4+2H_2O \qquad \Delta H^0_{298K}=-165 \text{ kJ/mol} \qquad \text{(v)}$$

Partial oxidation reaction

$$i-C_4H_{10}O+\frac{3}{2}O_2 \leftrightarrow 4CO+5H_2 \qquad \Delta H^0_{298K}=-160 \text{ kJ/mol} \qquad \text{(vi)}$$

Coke forming reactions

Methane decomposition reaction

$$CH_4 \leftrightarrow C+2H_2 \qquad \Delta H^0_{298K}=74.9 \text{ kJ/mol} \qquad \text{(vii)}$$

CO reduction reaction

$$CO+H_2 \leftrightarrow C+H_2O \qquad \Delta H^0_{298K}=-131.3 \text{ kJ/mol} \qquad \text{(viii)}$$

Boudouard reaction

$$2CO \leftrightarrow C+CO_2 \qquad \Delta H^0_{298K}=172.4 \text{ kJ/mol} \qquad \text{(ix)}$$

Hydrocarbon dissociation reaction

$$C_nH_{2n+2} \rightarrow nC+(n+1)H_2 \qquad \Delta H^0_{298K}=-131.29 \text{ kJ/mol} \qquad \text{(x)}$$
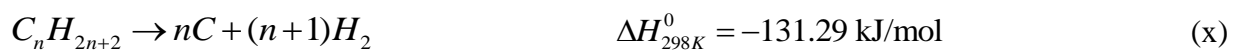
Scheme 2.1: Chemical reactions involved in SR of isobutanol.

The isobutanol reacts with water forming a mixture of hydrogen and carbon monoxide (Eq.(i) of Scheme 2.1). The SR reaction is endothermic in nature absorbing 558.32 kJ/mol of heat. The carbon monoxide then undergoes equilibrium limited water gas shift reaction (WGSR) with water forming carbon dioxide and hydrogen (Eq.(ii) of Scheme 2.1**Error! Reference source not found.**). The WGSR is slightly exothermic (ΔH^o_{298K}= -41.1 kJ/mol).

The overall SR reaction of isobutanol is endothermic (ΔH^o_{298K} = 394 kJ/mol) (Eq.(iii) of Scheme 2.1). The carbon monoxide and carbon dioxide formed in SR of isobutanol undergo exothermic reaction with hydrogen forming methane and water (Eqs.(iv-v) of Scheme 2.1). These reactions are responsible for reduction of hydrogen yield and hence undesirable for SR. The catalyst deactivation due to coke formation is one of the major challenges especially for SR of high molecular weight oxygenated compounds (Eq.(x) of Scheme 2.1). The formation carbon occurs by cracking of the C-C bonds of hydrocarbons. Some of the other probable reactions responsible for coke formation are shown by Eqs.(vii-ix) of Scheme 2.1. During OSR, isobutanol undergoes exothermic PO reaction in presence of oxygen forming CO and water. The exothermic PO reaction supplements heat required for endothermic SR reaction.

2.6   Process variables

The products composition in SR and OSR can be tuned by appropriate selection of process variables, steam-to-carbon mole ratio (SCMR), weight hourly space velocity (WHSV), and OCMR. The generalized definitions of these process variables used throughout the thesis are described below. One can observe from Eq.(iii) of Scheme 2.1**Error! Reference source not found.** that 7 moles of water is required for complete conversion of one mole of isobutanol to CO_2 and H_2. Therefore, stoichiometric SCMR of 7 was used in Eq.(2.1) This definition of SCMR signifies extents of excess water supplied compared to theoretical requirements of 1. In general, excess amounts of water are supplied to overcome thermodynamic limitations of WGSR and reduce coke formation on the catalysts. As observed from Eq.(vi) of Scheme 2.1, 1.5 moles of oxygen is required for complete conversion of one mole of isobutanol to CO and H_2. Therefore, 1.5 was considered as stoichiometric OCMR for Eq.(2.3) This definition of OCMR represents extents surplus or deficient oxygen supplied compared to theoretical maximum requirements of 1.

Steam-to-carbon mole ratio

$$= \frac{\left(\dfrac{\text{rate of moles of water fed}}{\text{rate of moles of isobutanol fed}}\right)}{\left(\dfrac{\text{moles of water}}{\text{moles of isobutanol}}\right)_{stoichiometric}} \qquad (2.1)$$

$$= \left(\frac{\text{rate of moles of water fed}}{7\times\text{rate of moles of isobutanol fed}}\right)$$

Weight hourly space velocity, h^{-1}

$$= \left(\frac{\begin{array}{c}\text{total mass flow rate of}\\ \text{isobutanol, water, nitrogen, and oxygen}\end{array}}{\text{weight of catalyst}}\right) \qquad (2.2)$$

Oxygen-to-carbon mole ratio (OCMR)

$$= \left(\frac{\text{rate of moles of oxygen}}{\text{rate of moles of isobutanol}}\right) \Bigg/ \left(\frac{\text{rate of moles of oxygen}}{\text{rate of moles of isobutanol}}\right)_{stoichiometric} \qquad (2.3)$$

$$= \frac{(\text{rate of moles of oxygen})}{1.5\times(\text{rate of moles of isobutanol})}$$

The progress of SR and OSR is generally expressed in terms of carbon conversion to gaseous products (CCGP), hydrogen yield, and selectivity to CO, CO_2, and methane. The generalized expressions of these progressed variables used throughout the thesis are represented by following equations [82,83]. As observed from Eq.(iii) of Scheme 2.1, maximum of 12 moles of hydrogen can be produced from one mole of isobutanol. However, number of moles of hydrogen produced per mole of isobutanol is practically far less due to thermodynamic limitation of WGSR and incomplete reforming of methane. Therefore, stoichiometric hydrogen yield of 12 was used in Eq.(2.6). The present definition of hydrogen yield therefore represents how far-off actual hydrogen yield from theoretical maximum of 100%.

Carbon conversion to gaseous products,%

$$=100\times\frac{\left(\begin{array}{c}\text{rate of moles of carbon}\\ \text{leaving as gaseous products}\end{array}\right)}{\text{rate of moles of carbon fed}} \qquad (2.4)$$

$$=100\times\frac{\left(\begin{array}{c}\text{rate of moles of CO, CO}_2\text{,}\\ \text{and CH}_4\text{ formed}\end{array}\right)}{4\times\text{rate of moles of isobutanol fed}}$$

Conversion of isobutanol,%

$$=100\times\frac{\left(\text{rate of moles of isobutanol fed-rate of moles of isobutanol unreacted}\right)}{\text{rate of moles of isobutanol fed}} \qquad (2.5)$$

Hydrogen yield, %

$$=100\times\frac{\left(\dfrac{\text{rate of moles of hydrogen formed}}{(\text{rate of moles of isobutanol fed})\times(\text{fractional CCGP})}\right)}{\left(\dfrac{\text{rate of moles of hydrogen formed}}{\text{rate of moles of isobutanol reacted}}\right)_{\text{stoichiometric}}} \qquad (2.6)$$

$$=100\times\frac{\text{rate of moles of hydrogen formed}}{12\times(\text{rate of moles of isobutanol fed})\times(\text{fractional CCGP})}$$

Selectivity to CO, CO$_2$, or CH$_4$, %

$$=100\times\frac{\text{rate of moles of CO, CO}_2\text{, or CH}_4\text{ formed}}{\text{rate of moles of CO+CO}_2\text{+CH}_4\text{ formed}} \qquad (2.7)$$

2.7   Thermodynamic analysis

Thermodynamic equilibrium analysis of SR and OSR of isobutanol was carried out using equilibrium reactor model, R-Gibbs, available in Aspen Plus®, Aspen Tech™ software [82,83]. The R-Gibbs reactor model calculates equilibrium products composition based on the principle of minimization of Gibbs free energy of the whole system considering all components as product. The thermodynamic equilibrium analysis was performed considering feed consisting of isobutanol, water, and oxygen entered into R-Gibbs reactor at the temperature of reactor. In the present study, hydrogen, carbon monoxide, carbon dioxide, methane, and oxygen (in case of OSR) together with carbon (graphite) and various hydrocarbons and oxygenated hydrocarbons with four or less carbon atoms were considered as probable products in both SR and OSR. The equilibrium mole fraction of carbon

(21)

(graphite), compounds containing two or more carbon atoms, and oxygen (in case of OSR) was however negligibly small for the whole range of process conditions examined. Hence these products were not considered for subsequent studies. Complete conversion of isobutanol was observed over entire range of temperature studied (773-923 K) during the thermodynamic equilibrium analysis. A brief description of algorithm of R-Gibbs reactor model for calculation of equilibrium products composition is outlined below. Total Gibbs free energy of the system containing N number of chemical compounds can be expressed by following equation.

$$G^t = \sum_{i=1}^{i=N} n_i \mu_i = \sum_{i=1}^{i=N} n_i G_i^0 + RT \sum_{i=1}^{i=N} n_i \ln \frac{f_i}{f_0} \tag{2.8}$$

Assuming ideal behaviour of gas phase, fugacity of compound i (f_i) and standard state fugacity of compound i (f_i^0) can be expressed as $f_i = \varphi_i y_i P$ and $f_i^0 = P^0$ respectively. Since G_i^0 is equal to zero for each chemical element in its standard state, $\Delta G^0 = \Delta G_{fi}^0$ for each component is assumed. The minimum Gibbs free energy of the whole system containing N number of gaseous species can now be represented by following equation based on Lagrange's undetermined multiplier method.

$$\sum_{i=1}^{N} \left(\Delta G_{f_i}^0 + RT \ln \frac{\varphi_i y_i P}{P^0} + \sum_k \lambda_k a_{ik} \right) = 0 \tag{2.9}$$

with following constraints of elemental balances.

$$\sum_{i=1}^{N} n_i a_{ik} = A_k \tag{2.10}$$

The Gibbs free energy of solid carbon can be expressed considering vapour-solid phase equilibrium as represented by following equation.

$$\overline{G}_{c(g)} = \overline{G}_{c(s)} = G_{c(s)} = \Delta G_{fc(s)}^0 = 0 \tag{2.8}$$

The Gibbs free energy minimization function was obtained by substituting Eq.(2.) and Eq.(2.8) in Eq. (2.8)

$$\sum_{i=1}^{N-1} n_i \left(\Delta G_{f_i}^0 + RT \ln \frac{\varphi_i y_i P}{P^0} + \sum_k \lambda_k a_{ik} \right) + \left(n_c \Delta G_{fc(s)}^0 \right) = 0 \tag{2.9}$$

Chapter 3

Performance of Metals (Ni, Co, Mo) and Roles of Supports (γ-Al$_2$O$_3$, SiO$_2$, ZrO$_2$) for Steam Reforming of Isobutanol

The performance of supported metals catalysts depends strongly on the type of metals and supports and extent of metal-support interactions. However, there is no systematic study in the open literature on role of metals and supports for SR of isobutanol. A systematic investigation was therefore undertaken in the present work to provide a comprehensive structure-activity relationship of various inexpensive transition metals (nickel, cobalt, and molybdenum) and role of supports (γ-Al$_2$O$_3$, SiO$_2$, and ZrO$_2$) for SR of isobutanol. Understanding roles of metals and supports on nature of coke formation on spent catalysts and chemical transformation of catalysts during SR were additional objectives of the present work.

3.1   Characterization of the catalysts

3.1.1   Surface area and pore volume

The SA and PV of calcined and reduced catalysts and pure supports are shown in Table 3.1. The SAs of γ-Al$_2$O$_3$, SiO$_2$, and ZrO$_2$ were 240, 233, and 38 m^2/g respectively. The SAs of both calcined and reduced catalysts were somewhat lesser than corresponding pure supports. The decrease of SA with impregnation of metals on the supports might be due to coverage of surfaces and blockage of pores of supports by metal or metal oxide. For γ-Al$_2$O$_3$ supported nickel, cobalt, and molybdenum catalysts with identical moles of metal loading; trends of SAs were in the order of 4.3MoAl (29 wt%)<4.3NiAl (20 wt%)~4.3CoAl (20 wt%) for both calcined and reduced catalysts. The lowest SA observed for 4.3MoAl might be due to large atomic mass of molybdenum and pore-blockage phenomenon quite often observed in

incipient wetness impregnation method. The PVs of SiO_2, γ-Al_2O_3, and ZrO_2 were 0.98, 0.84, and 0.2 cm^3/g respectively. Similar to SA, PV also decreased slightly with impregnation of metals/metal oxides on the supports. For γ-Al_2O_3 supported nickel, cobalt, and molybdenum catalysts, highest PV was observed for 4.3NiAl with 4.3MoAl being least for both calcined and reduced catalysts. The trends of SA and PV results were analogous and hence statements used to explain trends of SA are applicable for PV as well.

3.1.2 Metal dispersion and metallic surface area

The MD and metallic surface area (SM) of supported metal catalysts are shown in Table 3.1. For γ-Al_2O_3 supported metal catalysts with equal moles of metal loading, 4.3NiAl displayed highest MD and SM followed by 4.3CoAl and 4.3MoAl. This result clearly demonstrates that nickel has strongest interaction with γ-Al_2O_3 followed by cobalt and molybdenum. For γ-Al_2O_3 and SiO_2 supported nickel catalysts, higher MD and SM were observed for 4.3NiAl compared to 4.3NiSi.

Table 3.1: Physicochemical properties of the catalysts.

catalysts	BET				SD	chemisorption		XRD	TPR	H$_2$ Consumed (μmol/g)
	Cal		Red							
	SA	PV	SA	PV		MD	SM	d_c	T_{max}	
γ-Al_2O_3	228	0.84	-	-	-	-	-	-	-	
SiO_2	233	0.98	-	-	-	-	-	-	-	
ZrO_2	38	0.2	-	-	-	-	-	-	-	
4.3NiAl	178	0.6	166	0.6	19.5	1.86	12.4	13.6	790, 995	3167.4
4.3NiSi	185	0.73	143	0.7	22.6	0.29	1.90	30.9	661, 767	2875.7
4.3NiZr	27	0.18	33	0.16	98.1	0.07	0.47	26.7	661, 681	1980.7
4.3MoAl	119	0.49	142	0.52	-	0.02	0.14	129.4, 34.9[a]	720, 833	2461.1
4.3CoAl	166	0.58	163	0.59	-	0.29	2.01	19.2	752, 877, 942	2437.7

cal =calcined; red = reduced, SA = BET surface area, m^2/g; PV =pore volume, cm^3/g; SD =surface density, nickel atom/nm^2; MD= metal dispersion, %; SM= metallic surface area, m^2/g metal; d_c=metal crystallite size, nm. [a] unreduced forms or oxide forms (MoO_3), T_{max}=maximum reduction temperature, K.

The possible effects of SA on MD and SM can however be safely nullified in this case as SA of γ-Al$_2$O$_3$ and SiO$_2$ were very close. Therefore, it can be undoubtedly concluded that nickel-γ-Al$_2$O$_3$ interaction is much stronger compared to nickel-SiO$_2$ that leads to higher MD and SM for 4.3NiAl than 4.3NiSi. The 4.3NiZr was however excluded from the comparison of metal-support interactions due to very low SA of ZrO$_2$ as compared to γ-Al$_2$O$_3$ and SiO$_2$. Moreover, surface density of nickel in 4.3NiZr was much higher compared to 4.3NiAl and 4.3NiSi as shown in Table 3.1.

3.1.3 Powder XRD

Powder XRD patterns of calcined catalysts together with pure supports are shown in Figure 3.1). Powder XRD patterns of bulk metals oxide are also shown in same figure as quick references. Powder XRD patterns of calcined γ-Al$_2$O$_3$, SiO$_2$, and ZrO$_2$ supported nickel catalysts revealed characteristic peaks of bulk nickel oxide at 2θ of 37.26° (1 1 1), 43.46° (2 0 0), 62.88° (2 2 0), 75.42° (3 1 1), and 79.5° (2 2 2) (PDF#750197). The bulk nickel oxide peaks at 2θ of 75.42° and 79.5° were however not observed in calcined 4.3NiAl. Powder XRD patterns of calcined γ-Al$_2$O$_3$ supported cobalt and molybdena catalysts exhibited representative peaks of bulk cobalt oxide (Co$_3$O$_4$) at 2θ of 31.37° (2 2 0), 36.99° (3 1 1), 44.99° (4 0 0), 59.32° (5 1 1), and 65.38° (4 4 0) (PDF#781970) and molybdenum trioxide (MoO$_3$) at 2θ of 20.91° (1 1 1), 23.1° (0 0 2), 23.3° (0 2 0), 23.49° (2 0 0), and 26.3° (2 1 0) (PDF#800347) respectively. From above observations, it may therefore be concluded that calcined catalysts were associated with corresponding bulk metal oxides in their structure.

Powder XRD patterns of the reduced catalysts are shown in Figure 3.2. Powder XRD patterns of pure supports (calcined at 923 K) were also compared with that of reduced catalysts to avoid difficulty in identification of metals/metals oxide peaks. Three characteristic nickel crystallite peaks were identified at 2θ of 44.52° (1 1 1), 51.89° (2 0 0), and 76.44° (2 2 0) for 4.3NiAl, 4.3NiSi, and 4.3NiZr (PDF# 701849) [84,85]. For reduced γ-Al$_2$O$_3$ supported cobalt catalysts, two distinct cobalt crystallite peaks were observed at 2θ of 44.29° (1 1 1) and 75.95° (2 2 0) (PDF#894307). 4.3MoAl showed peaks corresponding to both molybdenum at 2θ of 40.598° (1 1 0) and 73.74° (2 1 1) (PDF#895156) and molybdenum dioxide (MoO$_2$) at 2θ of 26.19° (1 1 1), 36.89° (2 0 0), and 53.85° (2 2 2) (PDF#761807). The MoO$_2$ peaks observed in powder XRD of 4.3MoAl were due to its incomplete reduction at 923 K. The metals oxide peaks were however not detected in powder

XRD patterns of reduced γ-Al₂O₃, SiO₂, and ZrO₂ supported nickel and γ-Al₂O₃ supported cobalt catalysts. This result indicates that nickel and cobalt oxides are completely reducible at reduction temperature of 923 K.
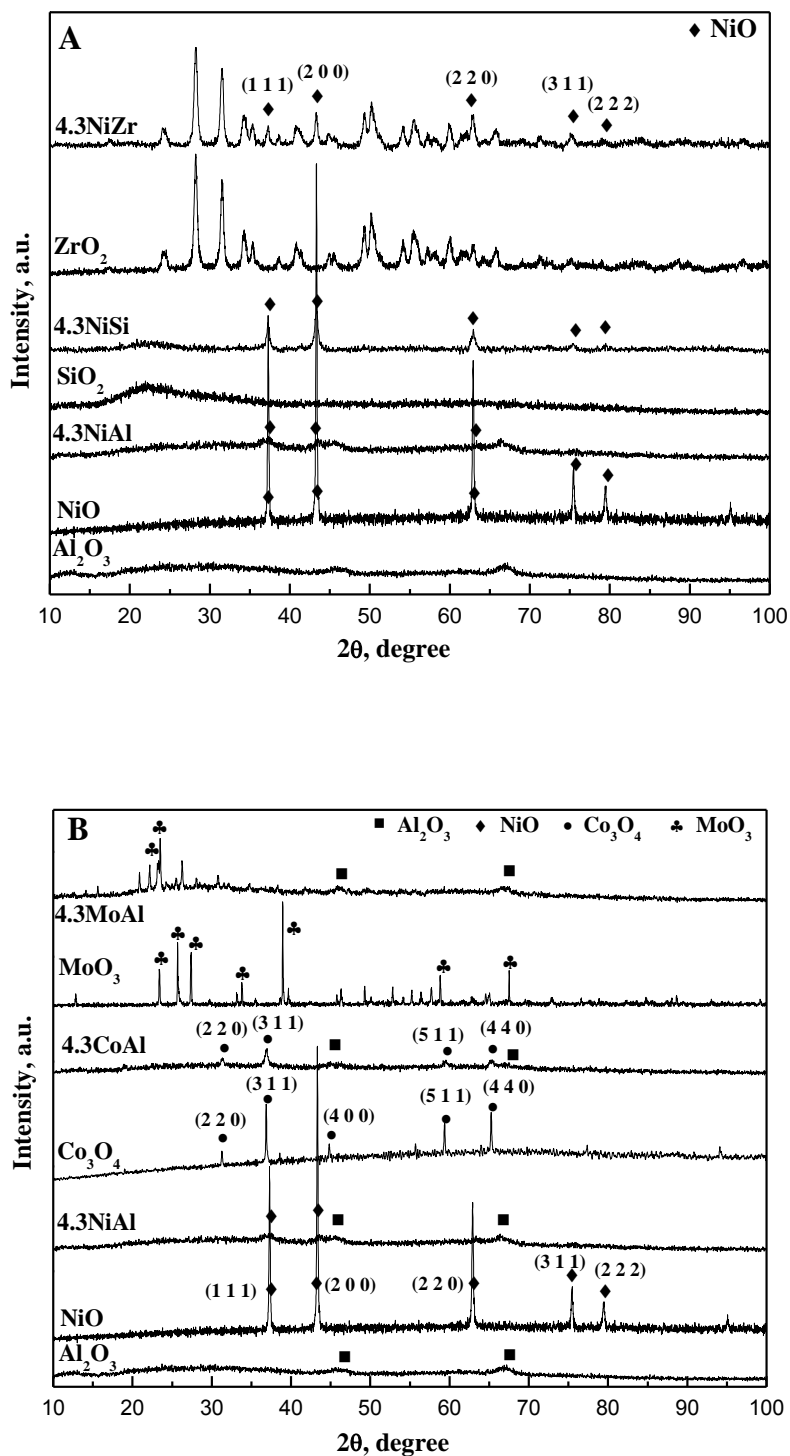
Figure 3.1: Powder XRD patterns of calcined catalysts. A. NiO, γ-Al₂O₃, 4.3NiAl, SiO₂, 4.3NiSi, ZrO₂, and 4.3NiZr. B. γ-Al₂O₃, NiO, 4.3NiAl, Co₃O₄, 4.3CoAl, MoO₃, 4.3MoAl.
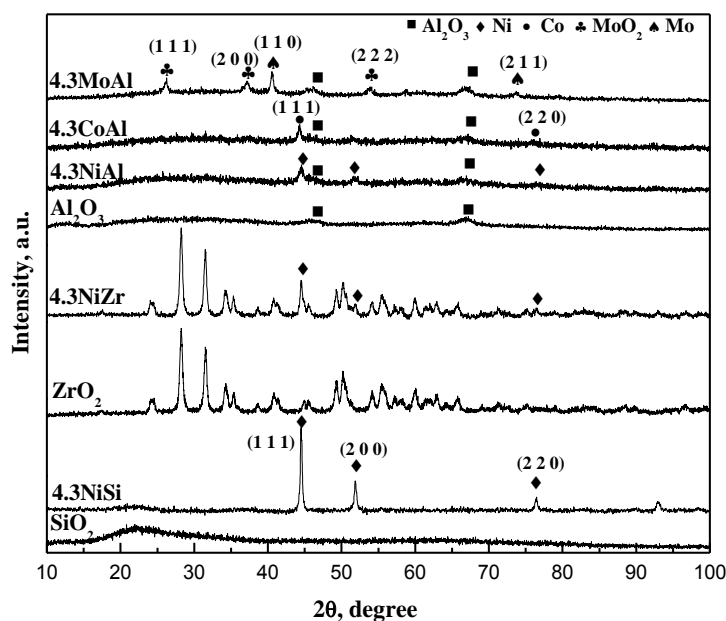
Figure 3.2: Powder XRD patterns of reduced catalysts: SiO_2, 20NiSi, ZrO_2, 4.3NiZr, γ-Al_2O_3, 4.3NiAl, 4.3CoAl, 4.3MoAl.

The average nickel crystallite sizes were 13.6, 30.9, and 26.7 nm for 4.3NiAl, 4.3NiSi, and 4.3NiZr respectively (Table 3.1). Lower nickel crystallite size for 4.3NiAl compared to 4.3NiSi and 4.3NiZr may be attributed to high SA of γ-Al_2O_3 and stronger metal-support interaction leading to high MD (Table 3.1). For reduced γ-Al_2O_3 supported nickel, cobalt, and molybdenum catalysts, average metals crystallite size were increasing in the order of Ni<Co<Mo (Table 3.1). The trends metals crystallite size obtained from powder XRD were fully concurring with MD obtained from H_2 pulse chemisorption.

3.1.4 Temperature programmed reduction

TPR profiles of pure supports and calcined catalysts are shown in Figure 3.3. TPR profiles of bulk metals oxides are also shown in the same figure as references. γ-Al_2O_3, SiO_2, and ZrO_2 showed no reduction peaks thereby confirming that pure supports are not reducible under the ranges of temperature [15]. The calcined 4.3NiAl exhibited two reduction peaks at 790 and 995 K. The lower temperature broad peak represents reduction of bulk nickel oxide; whereas higher temperature peak corresponds to reduction of dispersed nickel oxide having stronger

interaction with γ-Al_2O_3 than bulk nickel oxide. The relative peaks area and intensity further suggests that majority of nickel oxide was present in dispersed form in 4.3NiAl.

On the contrary, calcined γ-Al_2O_3 supported cobalt and molybdenum catalysts are known to reduce in two separate stages. Three distinct reduction peaks were observed for calcined γ-Al_2O_3 supported cobalt catalysts at 745-775, 874-885, and 942 K. The first two peaks were associated with reduction of various surface cobalt species; whereas peak at 942 K was due to reduction of $CoAlO_4$ spinel [86]. TPR profile of bulk cobalt oxide also showed three different reduction peaks at 642, 679 and 702 K [87]. The peak at 679 K was due to reduction of CoO to metallic cobalt; while peaks at 642 and 702 K were due to reduction of Co_3O_4 to metallic cobalt [86]. The shifting of reduction peaks relative to bulk cobalt oxides peaks may be due to weak interaction of cobalt oxides with γ-Al_2O_3 and extents of different bulk cobalt oxides species on γ-Al_2O_3. Two distinct reduction peaks were observed for calcined 4.3MoAl at 720 and 833 K corresponding to reduction of molybdenum trioxides (MoO_3) to MoO_2 and MoO_2 to molybdenum respectively.
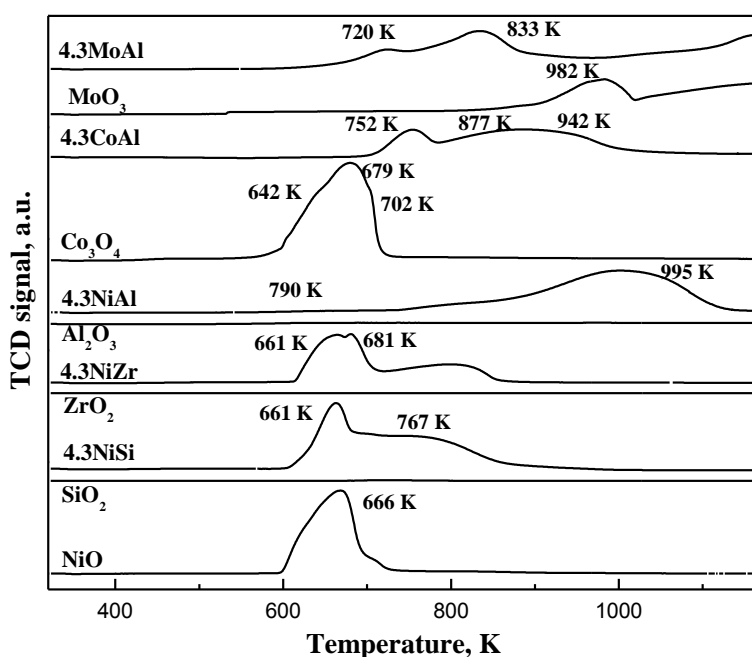
Figure 3.3: TPR profiles of NiO, SiO_2, 4.3NiSi, ZrO_2, 4.3NiZr, γ-Al_2O_3, 4.3NiAl, Co_3O_4, 4.3CoAl, MoO_3, and 4.3MoAl.

(28)

Contrary to calcined 4.3NiAl (790 and 995 K), bulk and dispersed nickel oxide reduction peaks were observed at lower temperature for calcined 4.3NiSi (661 and 767 K) and 4.3NiZr (661 K and 681 K) (Figure 3.3). The relative peaks intensity and area further shows that nickel oxide exists largely in bulk form in calcined 4.3NiZr and 4.3NiSi [88]. These results clearly demonstrate that reducibility of supported nickel catalysts depends strongly on nature of supports which in turn affects metal-support interactions. From the trends of T_{max} (Table 3.1), it may be further concluded that nickel has strong interaction with γ-Al_2O_3 followed by SiO_2 and ZrO_2.

3.2   Possible SR reactions

The SR of isobutanol involves cleavage of carbon-carbon, carbon-oxygen, and carbon-hydrogen bonds leading to a large number of plausible chemical reactions. However, basic chemical reactions of SR of isobutanol are shown in **Error! Reference source not found.** [10]. These reactions led to formation of H_2, CO, CO_2, and CH_4 as gaseous products as observed for SR of isobutanol. The formation of a number of intermediate chemical compounds such as acetaldehyde, propionaldehyde, 2-propenal, butyraldehydes, and 2-butanone together with unreacted (1-, 2-, and iso-) butanols were observed additionally during analysis of liquid samples for all experimental runs (**Error! Reference source not found.**). The identification and quantification of such intermediate chemical compounds are very much important to envisage probable chemical reactions occurred in SR of isobutanol as shown in Scheme 3.1.

From products distribution in liquid samples it may be concluded that isobutanol undergoes isomerization reactions during SR that led to formation of 1- and 2-butanols. The 1-, 2-, and iso-butanols further transforms to butyraldehyde, 2-butanone, and isobutyraldehyde respectively by dehydrogenation reactions. The carbon-carbon bond cleavage at various locations of butanols structure led to formation of various stable intermediate compounds including acetaldehyde, propionaldehyde, and 2-propenal as observed in the liquid samples. These intermediate compounds further undergone deep cracking and SR reaction forming H_2, CO, CO_2, and CH_4 as gaseous products.

Isomerization reactions

(i)

Dehydrogenation reactions

(ii)
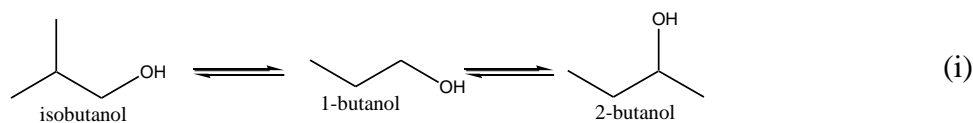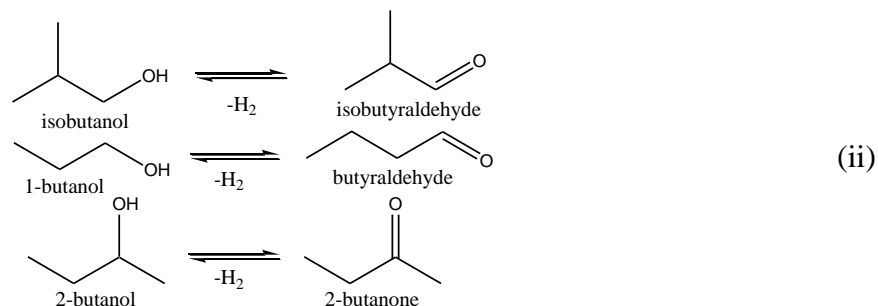
Carbon-carbon bond cleavage reactions

(iii)
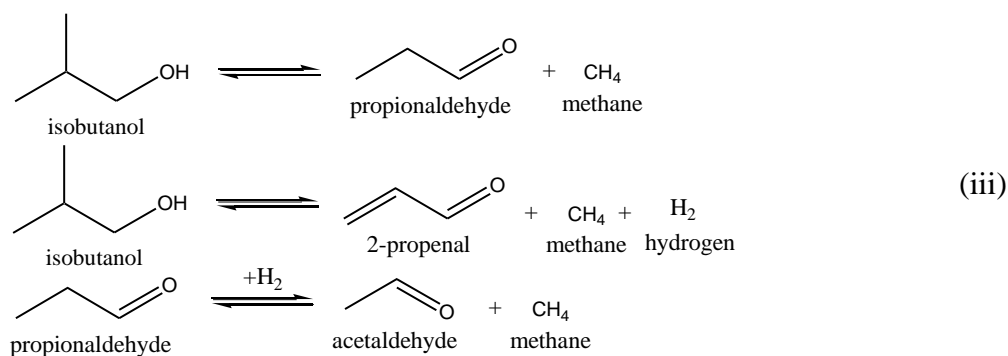
Scheme 3.1: Plausible chemical reactions involved in SR of isobutanol.

3.3   Results and discussion

The catalytic activity of supported (γ-Al_2O_3, SiO_2, and ZrO_2) metals (nickel, cobalt, and molybdenum) catalysts were evaluated for SR of isobutanol at 923 K, SCMR = 2.2, WHSV = 6.62 h^{-1}. The molar flow rates of feeds, gaseous, and liquid products together with unreacted butanols (1, 2, and iso-butanols) were calculated for all runs as presented in Table 3.2. The carbon balance errors (CBE) were also checked and errors were within ±10% for all experimental runs.

Table 3.2 : Carbon balance table for SR of isobutanol.

catalysts	gas products flow rates, mol h^{-1}				liquid products flow rates$\times 10^3$, mol h^{-1}						CBE	CIB	H$_2$/Bu
	H$_2$	CO	CH$_4$	CO$_2$	ACE	PPD	PPL	BUD	BUN	BU			
Effect of Supports [a]													
4.3NiAl	0.474	0.064	0.017	0.122	0	0.018	0.009	0.028	0.011	1.18	0.7	97.73	9.3
4.3NiSi	0.427	0.063	0.014	0.105	0	0.112	0.002	0	0.002	1.99	7.7	96.17	8.5
4.3NiZr	0.207	0.039	0.003	0.039	0	1.011	0.019	0	1.174	25.04	8.4	51.84	7.6
Effect of Metals [a]													
4.3NiAl	0.474	0.064	0.017	0.122	0	0.018	0.009	0.028	0.011	1.18	0.74	97.73	9.3
4.3CoAl	0.413	0.076	0.013	0.099	0.003	0.062	0	0	0.037	0.51	5.5	99.01	8.02
4.3MoA1	0.168	0.049	0.005	0.020	0.01	5.145	0.413	0	0.356	24.56	7.3	52.7	6.1

ACE = acetaldehyde, PPD = propionaldehyde, PPL= 2-propenal, BUD = (*n-* and iso-) butyraldehyde, BUN = 2-butanone, BU = 1-, 2-, and iso-butanol; CBE = carbon balance error, %, CIB=Conversion of isobutanol, %.

[a] isobutanol = 0.052 mol h^{-1}, H$_2$O = 0.83 mol h^{-1}, and N$_2$ = 0.14 mol h^{-1}. Conditions: 923 K, SCMR=2.2, WHSV = 6.62 h^{-1}.

3.3.1   Role of supports

For precise comparison of roles of supports (γ-Al$_2$O$_3$, SiO$_2$, and ZrO$_2$) for SR of isobutanol, three catalysts were prepared with identical moles of nickel loadings on these supports, 4.3NiAl, 4.3NiSi, and 4.3NiZr. These catalysts were then tested for SR of isobutanol under identical experimental conditions as shown in Figure 3.4. As observed from the figure, 4.3NiAl displayed highest catalytic activity among three catalysts with ~98% CCGP. The 4.3NiSi showed slightly lower catalytic activity than 4.3NiAl with CCGP of ~88%. The lower catalytic activity of 4.3NiSi compared to 4.3NiAl might be due to weak metal-support interactions as reflected by its poor MD, bigger nickel crystallite size (Table 3.1), and significant contents of bulk nickel (Figure 3.3).

Figure 3.4: Effect of supports on CCGP, hydrogen yield, and selectivity to CO, CO_2, and CH_4. Conditions: 923 K, SCMR = 2.2, WHSV= 6.62 h^{-1}, N_2 = 0.014 mol/min.

On the other hand, 4.3NiZr demonstrated least catalytic activity among the three catalysts with CCGP of only ~40%. The lowest catalytic activity of 4.3NiZr might be due to both low SA (Table 3.1) and higher extents of bulk nickel (Figure 3.3) with poor/or no metal-support interaction [20]. The low MD value of 4.3NiZr also supports above statement (Table 3.1). The 4.3NiZr however showed highest hydrogen yield of ~85%; while it was ~78% for both 4.3NiAl and 4.3NiSi. Moreover, selectivity to methane was lowermost for 4.3NiZr. The lower selectivity to methane for 4.3NiZr may be due to surface oxygen mobility characteristic of zirconia support. This is a desirable characteristic of a catalyst for SR as it increases sintering resistance and removes carbonaceous deposits from catalyst surface as CO by reacting with released oxygen [20]. The lower selectivity to methane leads to a slightly higher hydrogen yield as observed for 4.3NiZr. The trends of selectivity to CO were totally reverse of trends of CCGP as observed from the figure. This results clearly indicate that equilibrium limited WGSR (Eq.(ii) of **Error! Reference source not found.**) become significant only at high CCGP leading to lower selectivity to CO and higher selectivity to CO_2 at higher CCGP.

(32)

The unreacted butanols were dominating compounds in the liquid samples with insignificant amounts of various other intermediate compounds as observed from the Table 3.2. The molar flow rates of butanols and intermediate compounds were decreased with increasing CCGP in the order of 4.3NiZr<4.3NiSi<4.3NiAl. Since performance of γ-Al_2O_3 supported nickel catalyst was superior for SR of isobutanol among three supported nickel catalysts, subsequent studies were performed using γ-Al_2O_3 as supports.

3.3.2 Performance of nickel, cobalt and molybdenum

The catalytic performance of γ-Al_2O_3 supported nickel, cobalt, and molybdenum catalysts with identical moles of metal loading are shown in Figure 3.5. 4.3NiAl showed highest catalytic activity with 98% CCGP followed 4.3CoAl (~86% CCGP) and 4.3MoAl (~36% CCGP). The catalytic activity of transition metals for SR of isobutanol is strongly related to their interactions with support.
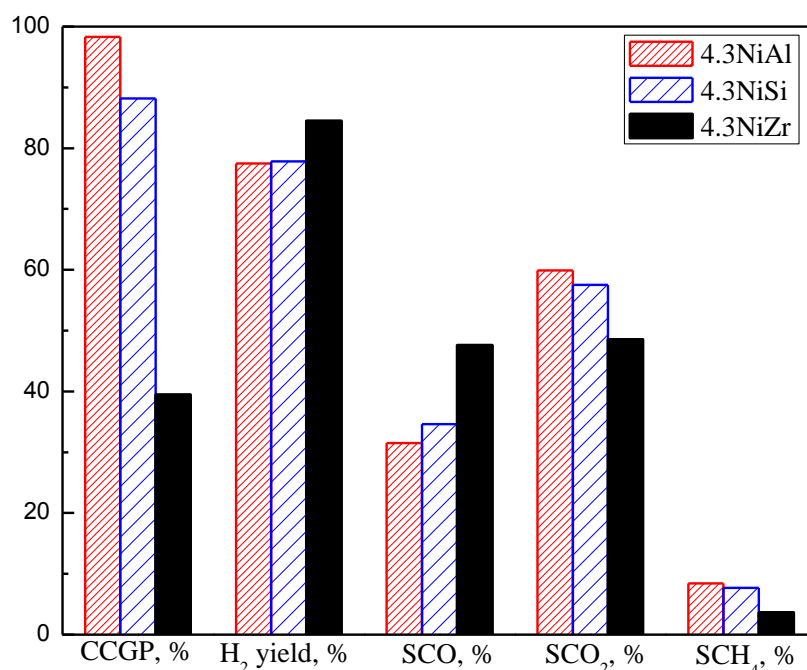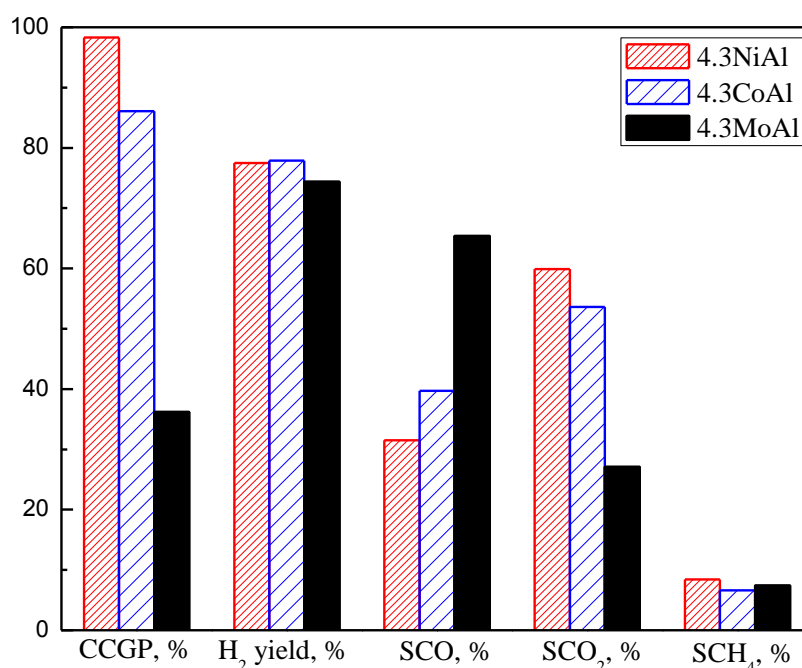

Figure 3.5: Effect of metals on CCGP, hydrogen yield, and selectivity to CO, CO_2, and CH_4. Conditions: 923 K, SCMR = 2.2, WHSV = 6.62 h^{-1}.

The catalytic activity increased with increasing metal-support interactions (4.3MoAl<4.3CoAl<4.3NiAl) as reflected by their MD and metal crystallite size. Moreover, presence of a fraction of molybdenum as MoO_2 in 4.3MoAl (as confirmed from powder XRD patterns) was also responsible for its low catalytic activity.

The hydrogen yield of ~78% was observed for both 4.3NiAl and 4.3CoAl; while it was about ~75% for 4.3MoAl. The selectivity to CO increased in the order of 4.3NiAl<4.3CoAl<4.3MoAl; while trend was reverse for selectivity to CO_2. It may be further observed that trends of selectivity to CO were completely reverse of trends of CCGP as observed previously. The similar arguments used in the previous section can also be used to explain trends of selectivity to CO and CO_2. The selectivity to methane was however found to be similar for all the catalysts. The molar flow rate of butanols and intermediate chemical compounds also decreased with increasing CCGP as shown in Table 3.2. From these results it can be concluded that γ-Al_2O_3 supported nickel and cobalt catalysts are suitable for SR of isobutanol.

3.3.3 Spent catalyst characterization

The characterization of spent catalysts for SR plays important role to understand nature of catalysts deactivation due to coke formation [89]. The possible reactions responsible for coke formation in SR are outlined in reactions of Eqs.(vii-x) of **Error! Reference source not found.**. Realizing the significance, several attempts were also made in the past to identify nature and amount of coke formed on spent catalysts for SR of various oxygenated compounds [73,75,90,91]. In the present work, spent catalysts were characterized to recognize roles of metals and supports on nature of coke formed and chemical transformation of the catalysts during SR of isobutanol.

3.3.4 SEM analysis

FESEM images of fresh catalysts and spent catalysts together with EDX analysis of selected surface are shown in Figure 3.6 and Figure 3.7 respectively. As observed from the figures, carbons nano-fibers were mainly formed on γ-Al_2O_3 supported nickel and cobalt catalysts used for SR reaction [92]. Moreover, carbon nano-fibers were grown from the tip of carbon nano-fibers containing nickel or nickel carbide particles (white spots in SEM image) [93].

(34)

The similar observations were also reported earlier for SR of ethanol [94,95]. On the other hand, combination of carbon spheres, nano-fibers, filaments, and rectangular flakes were observed in significant amounts on spent 4.3MoAl. These observations clearly demonstrated that shape and quantity of carbon formed on spent catalysts was strongly influenced by nature of metals. However, only carbon nano-fibers were observed on spent γ-Al_2O_3, SiO_2, and ZrO_2 supported nickel catalysts. The carbon formed a dense nano-fiber network on spent 4.3NiZr; whereas it was remained as dispersed nano-fibers on spent 4.3NiSi. From these results, it can be further concluded that nature of supports affects only quantity of coke on the spent catalyst without affecting shape of the carbon much.
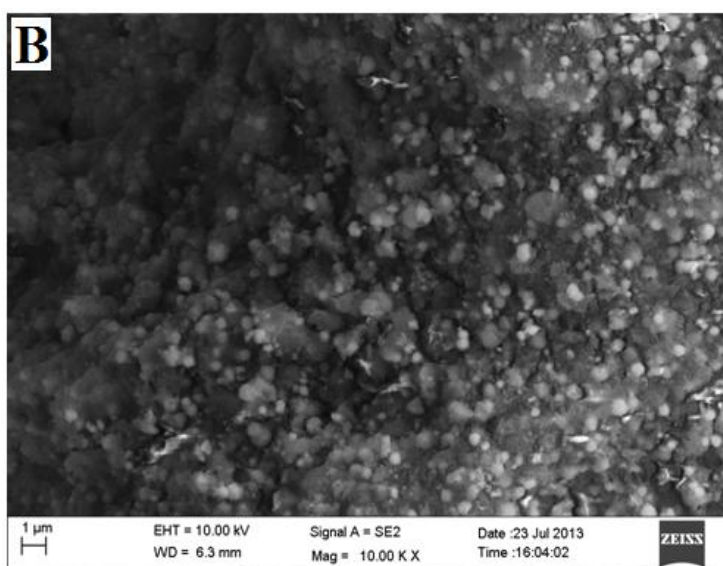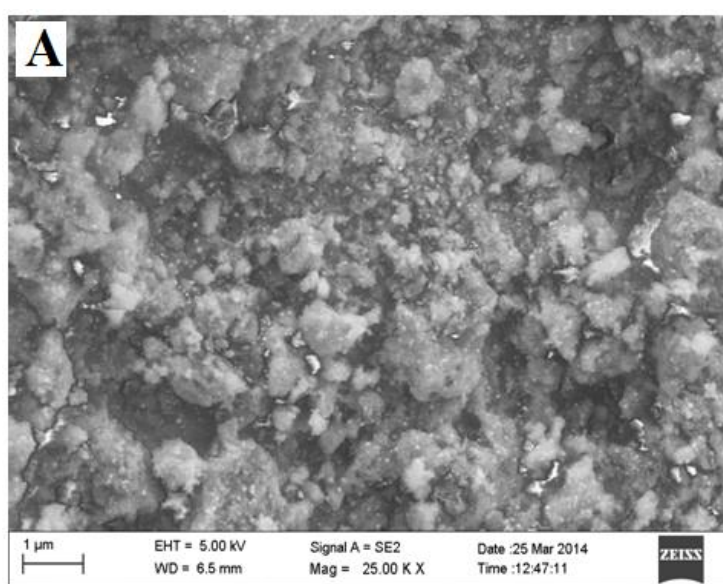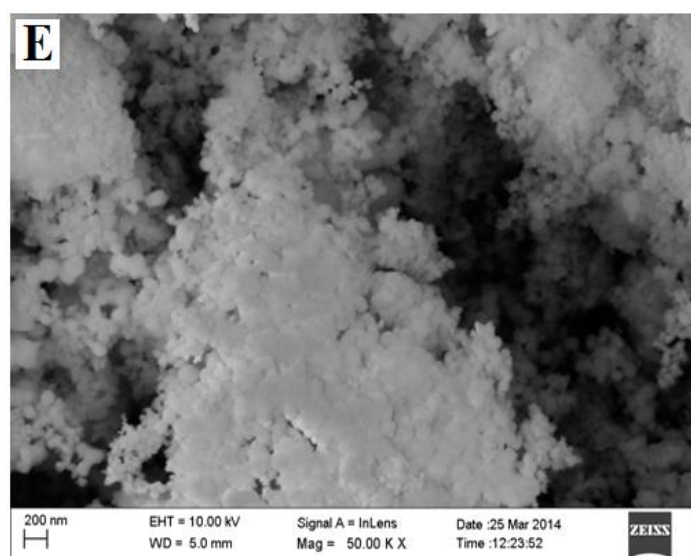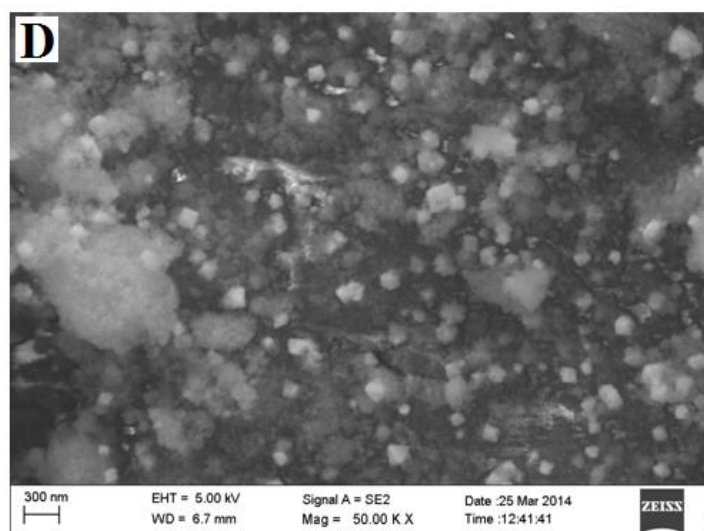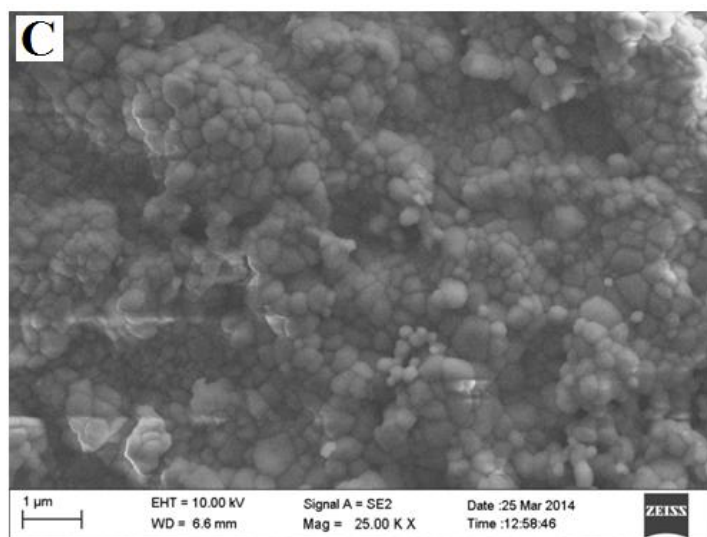
Figure 3.6: SEM images of calcined catalysts. A. 4.3NiAl, B. 4.3CoAl, C. 4.3MoAl, D. 4.3NiSi, and E. 4.3NiZr catalysts.
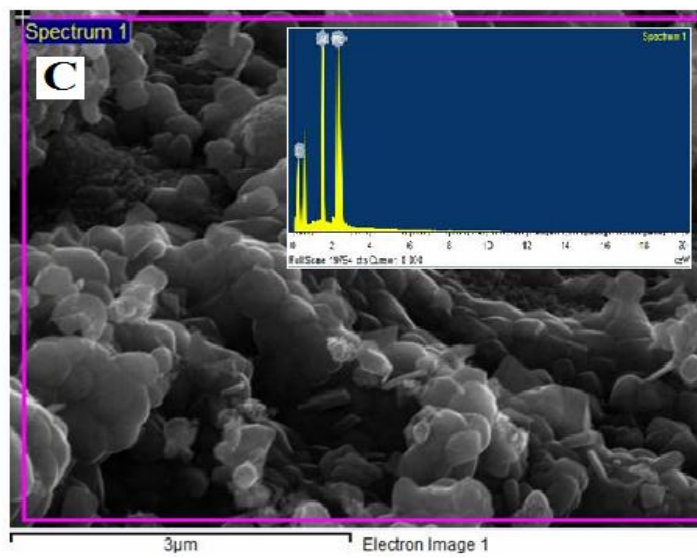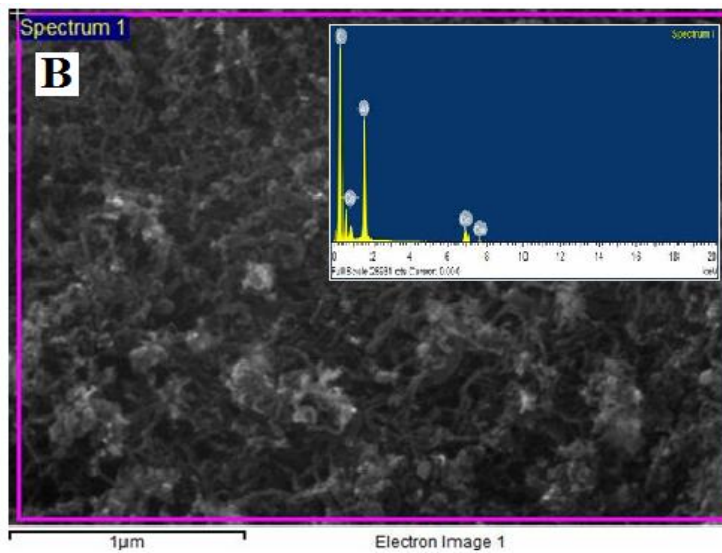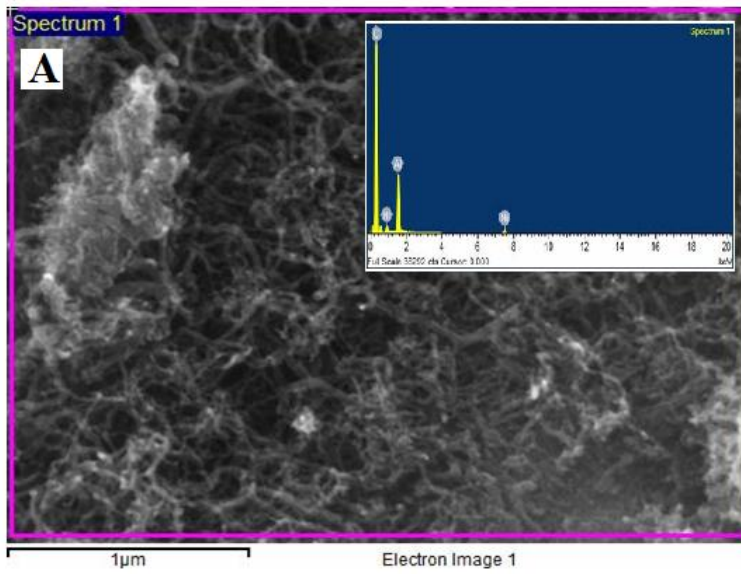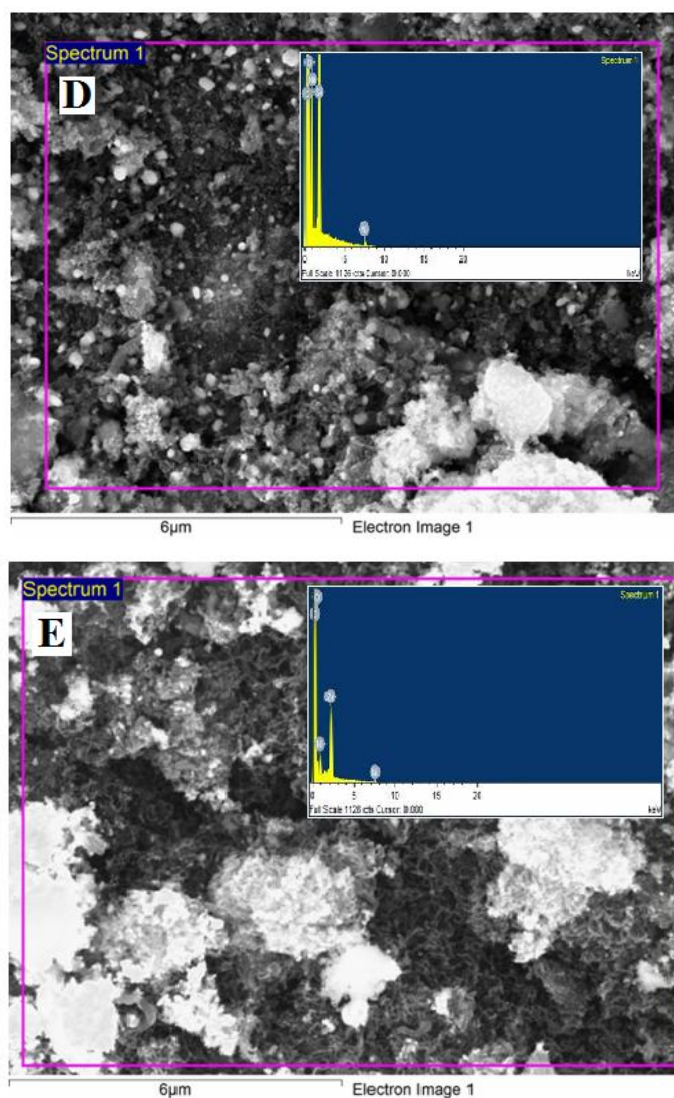
Figure 3.7: SEM images of spent catalysts. A. 4.3NiAl, B. 4.3CoAl, C. 4.3MoAl, D. 4.3NiSi, and E. 4.3NiZr catalysts. SR conditions: 923 K, SCMR = 2.2, WHSV = 6.62 h^{-1}.

3.3.5 Powder XRD

Powder XRD patterns of selected spent catalysts were acquired without any pretreatments as shown in Figure 3.8. The powder XRD patterns of spent γ-Al$_2$O$_3$, SiO$_2$ and ZrO$_2$ supported nickel catalysts showed features of nickel and respective supports only. The nickel peaks were observed at 2θ of 44.72° (1 1 1), 51.89° (2 0 0), and 76.33° (2 2 0) (PDF#701849). On the contrary, powder XRD patterns of spent γ-Al$_2$O$_3$ supported cobalt and molybdenum catalysts exclusively exhibited characteristic peaks of cobalt and molybdenum oxides respectively. The Co$_3$O$_4$ peaks were observed at 2θ of 31.37° (2 2 0), 36. 99° (3 1 1), 44.99° (4 0 0), 59.32° (5 1 1), and 65.38° (4 4 0) (PDF#781970). In case of spent 4.3MoAl, both

molybdenum trioxide (2θ of 25.88° (0 4 0)) and molybdenum dioxide (2θ of 36.99° (2 0 0) and 53.43° (2 2 2)) peaks were detected (PDF#895108 & PDF#761807). These results clearly suggested that cobalt and molybdenum oxidized during SR of isobutanol and vice versa. Therefore, it can be concluded that catalytic activity of cobalt and molybdenum may also depends on rates of oxidation-reduction cycle of metal-metal oxide during SR of isobutanol.
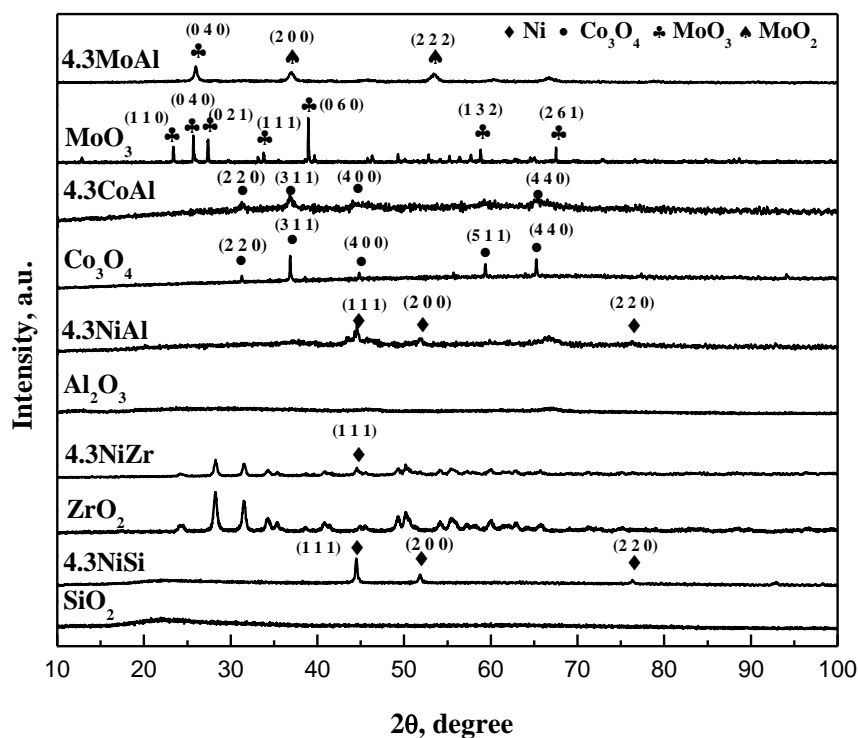
Figure 3.8: Powder XRD patterns of spent 4.3NiAl, 4.3CoAl, 4.3M0Al, 4.3NiSi, and 4.3NiZr catalysts. SR conditions: 923 K, SCMR = 2.2, and WHSV = 6.62 h^{-1}.

3.3.6 FTIR spectroscopy studies

FTIR spectra of spent catalysts were collected under ambient condition without any further treatment as shown in Figure 3.9. The IR bands appeared at ~2924 and ~2850 cm^{-1} for all spent catalysts were assigned to C-H (νC-H) bond vibration of aliphatic group [96,97]. The IR bands observed for spent 4.3NiAl and 4.3NiZr at ~2960-2970, 2874, 1470-1480, 1410-1420, and 1360-1370 cm^{-1} (ν(CH), ν_{as}(COO$^-$), δ(CH) and ν_s(COO$^-$)) were due to adsorbed formate species. The IR bands at 1560-1590 cm^{-1} together with ~1470-1480 and 1360-1370 cm^{-1} (ν_{as}(COO$^-$), ν_s(COO$^-$) and δ_s(CH$_3$)) were due to adsorbed acetate species. A strong IR band observed at ~1630 cm^{-1} was assigned to C=C bond vibration (ν_s(C=C)) [96][97]. The

evolution of IR band for C=C bond vibration proves presence of unsaturated hydrocarbon precursor which are responsible for formation of carbonaceous deposits on the catalysts.
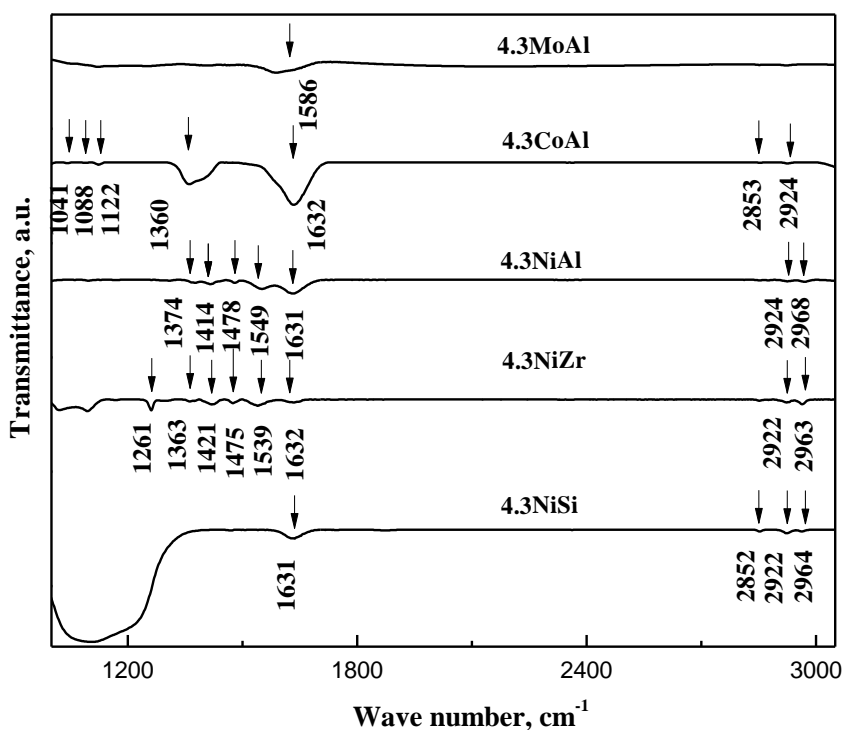
Figure 3.9: FTIR spectra of spent 4.3NiSi, 4.3NiZr, 4.3NiAl, 4.3CoAl, and 4.3MoAl catalysts.

3.3.7 Thermo gravimetric analysis

Spent catalysts were analysed by Thermo gravimetric analyser to determine the amount of coke present in the spent catalyst as shown in Figure 3.10. As presented in the figure, different behaviour of thermograms was noticed for different metals. Weight loss below 573K was because of desorption of the water and above 773K was because of the oxidation of carbon to CO and CO_2 gases. There was a weight gain/shift in the base line under inert atmosphere which can be explained as the inhomogeneity of the starting material and convective effects during the analysis [98]. There is a sharp decrease in the thermo gram of all catalysts when air was injected. This behaviour is because of the oxidation of amorphous coke which can be easily oxidized in presence of air. In case of 4.3MoAl, after oxidation of the amorphous coke, a slow decrease in the weight was observed which may be because of

vaporization of liquid MoO_2 (melting point of MoO_2 is 1068 K). Carbon content was found in the order of 4.3CoAl (0.4%) ~ 4.3MoAl (0.4%) < 4.3NiAl (1.1%)
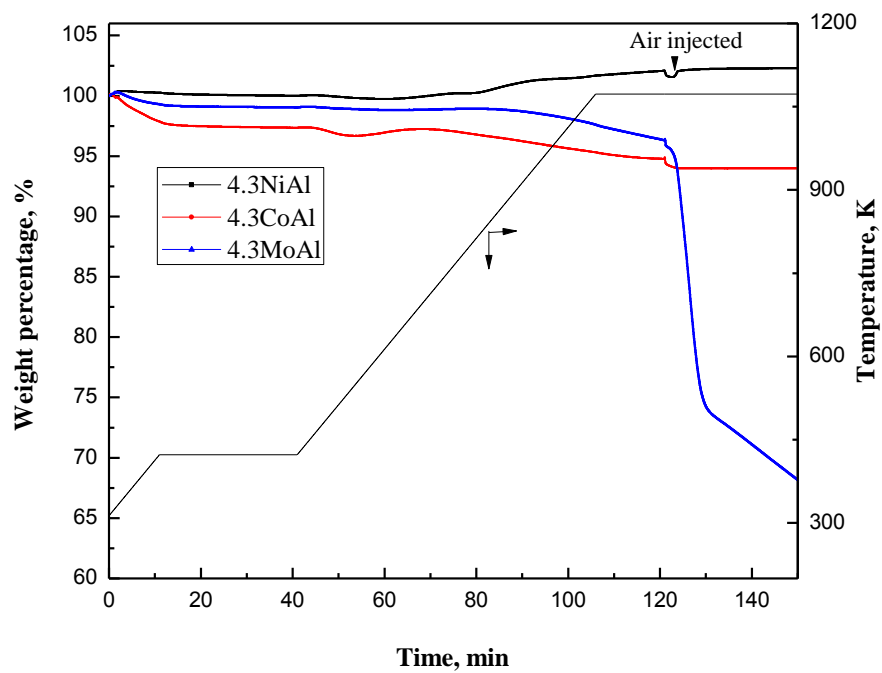
Figure 3.10: TGA of spent 4.3NiAl, 4.3CoAl, and 4.3MoAl catalysts.

Chapter 4

Steam reforming of isobutanol over Ni/γ-Al$_2$O$_3$ and Co/γ-Al$_2$O$_3$ catalysts

The γ-Al$_2$O$_3$ supported nickel and cobalt demonstrated promising catalytic activity for SR of isobutanol as observed in the previous chapter. A systematic investigation of SR of isobutanol was thus carried out over γ-Al$_2$O$_3$ supported nickel (xNiAl where x=1.9 to 5.7 mmol) and cobalt (xCoAl where x=3.0-7.3 mmol) catalysts of varying nickel and cobalt contents respectively. The effects of various process parameters such as temperature, SCMR, and WHSV on hydrogen yield and selectivity to CO, CO$_2$ and CH$_4$ were studied to obtain an optimum process conditions. Moreover, thermodynamic equilibrium analysis of SR of isobutanol was carried out under the experimental conditions using Aspen Plus and equilibrium composition was compared with experimental results.

4.1   Steam reforming of isobutanol over Ni/γ-Al$_2$O$_3$ catalysts

4.1.1   Catalyst characterization

4.1.1.1   Surface area, pore volume and chemisorption

The SA and PV of both fresh and reduced catalysts and MD and SM of reduced catalysts are shown in Table 4.1. The SA and PV of both fresh and reduced catalysts decreased with increasing nickel loading. With increasing nickel loading, the surfaces of the γ-Al$_2$O$_3$ support is covered by increased numbers of nickel crystallites that causes increased coverage of surface of pores leading to decreasing trends of SA and PV. The decrease in SA may be due to the blockage of the pores by deposition of nickel during incipient wetness impregnation method. The highest MD of 1.22% was observed for 1.9NiAl catalyst.

Table 4.1: Physicochemical properties of the prepared catalysts.

catalysts	BET				chemisorption		TPR	H_2 consumed, µmol/g	d_C	
	cal		red							
	SA	PV	SA	PV	MD	SM	T_{max}		cal	red
γ-Al$_2$O$_3$	240	0.8	240	0.8	-	-	-		-	-
1.9NiAl	211	0.7	209	0.74	1.22	8.2	746	5587.4	8.3	8.9
3.0NiAl	196	0.6	190	0.67	0.98	6.5	726		10.6	10.4
4.3NiAl	181	0.5	172	0.58	0.84	5.6	751	8517.6	12.2	13.8
5.7NiAl	164	0.5	161	0.54	1.01	6.7	776	11404.5	15.7	15.3

SA = surface area, m^2/g; PV = pore volume, cm^3/g; MD = metal dispersion, %; SM =metallic surface area, m^2/g metal; T_{max} = maximum reduction temperature; d_C =crystallite size by XRD, nm.

4.1.1.2 Temperature programmed reduction

TPR profiles of the calcined catalysts are shown in Figure 4.1. The temperature corresponding to the maximum hydrogen consumption (or T_{max}) for the catalysts was observed in the range of 748-823 K. For all the catalysts, the lower temperature reduction peak corresponds to the reduction of bulk NiO reducible species. For higher nickel loading, a small peak appeared at higher temperature (908 K) may be due to the formation of dispersed NiAl$_2$O$_4$ species which are not detectable by powder XRD [99]. In all experimental runs, the supported metal oxide catalysts were reduced in FBR at 923 K prior to SR reaction to ensure complete reduction.
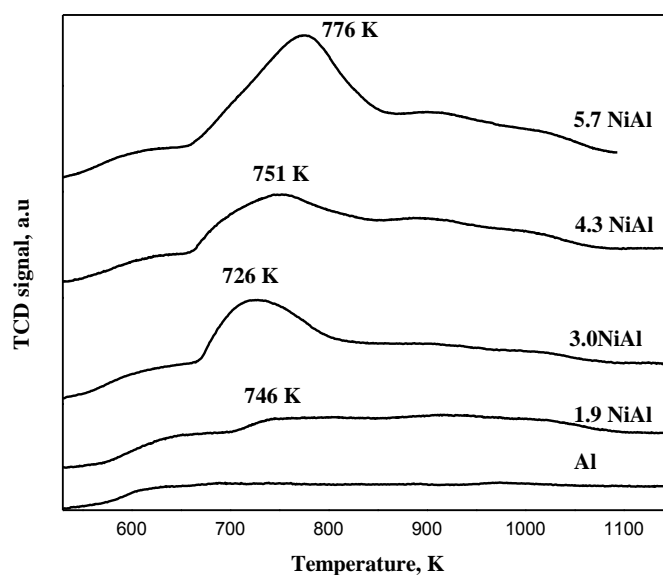
Figure 4.1: TPR profiles of calcined catalysts.

4.1.1.3   Powder XRD

The powder XRD patterns of the calcined and reduced catalysts are shown in Figure 4.2. The powder XRD patterns of support, γ-Al_2O_3, are also shown in the same figure. As observed from the figure, the peaks corresponding to 2θ of $45.78°$ and $66.55°$ were due to Al_2O_3 (PDF#821399). The peaks corresponding to 2θ of $37.34°$, $43.36°$, and $63.03°$ are due to the presence of nickel oxide species (Figure 4.2A) (PDF#731523). The peaks corresponding to 2θ of $44.43°$, $51.78°$, and $76.33°$ are due to the presence of nickel species (Figure 4.2B) (PDF#870712). The peak corresponding to 2θ of $37.21°$ observed for reduced catalyst at higher nickel loadings ($\geq$4.3 mmol nickel) is due to the bulk NiO species. It was also observed that the sharpness of the nickel peaks enhanced with increasing nickel loadings. From these results it may be concluded that the nickel remained in dispersed form on high surface area γ-Al_2O_3 at low nickel loading and nickel crystals started forming with increasing nickel loading. The calcined and reduced catalysts with different nickel loading showed the characteristic nickel oxide/nickel peaks corresponding to (1 1 1), (2 0 0), and (2 2 0) crystal planes. The average crystallite size of nickel and nickel oxide of reduced and calcined catalysts with different nickel loadings were determined using the Scherrer's equation from the FWHM of the XRD peaks corresponding to (1 1 1), (2 0 0) and (2 2 0) crystal planes as shown in Table 4.1. The dimensions of nickel and NiO crystallites were in the range 8.3–

(44)

15.7 nm.
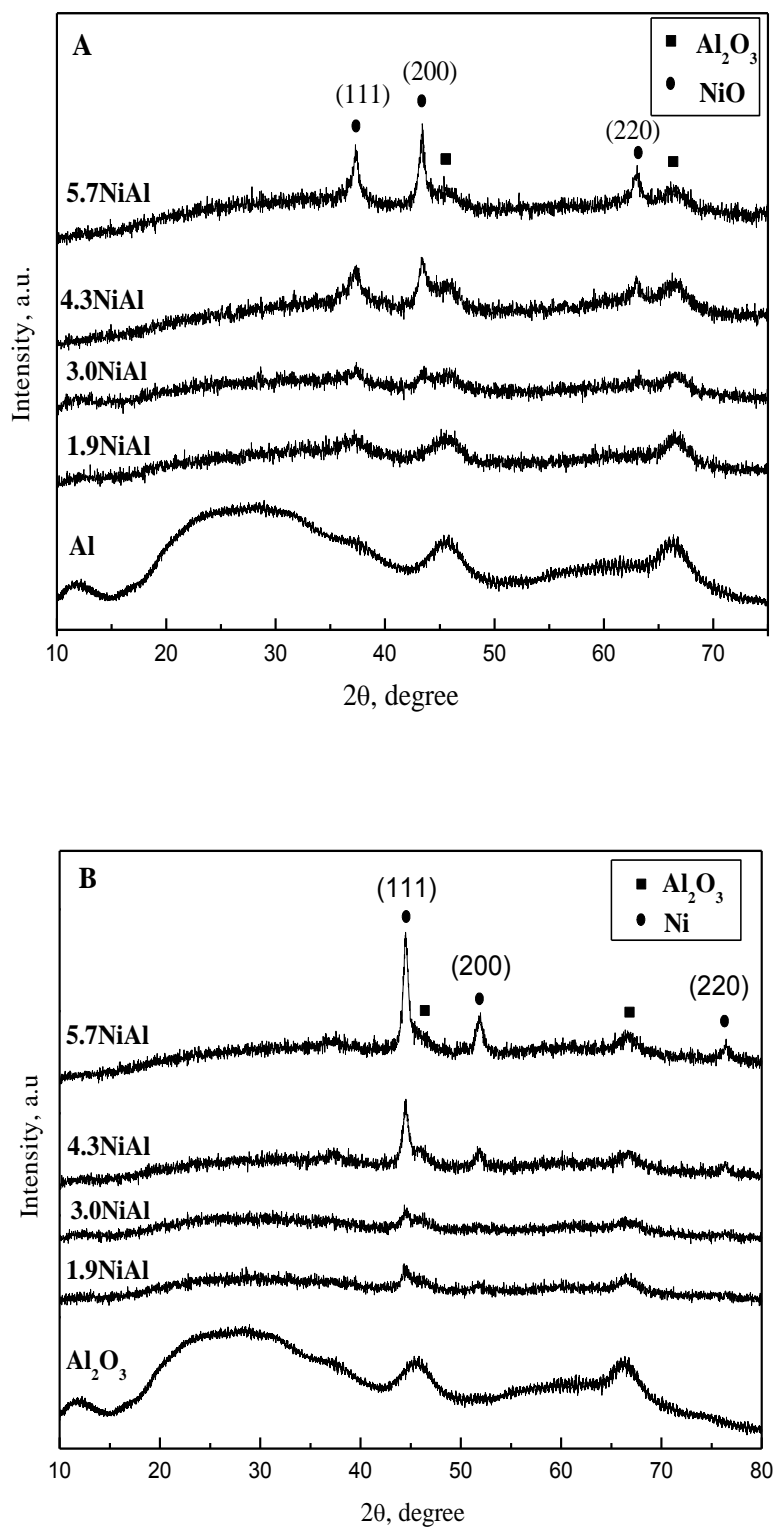
Figure 4.2: Powder XRD patterns of (A) calcined and (B) reduced catalysts.

4.1.2 Results and discussion

The experiments of isobutanol SR were carried out in a FBR using Ni/γ-Al$_2$O$_3$ catalysts under atmospheric pressure in wide ranges of temperature (773–923 K), SCMRs (1–3), and WHSVs (9.35–37.43 h^{-1}). H$_2$, CO, CO$_2$, and CH$_4$ were identified as the non-condensable gaseous products. The analysis of liquid samples by GC-FID and GC-MS revealed the formation of a large number of chemical compounds including acetaldehyde, propionaldehyde, 2-propenal, butyraldehyde, 2-butanone, and butanols (1, 2, and isobutanols), especially at low CCGP. A representative mole balance table displaying the flow rates of the feed and gaseous and liquid products is presented in Table 4.2.

Table 4.2: Carbon balance table for SR of isobutanol[a].

catalysts	gas products flow rates, mol h^{-1}				liquid products flow rates×10^3, mol h^{-1}						CBE	CIB	H$_2$/Bu
	H$_2$	CO	CH$_4$	CO$_2$	ACE	PPD	PPL	BUD	BUN	BU			
4.3NiAl	0.406	0.052	0.025	0.108	0.01	0.03	0.02	0.03	0.03	3.2	9.4	93.8	8.3

ACE = acetaldehyde, PPD = propionaldehyde, PPL= 2-propenal, BUD = (*n*- and iso-) butyraldehyde, BUN = 2-butanone, BU = 1-, 2-, and iso-butanol; CBE = carbon balance error, %, CIB= Conversion of Isobutanol, %.
[a] isobutanol = 0.052 mol h^{-1}, H$_2$O = 0.9 mol h^{-1}, and N$_2$ = 0.143 mol h^{-1}. Conditions: 873 K, SCMR=2.47, WHSV = 7.02 h^{-1}.

4.1.2.1 Time-on-stream behavior of 3.0NiAl

The stability of 3.0NiAl catalyst for SR of isobutanol was studied for about 10 h of TOS at 823 K with SCMR of 1.96 and WHSV of 28.01 h^{-1}. The CCGP, hydrogen yield, selectivity to CO, CO$_2$, and CH$_4$ stabilized within 150 min of TOS as shown in Figure 4.3. Beyond 150 min, the CCGP and compositions of gaseous products remained practically constant up to more than 10 h of TOS. From this result, it may be concluded that Ni/γ-Al$_2$O$_3$ catalyst is quite stable for SR of isobutanol. For all subsequent experiments, the steady state experimental data were collected after 150 min of TOS.
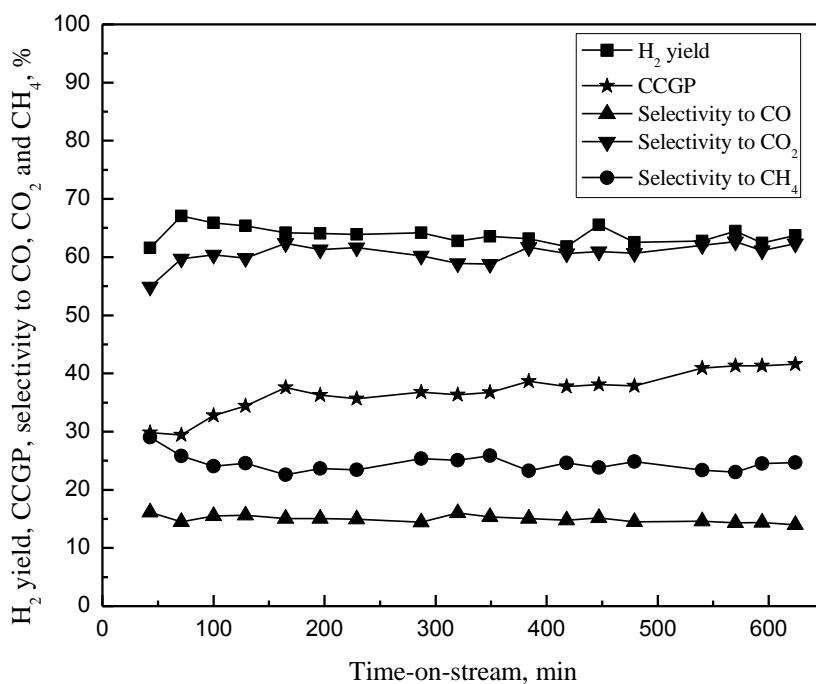
Figure 4.3: Time-on-stream behavior of the Ni/γ-Al$_2$O$_3$ catalyst. Conditions: 3.0NiAl, 823 K, SCMR=1.96, WHSV=28.01 h^{-1}.

4.1.2.2   Effect of weight hourly space velocity

The effects of WHSV were studied over 3.0NiAl catalyst at 873 K with SCMR of 1.47 as shown in Figure 4.4. The CCGP decreased with increasing WHSV. This is because of decrease of residence time of the reactants and products in the reactor. The hydrogen yield increased slightly with increasing WHSV. With an initial increase of WHSV, the selectivity to CO and CH$_4$ decreased and that of CO$_2$ increased slightly. However, the selectivity to CO, CO$_2$, and CH$_4$ practically remains unaffected beyond WHSV of ~15 h^{-1}. The identical trends of results were also reported for SR of *n*-butanol [69] and OSR of ethanol [100]. Therefore, the remaining studies were performed with WHSV more than 15 h^{-1} for better comparison of selectivity to CO, CO$_2$, and CH$_4$.
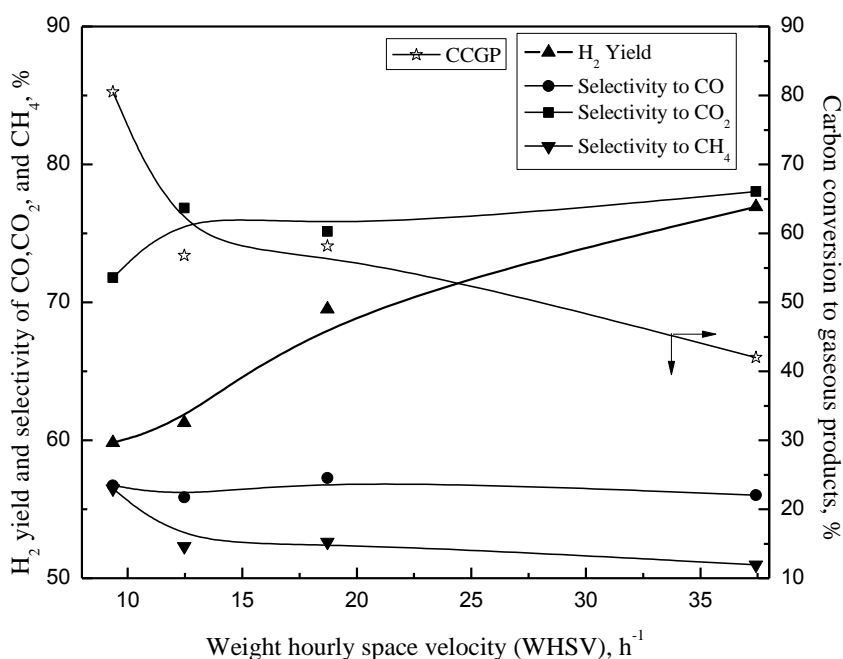
Figure 4.4: Effect of WHSV on CCGP, H_2 yield, and selectivity to CO, CO_2, and CH_4. Conditions: 3.0NiAl, 873 K, SCMR= 1.46.

4.1.2.3   Effect of nickel loading on γ-Al$_2$O$_3$

The three different nickel loaded γ-Al$_2$O$_3$ catalysts, 1.9NiAl, 4.3NiAl, and 5.7NiAl were examined for SR of isobutanol at 773 K with SCMR of 2.49 and WHSV of 28.25 h^{-1}. To delineate the role of the support for SR of isobutanol, the study was also conducted with pure γ-Al$_2$O$_3$ under identical experimental conditions. A very low CCGP was observed with pure γ-Al$_2$O$_3$ suggesting that pure γ-Al$_2$O$_3$ is inactive for SR of isobutanol under the experimental condition. The effects of nickel loading on γ-Al$_2$O$_3$ on CCGP, H_2 yield, and selectivity to CO, CO_2, and CH_4 are shown in Table 4.3. As observed from the table, the CCGP increased with increasing nickel loading on γ-Al$_2$O$_3$. The increase of catalytic activity with increasing nickel loading on γ-Al$_2$O$_3$ is due to increased number of active sites in the catalyst. The hydrogen yield also increased with increasing nickel loading on γ-Al$_2$O$_3$. The maximum hydrogen yield of about 84% was observed with 5.7NiAl. The selectivity to CO, CO_2, and CH_4 remained almost unaffected with increasing nickel loading on γ-Al$_2$O$_3$.

Table 4.3: Effect of nickel loading on γ-Al$_2$O$_3$ on CCGP, H$_2$ yield and selectivity to CO, CH$_4$, and CO$_2$.

catalysts	CCGP, %	H$_2$ yield, %	selectivity, %		
			CO	CO$_2$	CH$_4$
γ-Al$_2$O$_3$	0.49	31.67	0	97.63	2.37
1.9NiAl	31.20	64.49	9.87	64.2	25.93
4.3NiAl	84.75	65.94	4.54	58.64	36.82
5.7NiAl	100.00	84.49	5.86	67.4	26.74

[a]Conditions: 773 K, SCMR=2.49, WHSV=28.25 h^{-1}

4.1.2.4 Effect of steam-to-carbon mole ratio

The effects of SCMR on CCGP, hydrogen yield, and selectivity to CO, CO$_2$, and CH$_4$ were studied in the SCMR range of 1.1-3.2 at 873 K over 3.0NiAl catalysts with WHSV of 18.08 h^{-1} as shown in Figure 4.5.
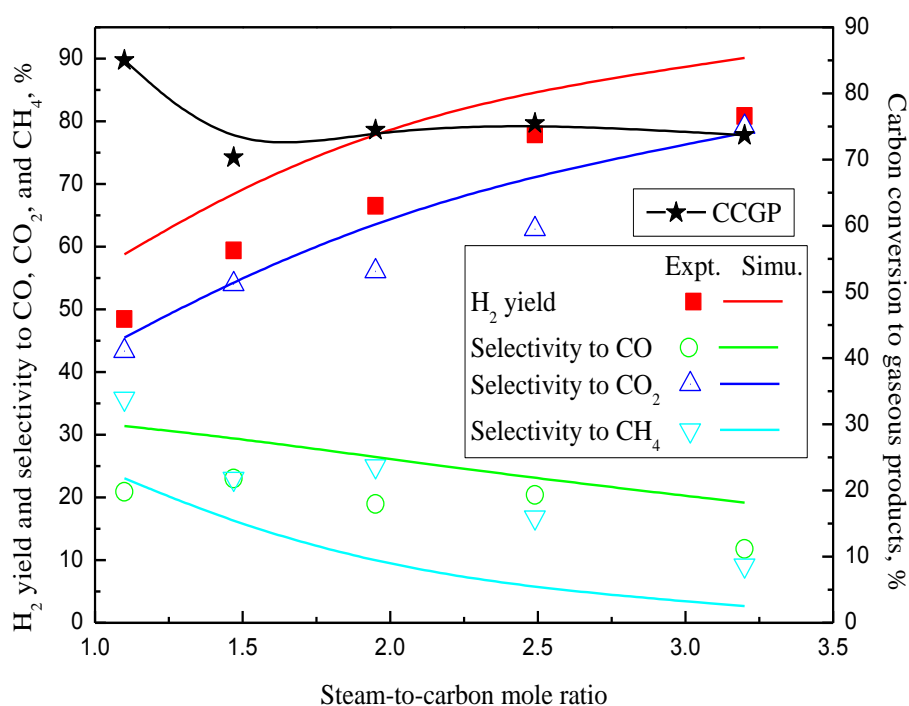
Figure 4.5: Effect of steam-to-carbon mole ratio on CCGP, H$_2$ yield, and selectivity to CO, CO$_2$, and CH$_4$. Conditions: 3.0NiAl, 873 K, WHSV=18.08 h^{-1}.

(49)

About 75% of CCGP was observed under experimental conditions. The hydrogen yield increased with increasing SCMR as observed from the figure. The maximum hydrogen yield of about 81% was observed with SCMR of 3.2. With increasing SCMR, the increase of selectivity to CO_2 and decrease of selectivity to CO and CH_4 were observed. With increasing SCMR, the WGSR (Eq.(ii) of **Error! Reference source not found.**), butanol (Eq.(i) of **Error! Reference source not found.**) and methane (reverse reaction of Eqs.(iv-v) of **Error! Reference source not found.**) SR reactions increases leading to increase in hydrogen yield and selectivity to CO_2 and decrease in selectivity to CO and CH_4. Hu and Lu also reported similar trends of results for SR of acetic acid over Ni/Al_2O_3 catalyst [58].

The study was further extended to thermodynamic equilibrium analysis of SR of isobutanol using R-Gibbs reactor with UNIF-LBY as property method using Aspen Plus under the identical experimental conditions. H_2, CO, CH_4, CO_2, isobutanol, water, 1-butanol, 2-butanol, butyraldehyde, isobutyraldehyde, propenal, propionaldehyde, acetaldehyde, 2-butanone and carbon were the components considered in the analysis. The results of thermodynamic equilibrium analysis of SR of isobutanol were then compared with experimental data as shown in Figure 4.5. The experimental trends of results displayed good agreement with that of thermodynamic equilibrium analysis results. However, the hydrogen yield and selectivity to CO was somewhat lower than that of equilibrium values. The selectivity to CH_4 was observed to be higher than that of equilibrium selectivity. From these results it may be concluded that reactions involved in SR of isobutanol (especially WGSR and methane SR reaction) remained slightly away from the equilibrium under the experimental conditions studied.

4.1.2.5   Effect of temperature

The effect of temperature on CCGP, hydrogen yield, and selectivity to CO, CO_2, and CH_4 was studied in the temperature range of 773-923 K over 3.0NiAl catalyst with SCMR of 1.47 and WHSV of 17.0 h^{-1} as shown in Figure 4.6. The CCGP increased with increasing temperature. The endothermic SR reactions (of isobutanol and intermediates) are favoured at higher temperature that results in an increase of CCGP with temperature. The hydrogen yield increased marginally with increasing temperature and the maximum hydrogen yield of ~65% was observed at 923 K. The increase of hydrogen yield is due to increase in CCGP and favourable endothermic SR of methane (reverse of Eqs.(iv-v) of **Error! Reference source not found.**)

(50)

at higher temperature. The increase of selectivity to CO and decrease of selectivity to CO_2 was observed with increasing temperature. A slight decreasing trend of selectivity to methane with temperature was also witnessed.
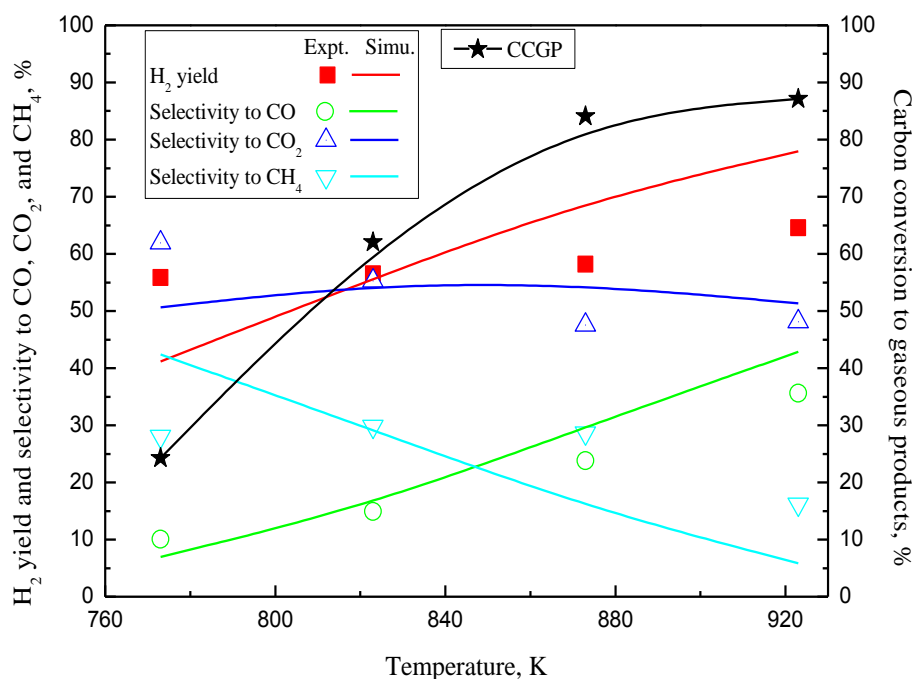
Figure 4.6: Effect of temperature on CCGP, H_2 yield, and selectivity to CO, CO_2, and CH_4. Conditions: 3.0NiAl, SCMR=1.46, WHSV=18.72 h^{-1}.

The trends of results can be explained by the fact that endothermic SR of isobutanol (Eq.(i) of **Error! Reference source not found.**), reverse methanation reaction (Eqs.(iv-v) of **Error! Reference source not found.**), and reverse WGSR (Eq.(ii) of **Error! Reference source not found.**) are favoured at higher temperature. The experimental results of the present study were found to be comparable with SR of oxygenated compounds like acetic acid in presence of Ni/Al_2O_3 [58]. Furthermore, the thermodynamic equilibrium analysis of SR of isobutanol was performed at different temperature under the experimental conditions and the results were then compared with experimental data as shown in Figure 4.6. As observed from the figure, the trends of experimental results are in good agreement with equilibrium results. The trends of thermodynamic results were also matched well with published literature [64]. However, the reactions involved in SR of isobutanol are away from the equilibrium to some extent causing somewhat lower hydrogen yield and selectivity to CO and CO_2 and higher selectivity

to CH_4 compared to equilibrium.

4.1.2.6   Optimum conditions

The optimum process conditions were determined to achieve complete CCGP and maximum hydrogen yield with very low selectivity to methane [82,83]. The CCGP depends on reactivity of the catalysts and WHSV. The catalytic activity on the other hand is a strong function of nickel loading on γ-Al_2O_3 (Table 4.3). Therefore, the maximum allowable nickel loading on γ-Al_2O_3 (generally 25-30 wt%) should be used as catalyst with appropriate WHSV to achieve complete CCGP. The hydrogen yield and selectivity to methane depends strongly on SCMR and temperature. With increasing SCMR and temperature, the hydrogen yield increases and selectivity to methane decreases (Figure 4.5 & Figure 4.6). The high SCMR is also desirable to minimize coke formation on the catalyst. From this discussion it may be apparently concluded that maximum permissible SCMR and temperature should be used to achieve maximum hydrogen yield with low selectivity to methane. However, the operation of SR at high temperature and SCMR will affect the thermal efficiency of the process significantly. Therefore, it may be concluded that optimum process conditions of SCMR= 2.5-3.0 and temperature = ~900 K should be used for SR of isobutanol. Similar optimum conditions were also reported earlier [67].

4.2 Steam reforming of isobutanol over Co/γ-Al₂O₃ catalysts

4.2.1 Catalyst characterization

4.2.1.1 Surface area, pore volume, and chemisorption

The SA and PV of calcined and reduced catalysts, MD and SM of reduced catalysts are shown in Table 4.4. The SAs of both calcined and reduced catalysts were somewhat lesser than corresponding pure supports. The decrease of SA with impregnation of metals on the supports might be due to coverage of surfaces and blockage of pores of supports by metal or metal oxide. For γ-Al₂O₃ supported cobalt catalysts, SAs decreased with increasing cobalt loadings on γ-Al₂O₃ as observed from the table.

Table 4.4: Physicochemical properties of the catalysts.

catalysts	BET				chemisorption		XRD	TPR	H_2 consumed (μmol/g)
	cal		red						
	SA	PV	SA	PV	MD	SM	d_c	T_{max}	
γ-Al₂O₃	228	0.84	-	-	-	-	-	-	
3.0CoAl	175	0.64	180	0.69	0.30	2.07	15.1	775, 874, 942	1955.7
4.3CoAl	166	0.58	163	0.59	0.29	2.01	19.2	752, 877, 942	2437.7
5.7CoAl	151	0.53	149	0.53	0.18	1.22	23.4	748, 881, 942	3535.5
7.3CoAl	138	0.48	135	0.49	0.17	1.15	60.7	745, 885, 942	5016.8

cal =calcined; red = reduced, SA = BET surface area, m^2/g; PV =pore volume, cm^3/g; MD= metal dispersion, %; SM= metallic surface area, m^2/g metal; d_c=metal crystallite size, nm; T_{max} = maximum reduction temperature, K.

The PVs also decreased marginally with increasing cobalt loading on γ-Al₂O₃ for both calcined and reduced catalysts. The trends of SA and PV results were analogous and hence statements used to explain trends of SA are applicable for PV as well. MD and SM decreased consistently with increasing cobalt loading on γ-Al₂O₃ as observed from the table. The decline of MD and SM was due to enrichment of cobalt agglomerates/bulk cobalt with

increasing cobalt loadings on γ-Al$_2$O$_3$.

4.2.1.2 Temperature programmed reduction

TPR profiles of pure support and calcined catalysts are shown in Figure 4.7. TPR profiles of bulk metal oxide are also shown in the same figure as reference. γ-Al$_2$O$_3$ showed no reduction peaks thereby confirming that pure support is not reducible under the ranges of temperature. Calcined γ-Al$_2$O$_3$ supported cobalt catalysts are known to reduce in two separate stages.
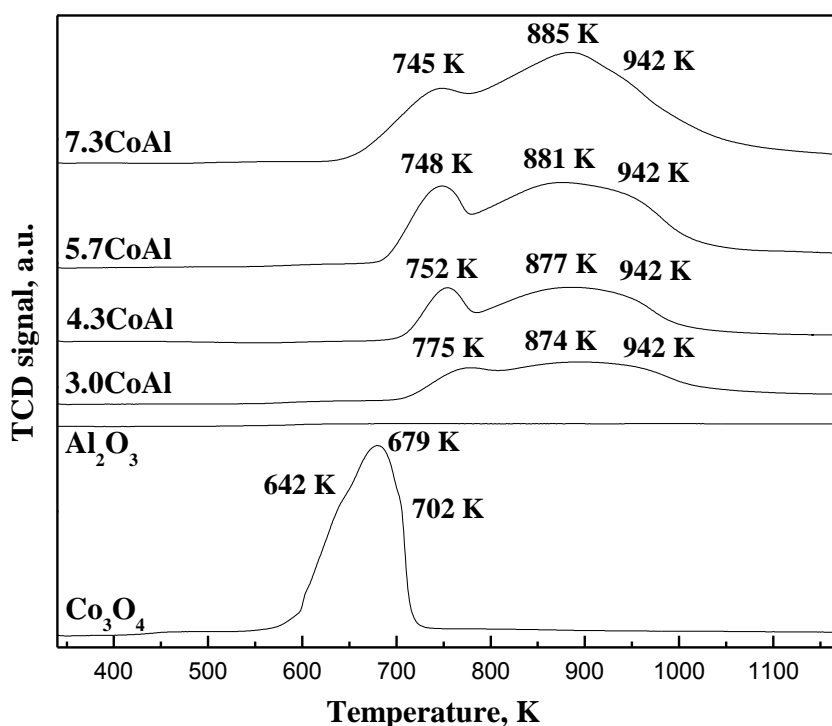
Figure 4.7: TPR profiles of Co$_3$O$_4$, γ-Al$_2$O$_3$, 3.0CoAl, 4.3CoAl, 5.7CoAl, and 7.3CoAl.

Three distinct reduction peaks were observed for calcined γ-Al$_2$O$_3$ supported cobalt catalysts at 745-775, 874-885, and 942 K. The first two peaks were associated with reduction of various surface cobalt species; whereas peak at 942 K was due to reduction of CoAlO$_4$ spinel [86]. TPR profile of bulk cobalt oxide also showed three different reduction peaks at 642, 679 and 702 K [87]. The peak at 679 K was due to reduction of CoO to metallic cobalt; while peaks at 642 and 702 K were due to reduction of Co$_3$O$_4$ to metallic cobalt [86]. It was further observed that reduction peaks at 745-775 K and 874-885 K moved progressively to lower and

higher temperature respectively with increasing cobalt loading on γ-Al$_2$O$_3$. The shifting of reduction peaks relative to bulk cobalt oxides peaks may be due to weak interaction of cobalt oxides with γ-Al$_2$O$_3$ and extents of different bulk cobalt oxides species depending on cobalt loading on γ-Al$_2$O$_3$.

4.2.1.3   Powder XRD

Powder XRD patterns of calcined catalysts together with pure supports are shown in Figure 4.8. Powder XRD patterns of bulk metals oxide are also shown in the same figure as quick references. Powder XRD patterns of calcined γ-Al$_2$O$_3$ supported cobalt catalysts exhibited representative peaks of bulk cobalt oxide (Co$_3$O$_4$) at 2θ of 31.37° (2 2 0), 36.99° (3 1 1), 44.99° (4 0 0), 59.32° (5 1 1), and 65.38° (4 4 0) (PDF#781970).
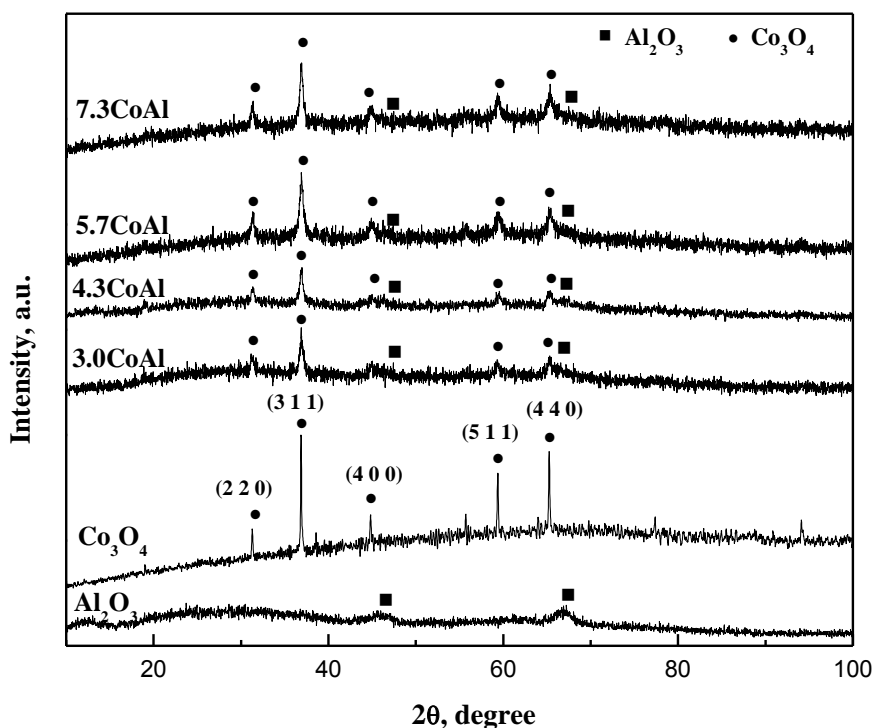
Figure 4.8: Powder XRD patters of calcined catalysts: γ-Al$_2$O$_3$, CO$_3$O$_4$, 3.0CoAl, 4.3CoAl, 5.7CoAl, and 7.3CoAl.

From above observations, it may therefore be concluded that calcined catalysts were associated with corresponding bulk metal oxides in their structure. Powder XRD patterns of the reduced catalysts are shown in Figure 4.9. Powder XRD patterns of pure supports

(55)

(calcined at 923 K) were also compared with that of reduced catalysts to avoid difficulty in identification of metals/metals oxide peaks. For reduced γ-Al$_2$O$_3$ supported cobalt catalysts, two distinct cobalt crystallite peaks were observed at 2θ of 44.29° (1 1 1) and 75.95° (2 2 0) (PDF#894307). 5.7CoAl and 7.3CoAl however showed an additional peak at 2θ of 51.28° (4 0 0) due to formation of Co$_2$AlO$_4$. This result clearly suggests that fraction of cobalt formed solid solution with alumina matrix especially at higher cobalt loadings on γ-Al$_2$O$_3$.

The metals oxide peaks were however not detected in powder XRD patterns of reduced γ-Al$_2$O$_3$ supported cobalt catalysts of different cobalt loadings on γ-Al$_2$O$_3$. This result indicates that cobalt oxides are completely reducible at reduction temperature of 923 K. Cobalt crystallite sizes increased with increasing cobalt loading on γ-Al$_2$O$_3$ in the case of reduced γ-Al$_2$O$_3$ supported cobalt catalysts as shown in Table 4.4. The trends metal crystallite size obtained from powder XRD were fully concurring with MD obtained from H$_2$ pulse chemisorption.
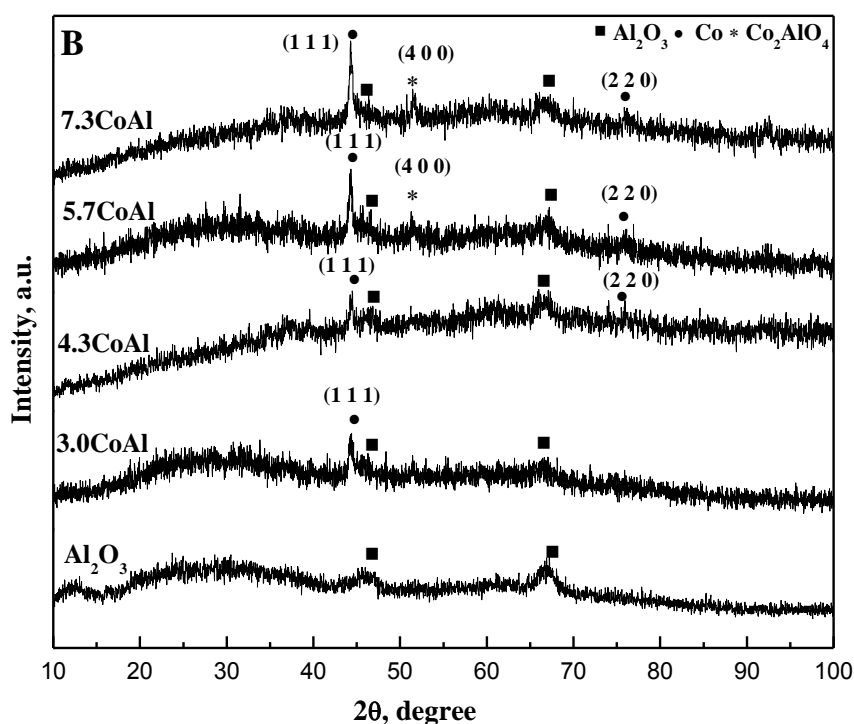
Figure 4.9: Powder XRD patterns of reduced catalysts. γ-Al$_2$O$_3$, 3.0CoAl, 4.3CoAl, 5.7CoAl, and 7.3CoAl.

4.2.2 Results and discussion

The SR of isobutanol was carried out in a FBR using Co/γ-Al$_2$O$_3$ catalysts under atmospheric pressure in the wide ranges of temperature (773–923 K), SCMRs (1.5–3). H$_2$, CO, CO$_2$, and CH$_4$ were identified as the non-condensable gaseous products. The analysis of liquid samples by GC-FID and GC-MS revealed the formation of a large number of chemical compounds including acetaldehyde, propionaldehyde, 2-propenal, butyraldehyde, 2-butanone, and butanols (1, 2, and isobutanols), especially at low CCGP. The molar flow rates of feeds, gaseous, and liquid products together with unreacted butanols (1, 2, and iso-butanols) for all runs are presented in Table 4.5. The carbon balance errors were also checked and errors were within ±10% for all experiments. Furthermore, two independent experiments were performed under identical experimental conditions to demonstrate reproducibility of results for SR of isobutanol as shown in Table 4.5. The results clearly showed that molar flow rate of products were comparable for both runs.

Table 4.5: Carbon balance table for SR of isobutanol.

catalysts	gas products flow rates, mol h^{-1}				liquid products flow rates$\times10^{3}$, mol h^{-1}						CBE	CIB	H$_2$/Bu
	H$_2$	CO	CH$_4$	CO$_2$	ACE	PPD	PPL	BUD	BUN	BU			
Effect of cobalt loading [a]													
3.0CoAl	0.404	0.101	0.002	0.080	0.0285	0.497	0.08	0	0.059	0.844	9.4	98.3	7.8
4.3CoAl	0.413	0.076	0.013	0.099	0.003	0.062	0	0	0.037	0.51	5.5	99.01	8.02
5.7CoAl	0.469	0.078	0.006	0.109	0.0004	0	0.01	0.0006	0.004	0.057	6.1	99.8	9.02
7.3CoAl	0.463	0.073	0.010	0.115	0.001	0.093	0.01	0.093	0.005	0.051	3.5	99.9	8.9
SCMR **Effect of steam-to-carbon mole ratio** [b]													
1.5	0.624	0.119	0.036	0.142	0.0008	0.0080	0.01	0.008	0.0035	0.055	3.9	99.9	8.7
2	0.512	0.09	0.020	0.125	0.0003	0.0009	0	0.0009	0.0005	0.0084	1.4	99.9	8.8
2.5[d]	0.480	0.077	0.014	0.115	0	0	0	1.6E-5	2.9E-6	6.3E-5	0.7	99.9	9.2
2.5[d]	0.464	0.073	0.011	0.115	0.001	0.0093	0.007	0.009	0.005	0.051	4.0	99.9	8.9
3.2	0.420	0.047	0.004	0.101	0	0	0	1.0E-5	8.3E-6	3.2E-5	2.2	99.9	10.7
Effect of temperature [c]													
773 K	0.307	0.012	0.069	0.103	0.0008	0.0225	0	0.002	0.0016	0.93	9.7	98.2	6.01
823 K	0.394	0.026	0.038	0.121	3.5E-6	0	0	3.3E-5	1.5E-6	0.827	9.5	98.4	7.6
873 K	0.462	0.049	0.037	0.115	0.0005	0.0001	0	0	0	0.003	2.8	99.9	8.8
923 K	0.480	0.077	0.014	0.115	0	0	0	1.6E-5	2.9E-6	6.3E-5	0.7	99.9	9.2

ACE = acetaldehyde, PPD = propionaldehyde, PPL= 2-propenal, BUD = (*n*- and iso-) butyraldehyde, BUN = 2-butanone, BU = 1-, 2-, and iso-butanol; CBE = carbon balance error, %, CIB= conversion of isobutanol, %

[a] isobutanol = 0.052 mol h^{-1}, H$_2$O = 0.83 mol h^{-1}, and N$_2$ = 0.14 mol h^{-1}. Conditions: 923 K, SCMR=2.2, WHSV = 6 h^{-1}.

[b] Conditions: 7.3CoAl, 923 K, WHSV= 6.5 h^{-1}, isobutanol flow rate = 0.071, 0.058, 0.052, and 0.039 mol h^{-1} and H$_2$O flow rate = 0.73, 0.8, 0.9, and 0.86 mol h^{-1} for SCMR of 1.5, 2, 2.5, and 3.2 respectively, and N$_2$ = 0.14 mol h^{-1}.

[c] isobutanol =0.052 mol h^{-1}, H$_2$O =0.9 mol h^{-1}, and N$_2$ = 0.14 mol h^{-1}. Conditions: 7.3CoAl, SCMR=2.5, WHSV=7.02 h^{-1}.

[d] Reproducible results

4.2.2.1 Time-on-stream behavior of 7.3CoAl

The stability of 7.3CoAl was demonstrated for 12 h of TOS study as shown in Figure 4.10. Practically complete CCGP was observed throughout the experiment. The composition of gaseous products was however reached to steady state within about initial 100 min of TOS. After 100 min of TOS, variation of composition of gaseous products was insignificant up to 12 h of TOS as observed from the figure. Thus γ-Al$_2$O$_3$ supported cobalt catalysts can be

considered as fairly stable under the experimental conditions.
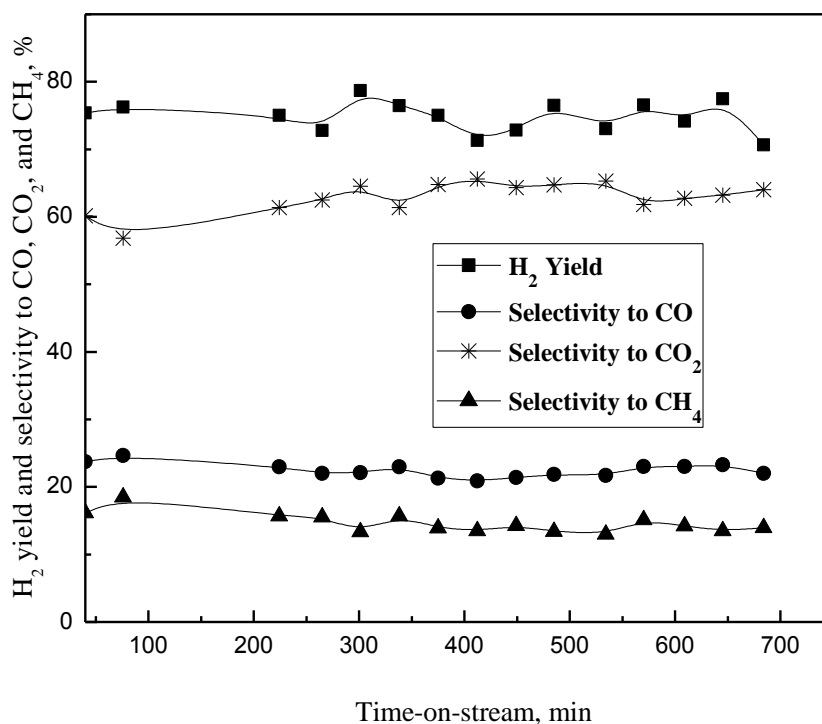
Figure 4.10: Time-on-stream behavior of 7.3CoAl catalyst. Conditions: 873 K, SCMR = 2.47, WHSV = 7.02 h^{-1}, CCGP = 100%.

4.2.2.2   Effect of cobalt loading on γ-Al$_2$O$_3$

To find optimum cobalt loading, four different catalysts were prepared with cobalt loading of 3.0, 4.3, 5.7, and 7.3 mmol per gram of γ-Al$_2$O$_3$. The effects of cobalt loading on γ-Al$_2$O$_3$ on CCGP, hydrogen yield, and selectivity to CO, CO$_2$, and CH$_4$ are shown in Figure 4.11. The CCGP increased with increasing cobalt loading on γ-Al$_2$O$_3$. About 96% CCGP was observed for 7.3CoAl. The number of active metal sites increased with increasing cobalt loading on γ-Al$_2$O$_3$ which in turn results in an increasing trend of catalytic activity. Consistent hydrogen yield (close to 80%) was obtained irrespective of cobalt loading on γ-Al$_2$O$_3$.
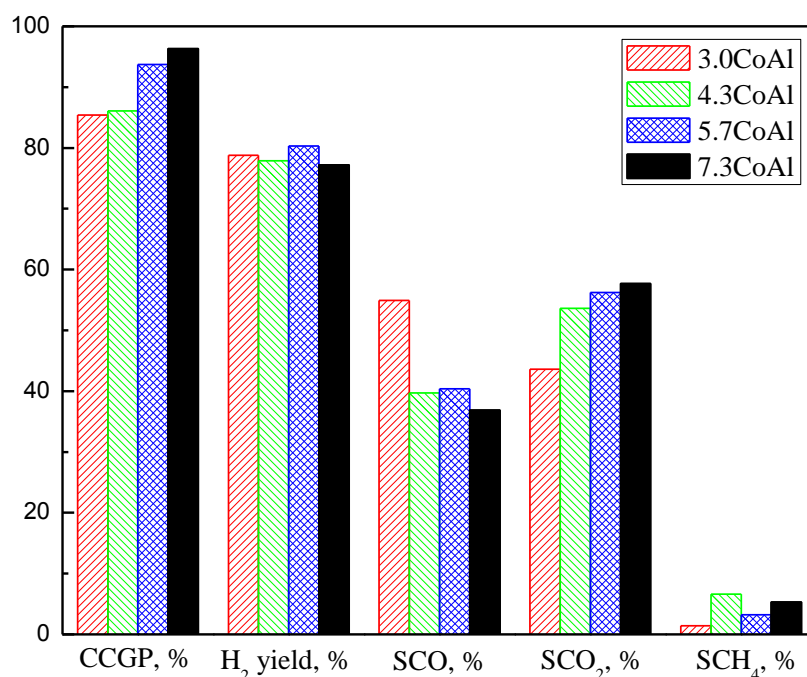
Figure 4.11: Effect of cobalt loading on γ-Al$_2$O$_3$ on CCGP, hydrogen yield, and selectivity to CO, CO$_2$, and CH$_4$. Conditions: 923 K, SCMR = 2.2, WHSV = 6.62 h^{-1}.

The selectivity to CO decreased with increasing cobalt loading on γ-Al$_2$O$_3$ and reverse trends were observed for selectivity to CO$_2$. With increasing cobalt loading on γ-Al$_2$O$_3$, WGSR favoured leading to decrease of selectivity to CO and increase of selectivity to CO$_2$ and H$_2$/CO mole ratio. The H$_2$/CO mole ratio in the range of 4.0 to 6.3 was achieved. The effects of cobalt loading on γ-Al$_2$O$_3$ on selectivity to methane was however practically insignificant. Since highest catalytic activity and H$_2$/CO mole ratio was observed for 7.3CoAl, remaining studies were performed using 7.3CoAl as catalyst.

4.2.2.3   Effect of steam-to-carbon mole ratio

The effect of SCMR was studied at 923 K in the SCMR range of 1.5-3.2 maintaining a constant WHSV of 6.5 h^{-1}. Almost complete CCGP was observed for all runs under the experimental conditions. The effect of SCMR on hydrogen yield and selectivity to CO, CO$_2$,

and CH_4 are shown in Figure 4.12. As observed from the figure, hydrogen yield and selectivity to CO_2 increased with increasing SCMR.
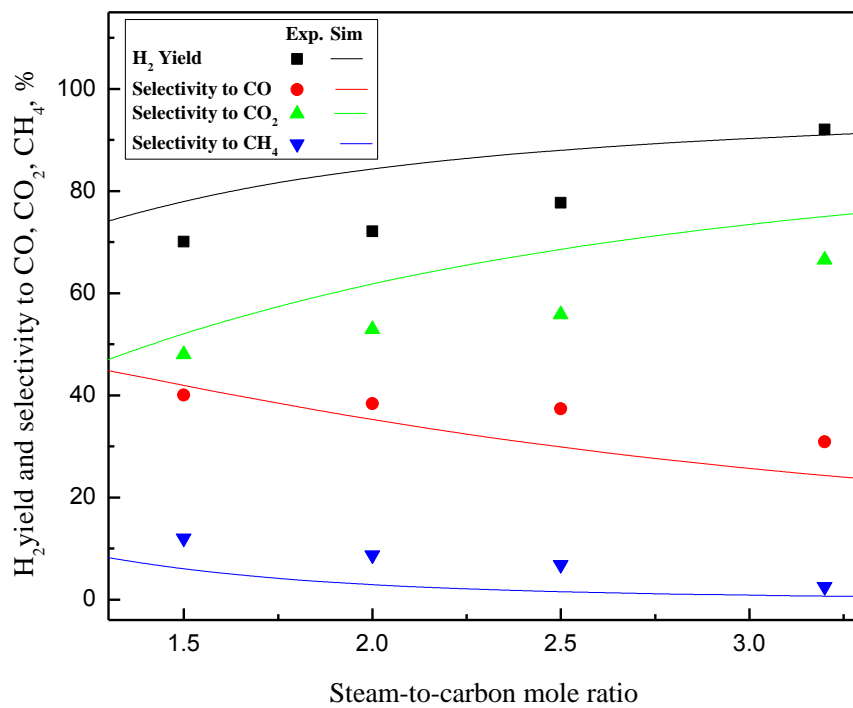
Figure 4.12: Effect of steam-to-carbon mole ratio on hydrogen yield and selectivity to CO, CO_2, and CH_4. Conditions: 7.3CoAl, 923 K, WHSV = 6.5 h^{-1}, CCGP = 100%.

The hydrogen yield increased from 70% at SCMR of 1.5 to about 90% at SCMR of 3.2. The selectivity to CO and CH_4 however decreased with increasing SCMR. Very low selectivity to methane in SG is highly desirable one for its downstream applications as feedstock for FTS and petroleum or fertilizer industry. As observed from the figure, selectivity to methane decreased from about 12% at SCMR of 1.5 to less than 3% at SCMR of 3.2. The SR of isobutanol (Eq.(i) of **Error! Reference source not found.**), intermediate compounds, and methane (reverse of Eqs.(iv-v) of **Error! Reference source not found.**) and WGSR (Eq.(ii) of **Error! Reference source not found.**) are favoured with increasing SCMR that results in an increasing trend of hydrogen yield and selectivity to CO_2 and decreasing trend of selectivity to CO and CH_4 with increasing SCMR. It can also be observed from Table 4.5 that molar flow rate of components in liquid samples decreased significantly with increasing SCMR.

The study was further extended to thermodynamic equilibrium analysis of SR of

isobutanol using R-Gibbs reactor with UNIF-LBY as property method using Aspen Plus under the identical experimental conditions. The detailed approach of thermodynamic equilibrium analysis of SR was presented in our earlier publications [82,83]. The results of thermodynamic equilibrium analysis of SR of isobutanol were then compared with experimental data as shown in Figure 4.12. The experimental trends of results displayed good agreement with that of thermodynamic equilibrium analysis results. However, the hydrogen yield and selectivity to CO_2 was somewhat lower than that of equilibrium values. The selectivity to CH_4 and CO was observed to be higher than that of equilibrium selectivity. From these results it may be concluded that reactions involved in SR of isobutanol (especially WGSR and methane SR reaction) remained slightly away from the equilibrium under the experimental conditions studied.

4.2.2.4 Effect of temperature

The effect of temperature on SR of isobutanol was studied at SCMR of 2.48 and WHSV of 7.02 h^{-1} in the temperature range of 773-923 K as shown in Figure 4.13.
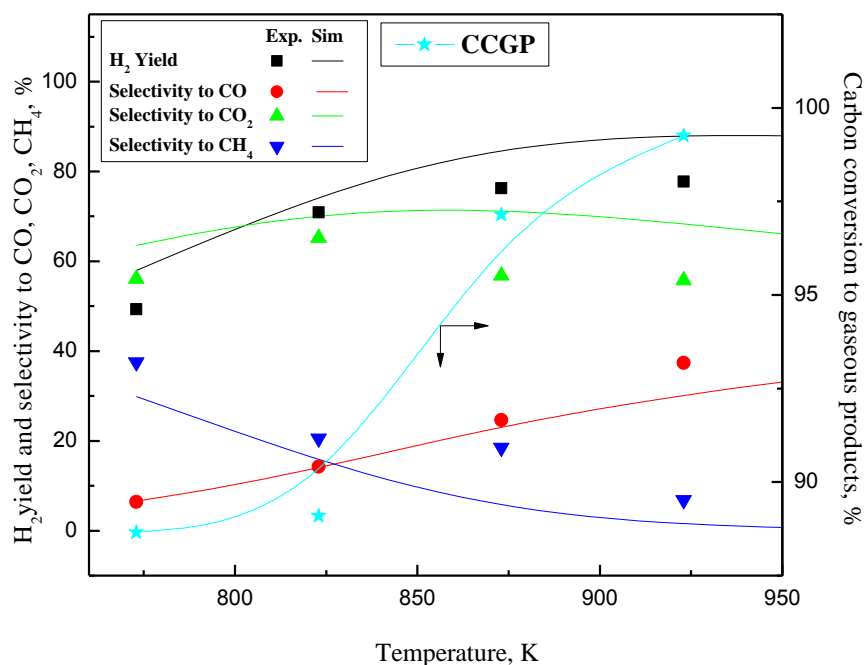
Figure 4.13: Effect of temperature on CCGP, hydrogen yield, and selectivity to CO, CO_2, and CH_4. Conditions: 7.3CoAl, SCMR = 2.48, WHSV = 7.02 h^{-1}.

As can be observed from the figure, CCGP increased with increasing temperature from merely 25% at 773 K to 100% at 923 K. The endothermic SR reactions (Eq.(i) and Eq.(iii) of Scheme 2.1) are favourable at high temperature leading to increasing CCGP with increasing temperature. The hydrogen yield increased with increasing temperature up to 873 K; beyond which hydrogen yield remained almost unchanged.

The selectivity to CO_2 and CH_4 decreased and selectivity to CO increased with increasing temperature. From these results it may be concluded that equilibrium of endothermic SR reactions (isobutanol and methane) (Eq.(i), Eq.(iii), and reverse of Eqs.(iv-v) of Scheme 2.1) are favoured at higher temperature leading to increase of hydrogen yield and decrease of selectivity to CH_4 with temperature. On the other hand, exothermic WGSR (Eq.(ii) of Scheme 2.1) are favoured at lower temperature that result in an increasing trend of selectivity to CO and decreasing trend of selectivity to CO_2 with temperature. Furthermore, the thermodynamic equilibrium analysis of SR of isobutanol was performed at different temperature under the experimental conditions and the results were then compared with experimental data as shown in Figure 4.13. As can be seen from the figure, the trends of experimental results are in good agreement with equilibrium results. However, the reactions involved in SR of isobutanol are away from the equilibrium to some extent causing somewhat lower hydrogen yield and selectivity to CO_2 and higher selectivity to CO and CH_4 compared to equilibrium.

Chapter 5

Oxidative Steam Reforming of Isobutanol over Ni/γ-Al$_2$O$_3$ Catalysts

SG with low levels of methane is highly desirable for applications as feedstock for chemical process industries and Fischer-Tropsch synthesis for manufacture of hydrocarbon fuels and organic chemicals. The OSR using sub-stoichiometric levels of oxygen is an attractive method for production of SG with low level of methane. Moreover, exothermic PO reaction provides necessary heat energy for endothermic SR reactions making operation of OSR under thermoneutral conditions. Detailed experimental studies on OSR of isobutanol are however very limited in the open literature. Considering the importance, the present work was extended to provide a systematic investigation of OSR and comparison with SR of isobutanol over γ-Al$_2$O$_3$ supported nickel catalysts. The experimental results were furthermore authenticated with equilibrium product compositions. The spent catalysts were additionally characterized by powder XRD and FESEM to elucidate chemical and morphological changes of catalysts during SR and OSR.

5.1   Catalyst characterization

5.1.1   Surface area, pore volume and chemisorption

The physicochemical properties of the catalysts are presented in Table 5.1. Pure γ-Al$_2$O$_3$ (calcined at 923 K) has SA and PV of 228 m^2/g and 0.84 cm^3/g respectively. The SA and PV of γ-Al$_2$O$_3$ supported calcined (4.3NiOAl and 7.3NiOAl) and reduced (4.3NiAl and 7.3NiAl) nickel catalysts were significantly lesser than pure γ-Al$_2$O$_3$ due to coverage of γ-Al$_2$O$_3$ surface by nickel/nickel oxide crystallites or blockage of pore mouths.

Table 5.1: Physicochemical properties of the catalysts.

catalysts	SA	PV	MD	SM	d_c	T_{max}, K	H_2 consumed ($\mu mol/g$)
γ-Al_2O_3	228	0.84	-	-	-	-	
4.3NiOAl	178	0.6	-	-	12.8[*]	745, 988	3167.4
7.3NiOAl	137	0.47	-	-	18.8[*]	782,1000	3243.9
4.3NiAl [a]	166	0.6	1.86	12.4	11.8[**]	-	
7.3NiAl [b]	109	0.43	1.73	11.5	18.6[**]	-	

SA = BET surface area, m^2/g; PV = pore volume, cm^3/g; MD = metal dispersion, %; SM = metallic surface area, m^2/g metal; d_c = metal[**]/metal oxide[*] crystallite size, nm. [a] For spent catalysts: nickel crystallite sizes were 15.3, 14.2, and 8.2 nm and nickel oxide crystallite sizes were 7.3, 8.4, 8.1, and 8.7 nm for OCMR of 0, 0.8, 1.7, and 2.5 respectively. Experimental conditions: 873 K, SCMR=2.5, WHSV=7.02-8.9 h^{-1}. [b] For spent catalysts: nickel crystallite sizes were 22.6 and 22.1 nm and nickel oxide crystallite sizes were 6.9 and 7.8 nm for OCMR of 0 and 0.8 respectively. Experimental conditions: 923 K, SCMR=2.5, WHSV=7.6 h^{-1}.

5.1.2 Powder XRD

The powder XRD patterns of both calcined and reduced catalysts are shown in Figure 5.1. The powder XRD patterns of calcined γ-Al_2O_3 and bulk nickel oxide were also acquired for clear discrimination of nickel peaks from support and nickel oxide peaks. The bulk nickel oxide peaks were appeared at 2θ of 37.3° (1 1 1) and 43.2° (2 0 0) for calcined catalysts (PDF#750197). The peaks observed at 2θ of 37.3° (3 1 1) and 66.2° (4 4 0) were attributed to differently coordinated dispersed nickel-aluminate ($NiAl_2O_4$) (PDF#780552). The powder XRD patterns of 4.3NiAl showed only characteristic nickel peaks indicating that nickel oxides of 4.3NiOAl were completely converted to metallic nickel during reduction at 923 K. The powder XRD patterns of 7.3NiAl however exhibited additional $NiAl_2O_4$ peaks due to incomplete reduction of $NiAl_2O_4$. The characteristic nickel peaks were identified at 2θ of 44.44° (1 1 1), 51.5° (2 0 0), and 76.4° (2 2 0) for both 4.3NiAl and 7.3NiAl (PDF#650380). As observed from Table 5.1, nickel/nickel oxide crystallites were enlarged with increasing nickel loading on γ-Al_2O_3 due to agglomeration of nickel/nickel oxide at higher nickel loadings on γ-Al_2O_3. The agglomeration of nickel/nickel oxide also caused decrease of MD and SM with increasing nickel loadings on γ-Al_2O_3 (Table 5.1). MD of 1.86% and 1.73% was

(65)

obtained for 4.3NiAl and 7.3NiAl respectively.
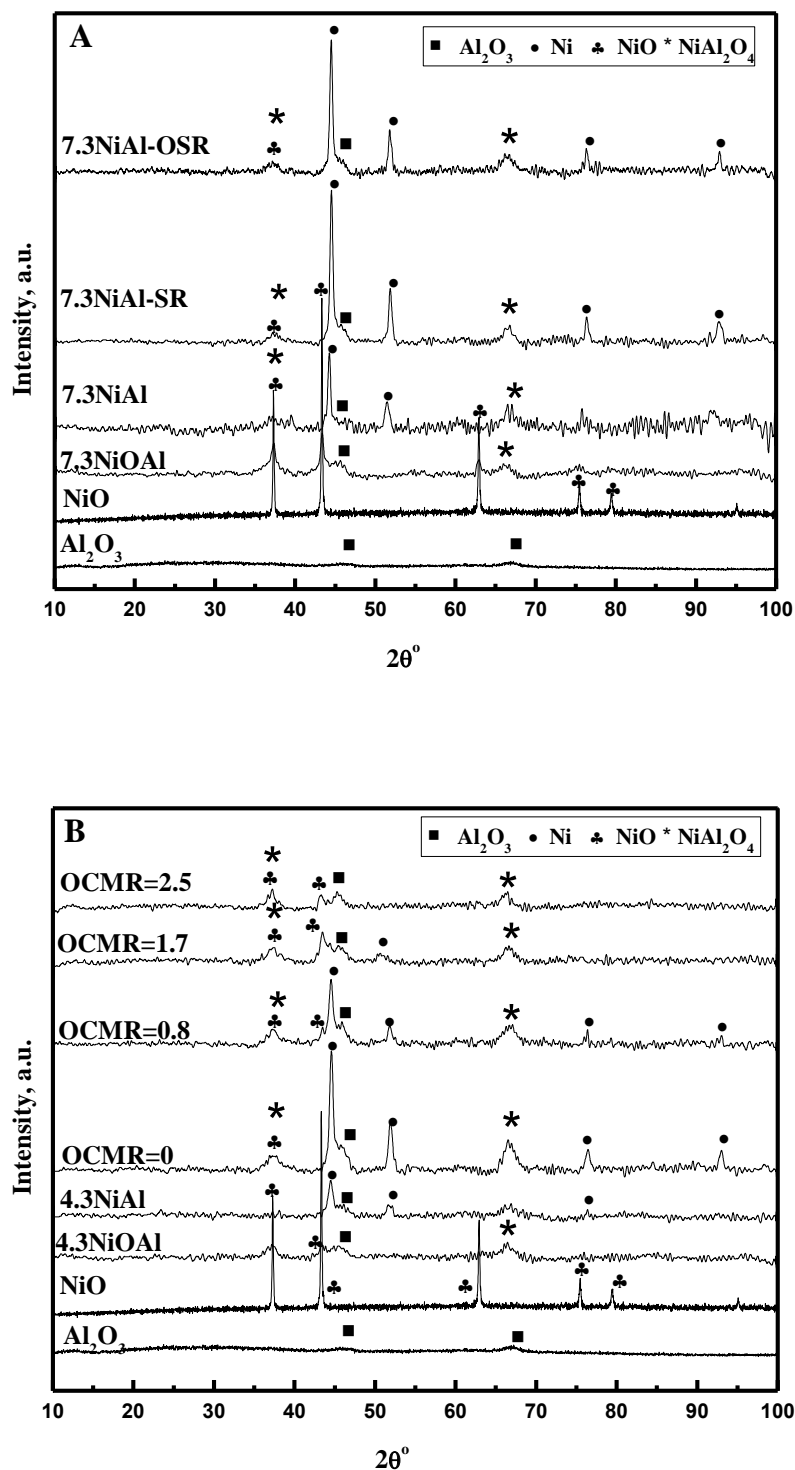
Figure 5.1: Powder XRD patterns of A. $\gamma\text{-}Al_2O_3$, NiO, 7.3NiOAl, 7.3NiAl, and spent 7.3NiAl and B. $\gamma\text{-}Al_2O_3$, NiO, 4.3NiOAl, 4.3NiAl, and spent 4.3NiAl catalysts. Experimental conditions: 923 K, SCMR=2.5, WHSV=7.02 h^{-1} (SR) and 7.6 h^{-1}(OSR), OCMR=0.8 (7.3NiAl).

5.1.3 Temperature programmed reduction

TPR profile of 4.3NiOAl and 7.3NiOAl are shown in Figure 5.2. TPR profile of calcined γ-Al_2O_3 was also evaluated to verify reducibility of γ-Al_2O_3. However, no reduction peaks were observed thereby confirming that γ-Al_2O_3 is fairly stable and absolutely non-reducible over whole ranges of temperature studied. Two clearly distinguished reduction peaks were however observed for calcined catalysts. The lower temperature broad reduction peaks were observed at 745 K and 782 K for 4.3NiOAl and 7.3NiOAl respectively.
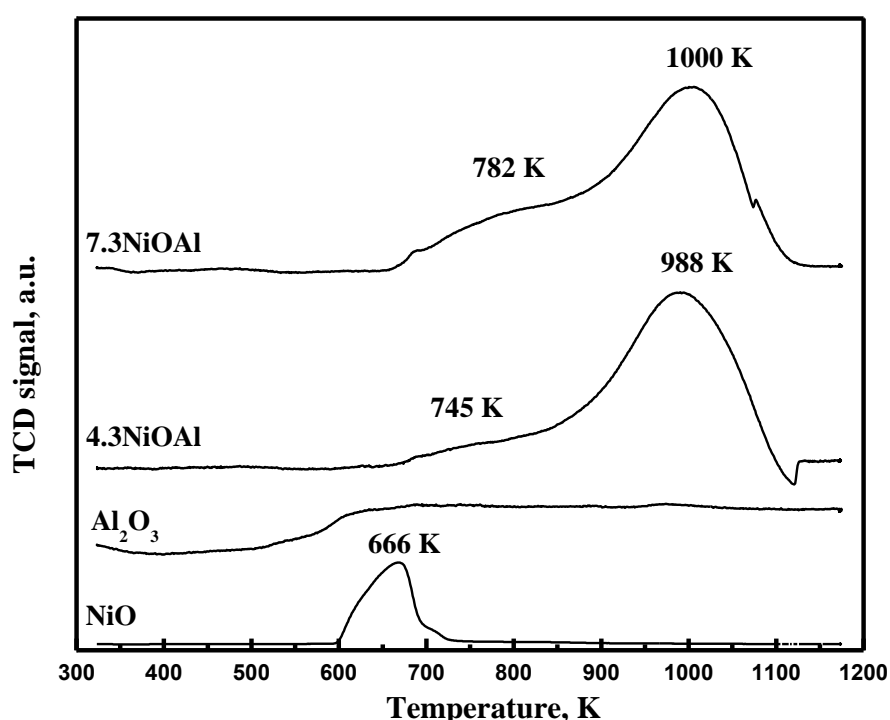
Figure 5.2: TPR profiles of NiO, γ-Al_2O_3, 4.3NiOAl, and 7.3NiOAl.

To ascertain these reduction peaks, TPR profile of bulk nickel oxide was also acquired. The results clearly showed that these peaks were attributed to the reduction of bulk nickel oxide. However, these peaks were comparatively broader relative to bulk nickel oxide peaks and shifted gradually to higher temperature with increasing nickel loadings on γ-Al_2O_3. These results undoubtedly suggested existence of weak interaction of bulk nickel oxide with γ-Al_2O_3. The shifting of reduction peak to higher temperature for higher nickel loadings on γ-Al_2O_3 may also be due to higher quantities of enlarged bulk nickel oxide crystallites. Powder

XRD patterns also confirmed enlargement of nickel/nickel oxide crystallites with increasing nickel loading on γ-Al_2O_3. Higher temperature reduction peaks were observed at 988 K and 1000 K for 4.3NiOAl and 7.3NiOAl respectively. These peaks were due to reducible dispersed $NiAl_2O_4$ spinel [101]. Powder XRD patterns also manifested $NiAl_2O_4$ peaks in 4.3NiOAl, 7.3NiOAl, and 7.3NiAl. In $NiAl_2O_4$ spinel, Ni^{2+} ions were incorporated non-stoichiometrically in tetrahedral (Ni_{td}) or octahedral (Ni_{oct}) sites of γ-Al_2O_3. The dispersed Ni_{td} reduced at relatively lower temperature than dispersed Ni_{oct} [101]. The increase of nickel loading on γ-Al_2O_3 enriched reducible Ni_{oct} species leading to rise of reduction temperature [101]. The relative peaks area and intensity further suggests that majority of nickel oxide exists as dispersed $NiAl_2O_4$ form on γ-Al_2O_3.

5.2   Results and discussion

Investigation of SR and OSR of isobutanol were carried out over γ-Al_2O_3 supported nickel catalysts under wide range of OCMRs (0.8-2.5), temperature (773-923 K), and SCMRs (1.5-3.2). The acetaldehyde, propionaldehyde, isobutyraldehyde, 2-propenal, 2-butanone, 1-butanol, 2-butanol, and unreacted isobutanol were identified as products in liquid samples. The carbon balance was checked for all experiments and errors were within ±10% (Table 5.2). As observed from the table, unreacted butanols were major products in liquid sample in all experiments. It was further observed that molar flow rates of products in liquid samples decreased with increasing OCMR, temperature, and SCMR. However, these products were excluded from selectivity calculations for better comparisons with equilibrium selectivity to CO, CO_2, and methane. The reproducibility of the experiments was also checked for few runs as shown in Table 5.2. The molar flow rates of various products matched closely for repeated runs thereby confirming that experimental data are reasonably reproducible. Moreover, the activity of pure γ-Al_2O_3 was also examined for SR and OSR and negligible CCGP was observed under the experimental conditions thereby demonstrating that γ-Al_2O_3 alone has insignificant role for SR and OSR.

Table 5.2: Carbon balance table for SR and OSR of isobutanol.

	gas products flow rates, mol h^{-1}				liquid products flow rates$\times 10^5$, mol h^{-1}						CBE	CIB	H_2/Bu
	H_2	CO	CH_4	CO_2	ACE	PPD	PPL	BUD	BUN	BU			
OCMR				**Effect of OCMR for OSR**[a]									
0	0.406	0.052	0.025	0.107	1.3	2.67	2	0.32	3.1	90.5	9.6	98.2	7.9
0.8	0.363	0.043	0.005	0.137	2.83	50.7	27.6	0.14	32.3	70.4	7.9	98.6	7.07
1.7	0.318	0.040	0.003	0.147	2.06	34.7	16	0	17.9	8.5	7.4	99.8	6.1
2.5	0.183	0.023	0.001	0.179	2.3	26.42	6.65	0	11.92	2.96	1.6	99.9	3.5
Temperature, K				**Effect of temperature for SR**[b]									
773	0.277	0.027	0.04	0.117	2.81	3.04	3	0	4.26	78.3	9.8	98.4	5.4
823	0.311	0.036	0.033	0.13	0.65	2.02	0	0	2.31	38.1	3.5	99.2	6.02
873	0.455	0.044	0.03	0.133	0.278	0.56	0	0	0.79	0.22	0.45	99.9	8.7
923	0.499	0.060	0.011	0.137	0	0.12	0	0.164	0.178	0.179	-0.01	99.9	9.5
Temperature, K				**Effect of temperature for OSR**[c]									
773	0.236	0.019	0.027	0.136	1.67	63.5	25.7	0	28	65	9.4	98.7	4.5
823	0.308	0.026	0.022	0.138	0.57	16.07	7.1	0	6.5	46	9.2	99.1	5.9
873[R1]	0.394	0.043	0.012	0.146	0.16	2.5	0.63	0	1.5	1.3	3.2	99.9	7.5
873[R1]	0.376	0.04	0.017	0.140	0.4	10.62	2.62	0	1.9	37.2	4.3	99.2	7.2
923[R2]	0.42	0.06	0.004	0.142	0.025	0.52	0.15	0	0.38	0.7	1.4	99.9	8.07
923[R2]	0.45	0.06	0.004	0.142	0.789	1.3	0.50	0	0.27	2.5	1.1	99.9	8.6
SCMR				**Effect of SCMR for SR**[d]									
1.5	0.593	0.140	0.035	0.104	0.072	1.3	1	0	1.51	3.211	1.67	99.95	8.3
2	0.504	0.081	0.02	0.115	0.048	1.63	0	0.046	0.303	3.52	6.8	99.93	8.6
2.5	0.499	0.060	0.011	0.137	0	0.12	0	0.164	0.178	0.179	-0.01	99.99	9.5
3.2	0.424	0.049	0.004	0.103	0.06	0.02	0	0	0	0.07	-2.63	99.99	11.1
SCMR				**Effect of SCMR for OSR**[e]									
1.5	0.493	0.098	0.018	0.155	3.3	2.17	50.13	0	0.69	5.95	4	99.91	6.9
2	0.439	0.077	0.01	0.146	2.06	6.05	57.87	0	0.87	27.81	-1.7	99.5	7.6
2.5	0.448	0.059	0.005	0.142	0.79	1.31	0.501	0	0.27	2.54	0.9	99.95	8.6
3.2	0.32	0.033	0.001	0.121	0.22	0.069	122.8	0	0.35	0.36	-4.4	99.99	8.4

ACE = acetaldehyde, PPD = propionaldehyde, PPL=2-propenal, BUD = butyraldehyde, BUN = 2-butanone, BU = 1-, 2-, and butanol; CBE = carbon balance error, %, CIB= conversion of Isobutanol, %.

[a] isobutanol =0.052 mol h^{-1}, H_2O =0.9 mol h^{-1}, and N_2=0.14 mol h^{-1}. Experimental conditions: 4.3NiAl, 873 K, SCMR= WHSV= 7.02, 7.6, 8.3 and 8.9 h^{-1} for OCMR of 0.8, 1.7 and 2.5 respectively.

[b] isobutanol =0.052 mol h^{-1}, H_2O = 0.9 mol h^{-1}, and N_2=0.14 mol h^{-1}. Experimental conditions: 7.3NiAl, SCMR=2.5, WHS 7.02 h^{-1}.

[c] isobutanol =0.052 mol h^{-1}, H_2O = 0.9 mol h^{-1}, and N_2=0.14 mol h^{-1}. Experimental conditions: 7.3NiAl, SCMR=2.5, OCMR= WHSV= 7.6 h^{-1}.

[d] isobutanol = 0.071, 0.058, 0.052, and 0.038 mol h^{-1} and H_2O = 0.73, 0.8, 0.9, and 0.87 mol h^{-1} for SCMR of 1.5, 2, 2.5, and respectively, and N_2=0.14 mol h^{-1}. Experimental conditions: 7.3NiAl, 923 K, WHSV= 6.5 h^{-1}.

[e] isobutanol =0.071, 0.058, 0.052, and 0.038 mol h^{-1} and H_2O = 0.73, 0.8, 0.9, and 0.87 mol h^{-1} for SCMR of 1.5, 2, 2.5, and respectively, and N_2=0.14 mol h^{-1}. Experimental conditions: 7.3NiAl, 923 K, OCMR =0.8, WHSV= 7.6 h^{-1}. [R1, R2] Reproducibi results.

5.2.1 Time-on-stream behavior of 7.3NiAl for OSR

The catalyst stability of 7.3NiAl for OSR was verified for about 12 h of TOS (Figure 5.3). 100% CCGP persisted over the entire range of TOS. The product gas composition reached to steady state within first 2 h of TOS. After initial 2 h of TOS, the hydrogen yield and selectivity to CO, CO_2, and methane remained practically constant up to 12 h of TOS. These results confirmed that γ-Al_2O_3 supported nickel catalysts were fairly stable under the experimental conditions. All subsequent experiments were conducted for minimum of 4 h of TOS. The products composition data were collected after 2 h of TOS for all experiments.
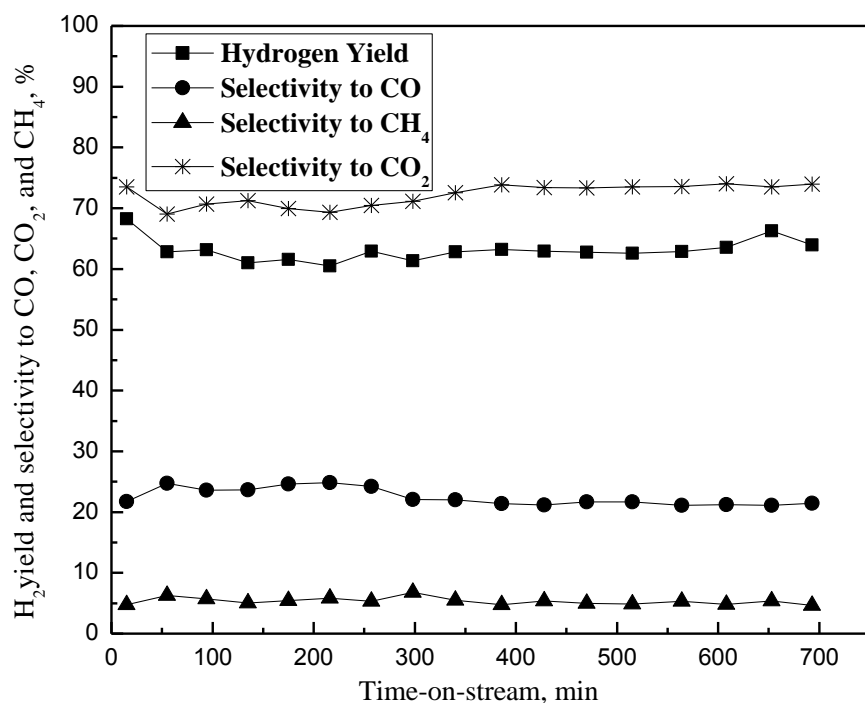
Figure 5.3: Time-on-stream behaviour of 7.3NiAl catalyst for OSR. Experimental conditions: 873 K, SCMR = 2.5, WHSV = 7.6 h^{-1}, OCMR=0.8, CCGP = 100%.

5.2.2 Effect of oxygen-to-carbon mole ratio

The effect of OCMR was investigated experimentally at 873 K with SCMR of 2.5 (Figure 5.4). The experiments were performed at various oxygen flow rates in the feed equivalent to OCMR in the range of 0-2.5 keeping all other process parameters constant. The experiments were designed well below OCMR of 4 to avoid complete combustion of isobutanol to CO_2

(70)

and H_2O. The introduction of oxygen in the feed however resulted in slightly increasing trend of WHSV with increasing OCMR. In the product gas, even traces of oxygen was not detected in any of the experiments thereby confirming that oxygen completely reacted with isobutanol, intermediate compounds, or products within the reactor.
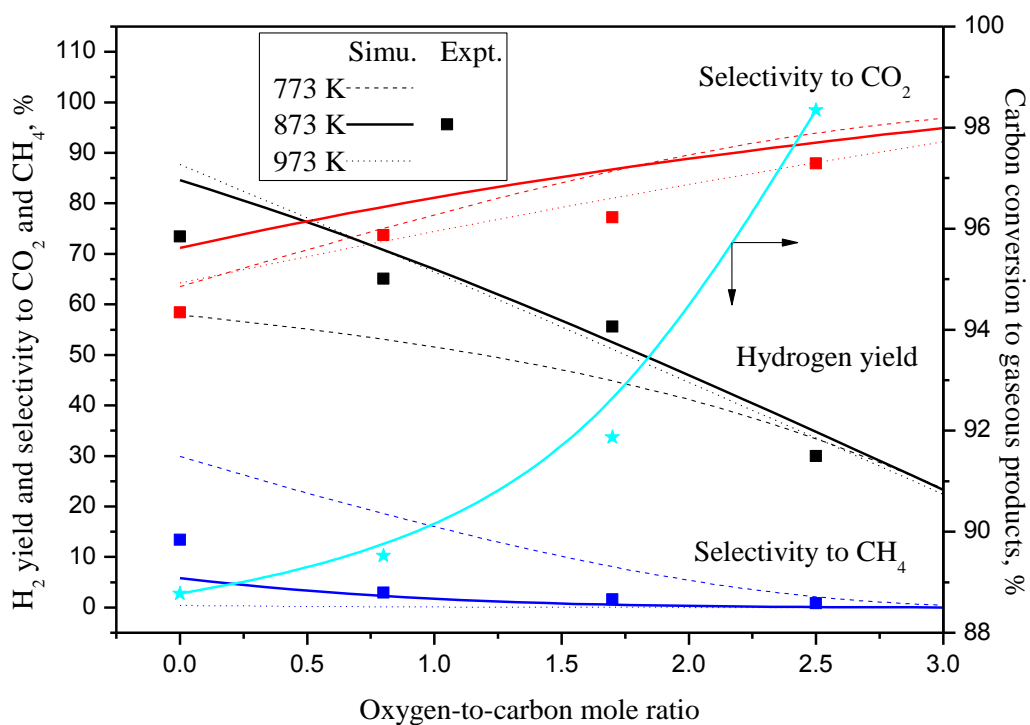

Figure 5.4: Effect of oxygen-to-carbon mole ratio on hydrogen yield, and selectivity to CO_2 and CH_4 for OSR. Experimental conditions: 4.3NiAl, 873 K, SCMR=2.5, WHSV= 7.02, 7.6, 8.3 and 8.9 h^{-1} for OCMR of 0, 0.8, 1.7, and 2.5 respectively.

The CCGP increased from ~89% to ~98% with increasing OCMR from 0 to 2.5. The increase of CCGP was mainly due to enhanced oxidation of isobutanol or intermediate compounds with increasing OCMR. The hydrogen yield and selectivity to CO and CH_4 however reduced and selectivity to CO_2 increased continually with increasing OCMR. The hydrogen yield reduced to just 30% from 73%; while selectivity to CH_4 dropped to only 0.3% from 13.5% with increase of OCMR from 0 to 2.5. These results suggested that oxidation of hydrogen, CO, and CH_4 into H_2O and CO_2 was promoted with increasing levels of oxygen in the feed thereby decreasing hydrogen yield and selectivity to CO and CH_4. Identical trends were also reported earlier for OSR of ethanol [100] and isobutanol [77].

(71)

The equilibrium product compositions were also calculated under identical experimental conditions at three different temperature and compared with experimental hydrogen yield and selectivity to CO_2 and CH_4 as presented in Figure 5.4. As observed from the figure, experimental trends of hydrogen yield and selectivity to CO_2 and CH_4 were fully consistent with thermodynamic equilibrium analysis results.

5.2.3 Thermoneutral conditions

The principal advantage of OSR is that heat required for endothermic SR reactions can be generated in-situ by exothermic PO reactions. Therefore, maintaining appropriate OCMR depending on process conditions is crucial to accomplish thermoneutral operation (condition at which heat duty =0). The heat duty of the process is governed mainly by the feed and reactor temperature and OCMR. In the present study, heat duty analyses were performed by varying reactor temperature for several OCMRs (0.5-1.0) assuming feed (consisting of isobutanol, water, and oxygen) and reactor temperature being same (Figure 5.5A). As observed from the figure, exothermicity of the process increased with increasing OCMR for a fixed temperature. However, for fixed OCMR, process become increasingly endothermic with increasing temperature. As noted from the figure, OCMR of 0.5, 0.6, and 0.7 are necessary for thermoneutral operation at 808 K, 854 K, and 1057 K, respectively.
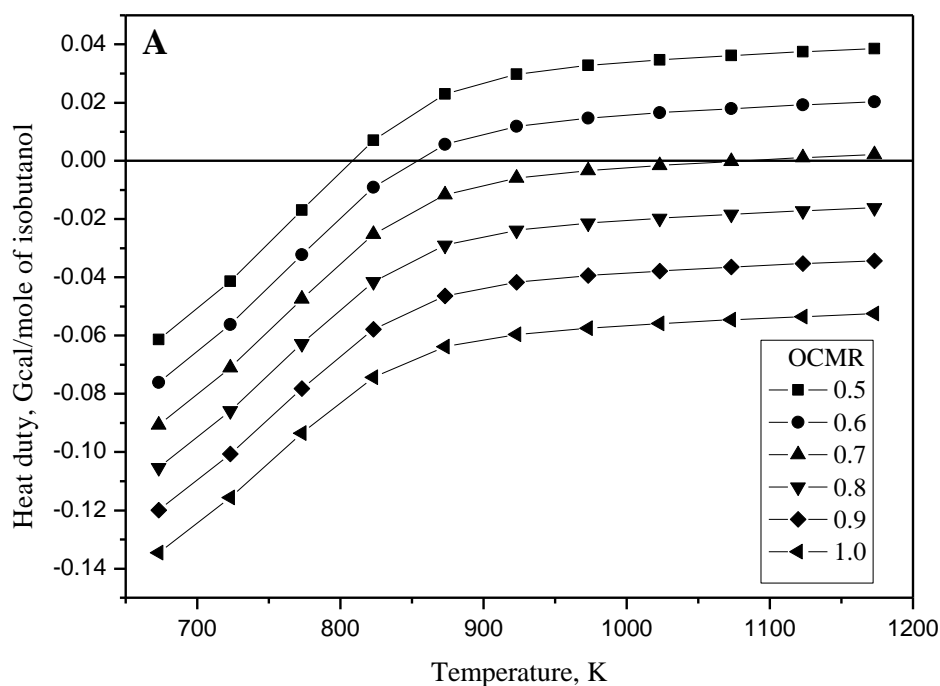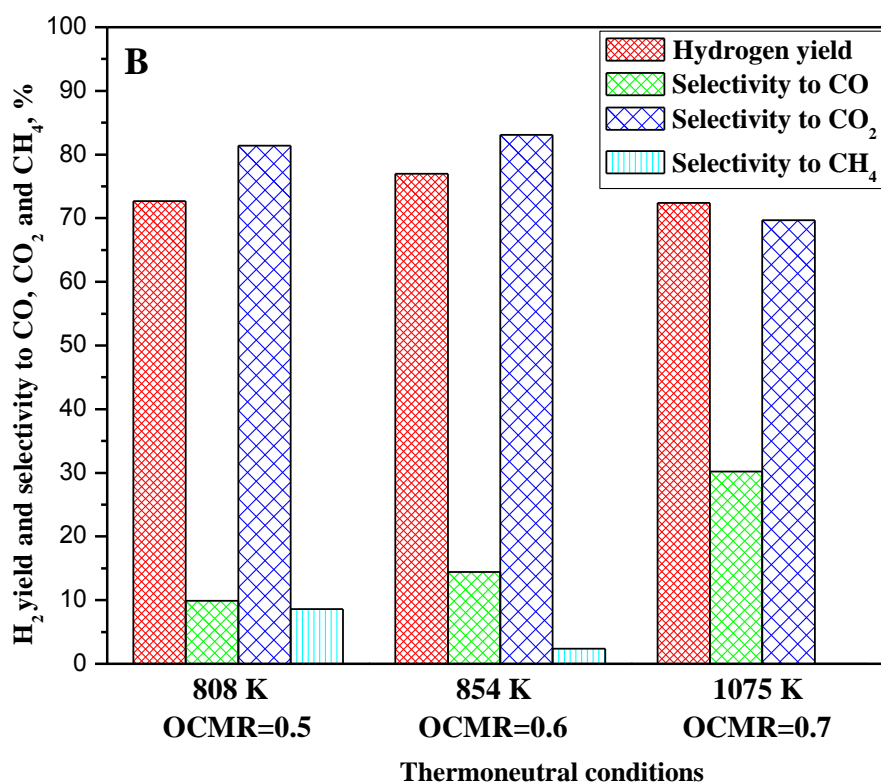
Figure 5.5: A. Heat duty analysis and B. equilibrium product composition at thermoneutral conditions for OSR of isobutanol.

The equilibrium SG composition at thermoneutral conditions is shown in Figure 5.5B. As observed from the figure, selectivity to methane decreased with increasing temperature and it was almost negligible at 1075 K with OCMR=0.7. The selectivity of CO increased with increasing temperature.

5.2.4   Effect of temperature

The experimental investigations of SR of isobutanol were conducted in the temperature range of 773-923 K with SCMR of 2.5 and WHSV of 7.02 h^{-1} as shown in Figure 5.6A.   As observed from the figure, CCGP increased with increasing temperature. The CCGP was just ~89% at 773 K and reached to 100% at 923 K. The increase of CCGP was mainly due to enhancements of endothermic SR reactions (Eq.(i) and reverse of Eqs.(iv-v) of **Error! Reference**

source not found.) at elevated temperature. The equilibrium calculations were however performed in the temperature range of 623-1173 K at three different SCMRs, 1.5, 2.5, and 3.5. The equilibrium results were then compared with experimental hydrogen yield and selectivity to CO and CH$_4$ (Figure 5.6A). As observed from the figure, equilibrium results were fully consistent with experimental data.

For fixed SCMR, equilibrium hydrogen yield increased sharply with increasing temperature and reached a maximum at about 903-969 K depending on SCMR. The hydrogen yield was then started declining slowly with further increase in temperature. The maximum experimental hydrogen yield of ~80% was observed at 923 K and SCMR of 2.5 compared to theoretical maximum of ~87%. The slightly lesser experimental hydrogen yield clearly indicates that reactions are somewhat away from the equilibrium.
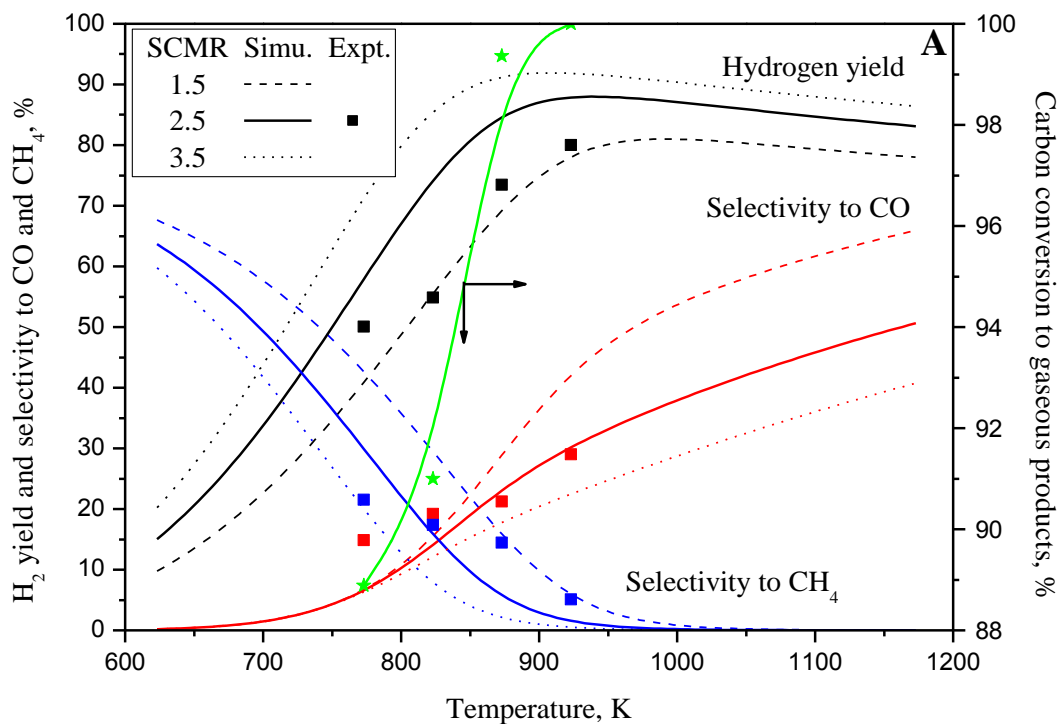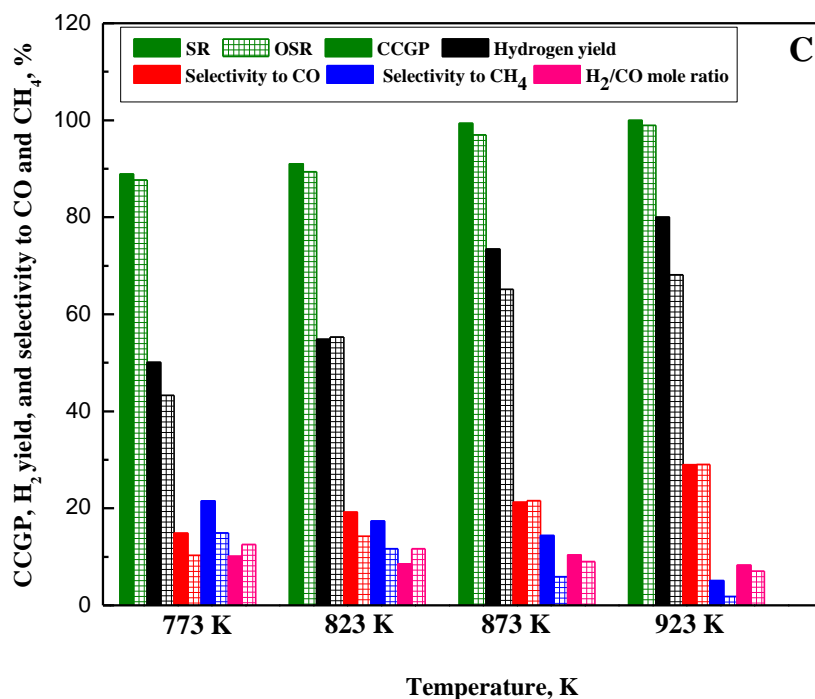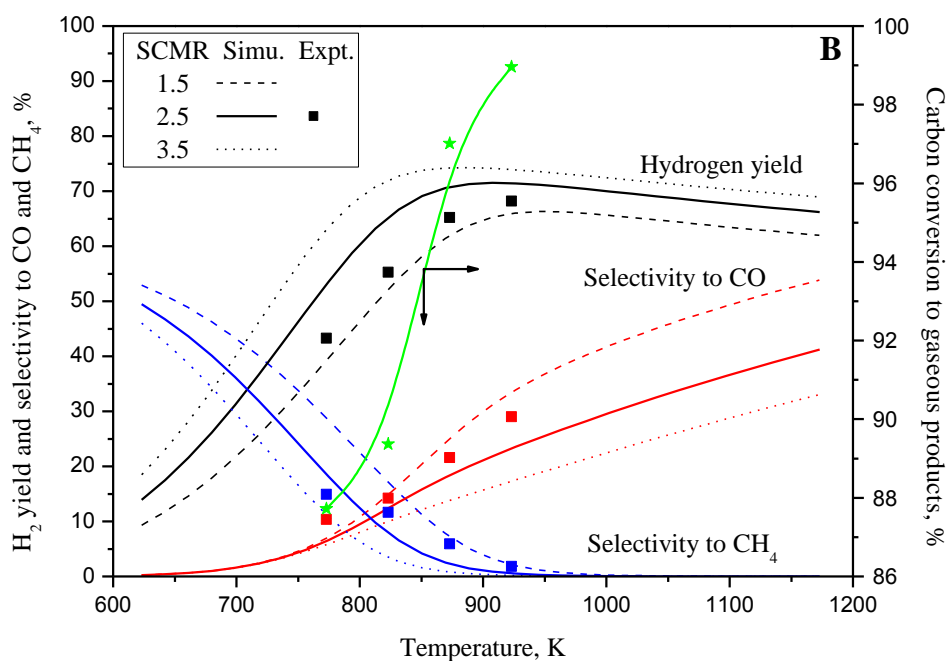
Figure 5.6: Effect of temperature on CCGP, hydrogen yield, and selectivity to CO and CH₄ for A. SR, B. OSR, and C. comparison of SR and OSR of isobutanol. Experimental conditions: 7.3NiAl, SCMR=2.5, WHSV=7.02 h⁻¹ (SR) and 7.6 h⁻¹ (OSR), OCMR=0.8 (OSR).

On the other hand, selectivity to CO increased and selectivity to CH$_4$ dropped with increasing temperature. The experimental selectivity to CH$_4$ was reduced to only 5% at 923 K with SCMR of 2.5. These observations can be explained by the fact that endothermic SR reactions (Eq.(i) and reverse of Eqs.(iv-v) of **Error! Reference source not found.**) are favoured at elevated temperature; while exothermic WGSR (Eq.(ii) of **Error! Reference source not found.**) are favoured at lower temperature. At relatively lower temperature (below temperature of maximum of hydrogen yield) with high concentration of methane, contribution of endothermic SR reactions on hydrogen yield were dominating over exothermic WGSR leading to growing trends of hydrogen yield with increasing temperature. However, at sufficiently high temperature with very low concentration of methane, SR of methane became unimportant and exothermic WGSR became sole contributing factor on hydrogen yield leading to slightly declining trends of hydrogen yield with increasing temperature. It was further observed from the figure that temperature of maximum hydrogen yield moved gradually to lower temperature with increasing SCMR. This was due to the fact that selectivity to methane reached a low value at a relatively lower temperature at higher SCMR.

The effect of temperature on OSR of isobutanol was investigated at OCMR of 0.8 under otherwise identical experimental conditions of SR. The thermodynamic equilibrium analysis of OSR of isobutanol was carried out at SCMRs of 1.5, 2.5, and 3.5. The equilibrium results were then compared with experimental data as shown in Figure 5.6B. Fairly decent agreements were also observed between equilibrium and experimental hydrogen yield and selectivity to CO and CH$_4$. As observed from the figure, the trends of OSR results were fully analogous to SR. Hence, similar arguments can be used to explain the trend of OSR results as well.

The comparisons of experimental OSR results with SR are presented in Figure 5.6C. As shown in figure, CCGP was somewhat lesser for OSR compared to SR. The molar flow rates of products in liquid samples were also slightly higher in OSR than SR (Table 5.2). The lesser CCGP and higher levels of products in liquid samples in OSR were mainly due to slightly higher WHSV compared to SR (owing to added oxygen flow in feed for OSR). The hydrogen yield and selectivity to CO and CH$_4$ were however lesser for OSR compared to SR. Experimental hydrogen yield was only ~68% for OSR compared to ~80% for SR at 923 K. The selectivity to CH$_4$ dropped to below 2% for OSR from ~5% for SR at 923 K. Such a low selectivity to methane is one of the biggest advantages of OSR. These results clearly indicated that hydrogen, CO, and methane were oxidised by oxygen leading to drop in

hydrogen yield and selectivity to CO and methane for OSR compared to SR [102,103]. Thermodynamic equilibrium analysis results further revealed that temperature corresponding to maximum hydrogen yield were somewhat lesser for OSR (864-932 K) compared to SR (903-969 K). This was mainly due to lesser selectivity to methane OSR compared to SR for a fixed temperature and SCMR.

The requirements of H_2/CO mole ratio generally varies depending upon downstream applications of SG. For example, H_2/CO mole ratio in the range of 1.7 to 2.15 is required for FTS of methanol, dimethyl ether, and hydrocarbons. The hydrogen rich SG however provides the source of hydrogen for chemical process industries or fuel cell. As seen from Figure 5.6C, H_2/CO mole ratio remained practically unaffected by temperature for both SR and OSR. With increasing temperature, both hydrogen yield and selectivity to CO increased thereby keeping H_2/CO mole ratios almost unchanged. It was further observed from the figure, H_2/CO mole ratios were virtually same for both SR and OSR. These results clearly demonstrated that hydrogen and CO were equally oxidised in presence of oxygen thereby maintaining consistent H_2/CO mole ratios for both SR and OSR. In the present study, H_2/CO mole ratios in the range of 8-10 were observed for both SR and OSR under the experimental conditions.
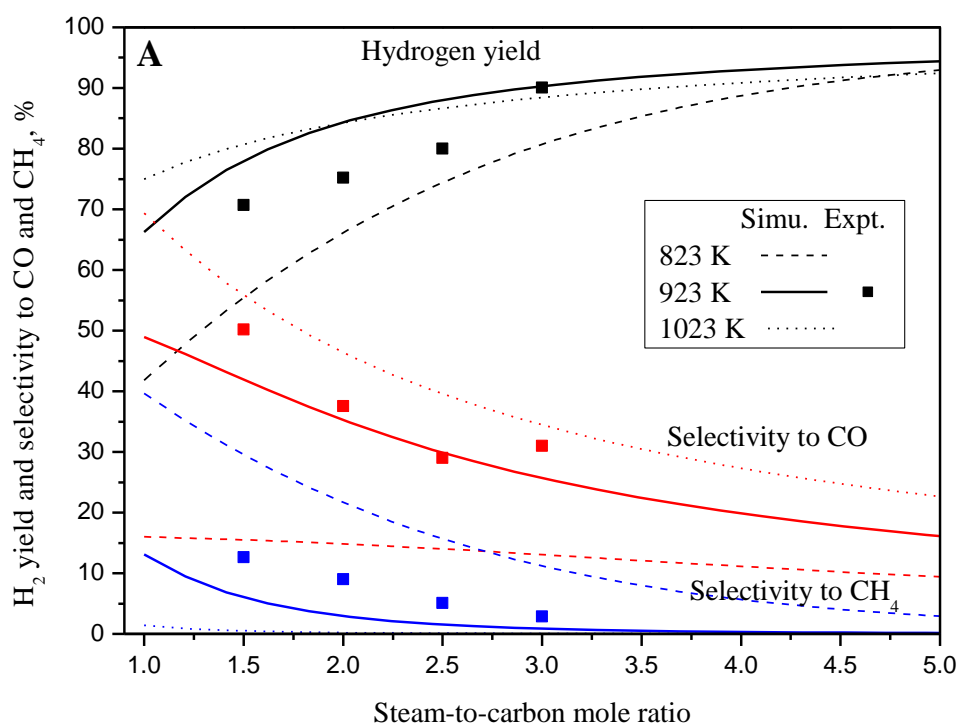
5.2.5 Effect of steam-to-carbon mole ratio

The SR experiments were conducted over 7.3NiAl at 923 K and 6.5 h^{-1} WHSV in the SCMR range of 1.5 to 3.2 as illustrated in Figure 5.7. For accurate comparisons of results, WHSV for all experiments was kept constant by maintaining same total mass flow rate of feed (with different mole ratios of isobutanol and water) and weights of the catalyst (Table 5.2). Almost complete CCGP was observed for whole ranges of SCMRs studied. Thermodynamic equilibrium analysis was performed at three different temperature (823, 923, and 1023 K) under otherwise identical experimental conditions. The equilibrium results agreed reasonably well with experimental hydrogen yield and selectivity to CO and CH_4 as shown in the figure.

The hydrogen yield increased with increasing SCMR for a fixed temperature. The selectivity to CO and CH_4 however decreased with increasing SCMR. The maximum of 90% hydrogen yield with less than 3% selectivity to CH_4 was observed experimentally at SCMR of 3.2. With increase of SCMR, SR of isobutanol, SR of methane (reverse of Eqs.(iv-v) of **Error! Reference source not found.**) and WGSR (Eq.(ii) of **Error! Reference source not found.**) were favoured thereby increasing hydrogen yield and decreasing selectivity to CO and CH_4. Similar trends of experimental and equilibrium results were also reported earlier for SR of

(77)

aqueous phase of bio-oil [104].

Effect of SCMR on OSR of isobutanol was also examined at OCMR of 0.8 and WHSV of 7.6 h^{-1} under otherwise identical experimental condition of SR as shown in Figure 5.7B. As shown in the figure, CCGP increased with increasing OCMR. The CCGP was about 95% at SCMR of 1.5 and touched 100% at SCMR of 3.2. The equilibrium calculations for OSR of isobutanol were also carried out at three different temperature, 823, 923, and 1023 K. The experimental OSR results matched reasonably well with equilibrium predictions. Moreover, identical trends of results were also observed for both SR and OSR. Therefore, arguments used for explanation of trends of SR results are equally applicable for OSR.
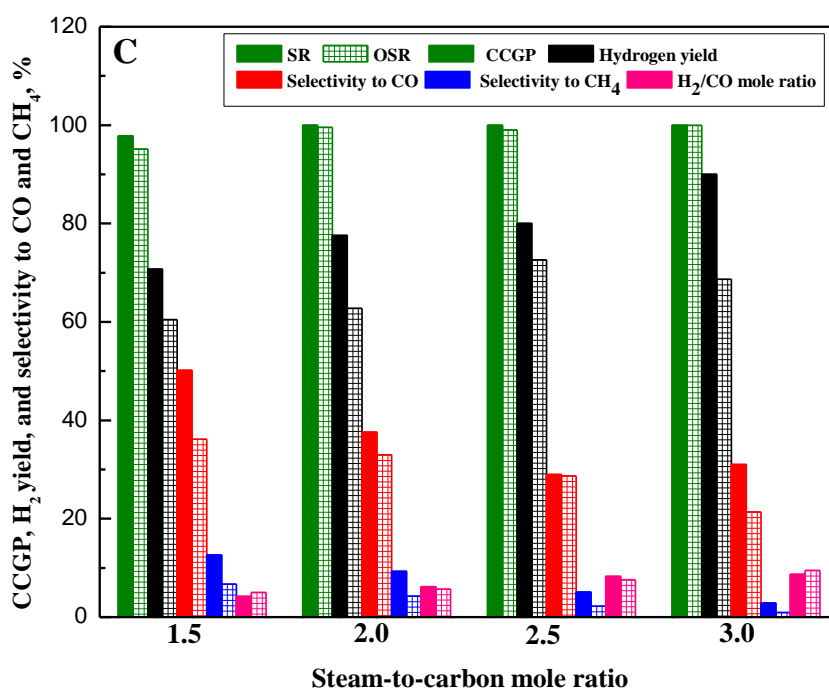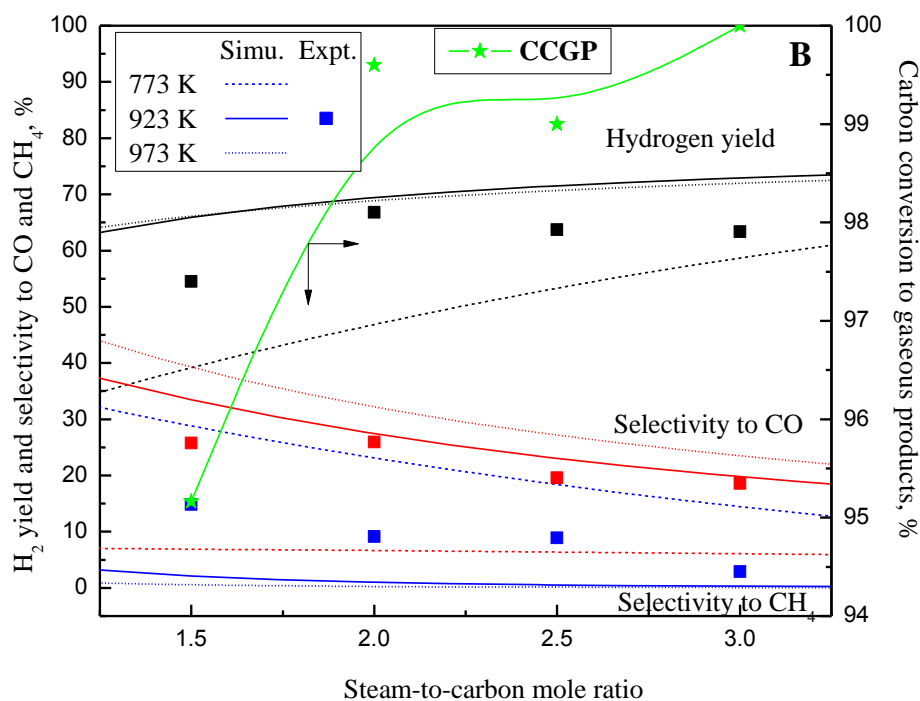
Figure 5.7: Effect of steam-to-carbon mole ratio on hydrogen yield and selectivity to CO and CH$_4$ for A. SR, B. OSR, and C. comparison of SR and OSR of isobutanol. Experimental conditions: 7.3NiAl, 923 K, WHSV= 6.5 h^{-1} (SR) and 7.6 h^{-1} (OSR), CCGP=100% (SR), OCMR=0.8 (OSR).

(79)

The comparisons of experimental SR and OSR results are shown in Figure 5.7C. As observed, CCGP was slightly higher for SR than OSR. The molar flow rate of products in liquid sample was somewhat more in OSR compared to SR (Table 5.2). This was mainly due to incomplete CCGP because of slightly higher WHSV for OSR than SR. However, hydrogen yield and selectivity to CO and CH_4 were lesser for OSR compared to SR as observed from Figure 5.7C. This result indicates that hydrogen, CO, and CH_4 were oxidized by oxygen to water and CO_2 thereby reducing hydrogen yield and selectivity to CO and CH_4. As observed from the figure, H_2/CO mole ratio enhanced with increasing SCMR. The H_2/CO mole ratio was below 5 at SCMR of 1.5 and increased to 10 at SCMR of 3.2. This was mainly because of the fact that hydrogen yield increased and selectivity to CO decreased with increasing SCMR thereby increasing H_2/CO mole ratio. However, H_2/CO mole ratio remained almost same for both SR and OSR.

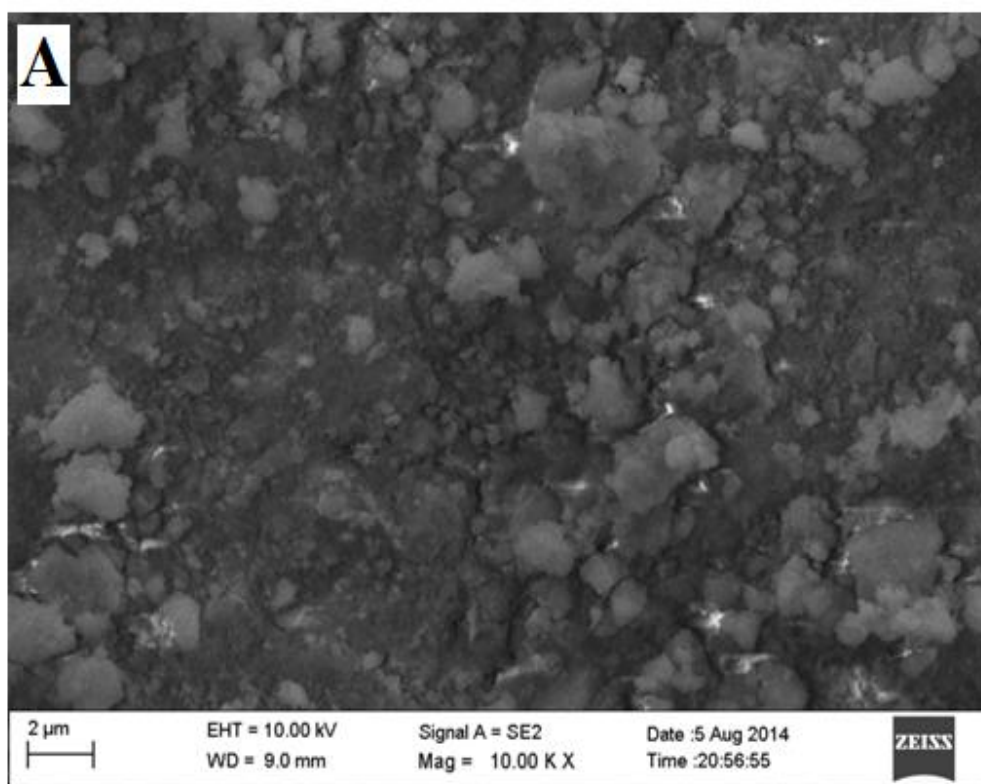### 5.2.6 Spent catalyst characterization

5.2.6.1 Powder XRD

Spent catalysts were characterized by powder XRD for various OCMRs (0 to 2.5) to understand the role of OCMR on chemical changes of supported nickel catalysts during SR and OSR (Figure 5.1). Powder XRD patterns of spent catalysts showed characteristic peaks of nickel (at 2θ of 44.5°, 51.97°, 76.47°, and 92.6°), nickel oxide (at 2θ of 37.37°, 43.2° and 50.85°), and $NiAl_2O_4$ (at 2θ of 37.37° and 66.2°) depending on OCMR. For SR, except the combined peak at 2θ of 37.3° for nickel/nickel oxide, spent 4.3NiAl showed representative peaks of nickel only. The existence of bulk nickel oxide on spent 4.3NiAl for SR thus remained inconclusive. Interestingly, with increasing OCMR, nickel oxide peaks were appeared gradually with concurrent decrease of intensity of nickel peaks. At OCMR= 2.5, only nickel oxide and $NiAl_2O_4$ peaks were observed in spent 4.3NiAl. Moreover, intensity of one signature $NiAl_2O_4$ peak at 2θ of ~66.2° decreased gradually with increasing OCMR for spent 4.3NiAl. These results clearly endorsed that nickel and $NiAl_2O_4$ converted to bulk nickel oxide during OSR. For spent 4.3NiAl, average nickel crystallite size decreased from 15.3 nm to 8.2 nm with increasing OCMR from 0 to 1.7 (Table 5.1). However, average nickel/nickel oxide crystallite sizes remained practically unaffected with increasing OCMR

(80)

for 7.3NiAl. The nickel oxide crystallites were however enlarged in spent catalysts of SR and OSR compared to fresh calcined catalysts.

5.2.6.2 SEM analysis

FESEM images of calcined catalysts and selected spent catalysts are presented in Figure 5.8 and Figure 5.9. A complex criss-cross carbon nano-fibers networks were formed on spent γ-Al_2O_3 supported nickel catalysts for both SR and OSR. These carbon nano-fibers were formed on active metals by decomposition of carbonaceous compounds (Eqs.(vii-x) of **Error! Reference source not found.**) [105]. The carbon nano-fibers networks were denser and bigger in diameter over spent 7.3NiAl than spent 4.3NiAl for both SR and OSR. These results clearly suggested that extents and diameter of carbon nano-fibers increased with increasing nickel crystallite size [106].
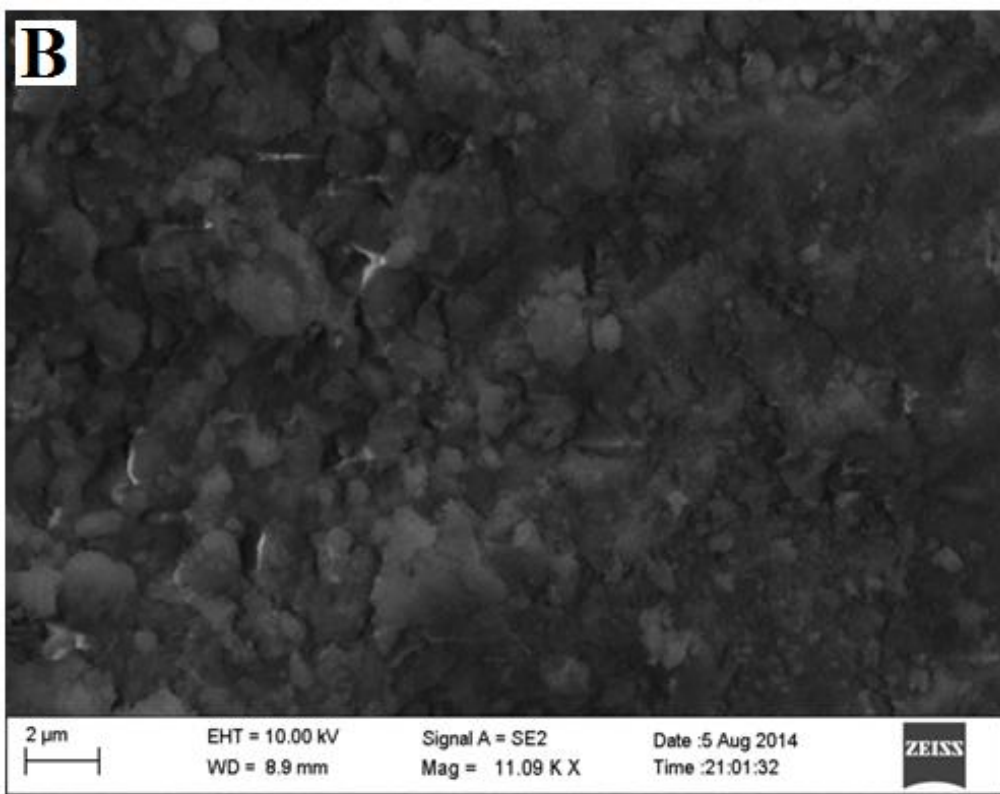
Figure 5.8: SEM images of calcined catalysts. A. 4.3NiAl B. 7.3NiAl.

Pa 1 =117.6 nm
Pb 1 = 90.0^0

Pa R1

Pa 1

| 200 nm | EHT = 20.00 kV | Signal A = InLens | Date :5 Aug 2014 | ZEISS |
| | WD = 8.9 mm | Mag = 50.00 K X | Time :20:38:19 | |

Pa 1

Pa 1 =58.79 nm
Pb 1 = 360.0^0

Pa R1

| 300 nm | EHT = 20.00 kV | Signal A = InLens | Date :5 Aug 2014 | ZEISS |
| | WD = 7.5 mm | Mag = 50.00 K X | Time :19:07:00 | |
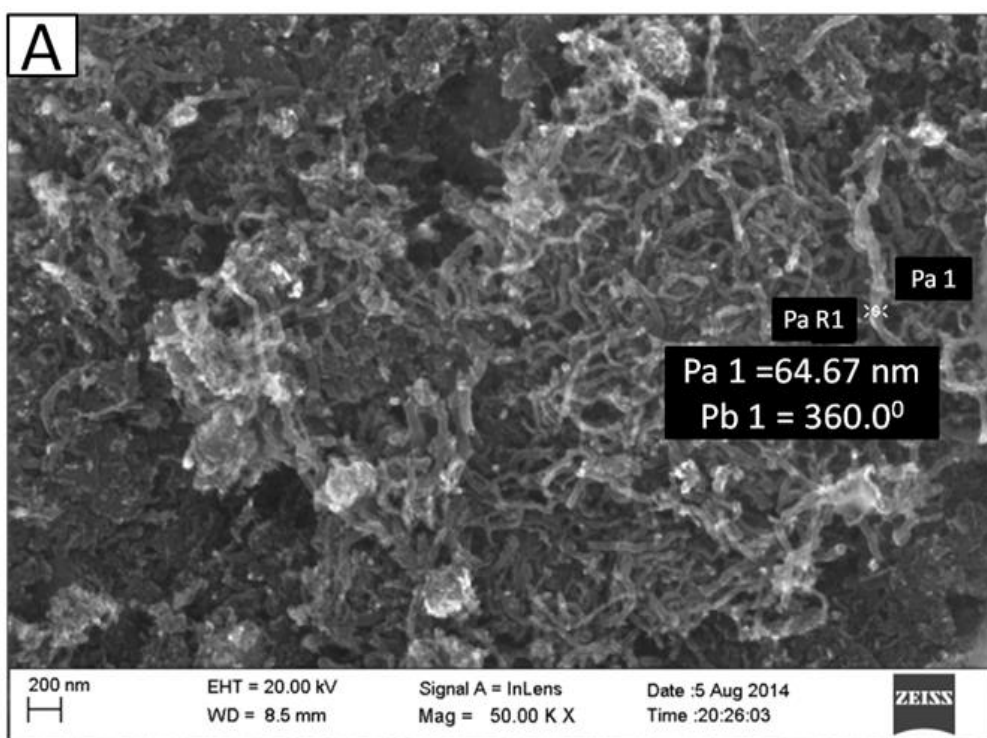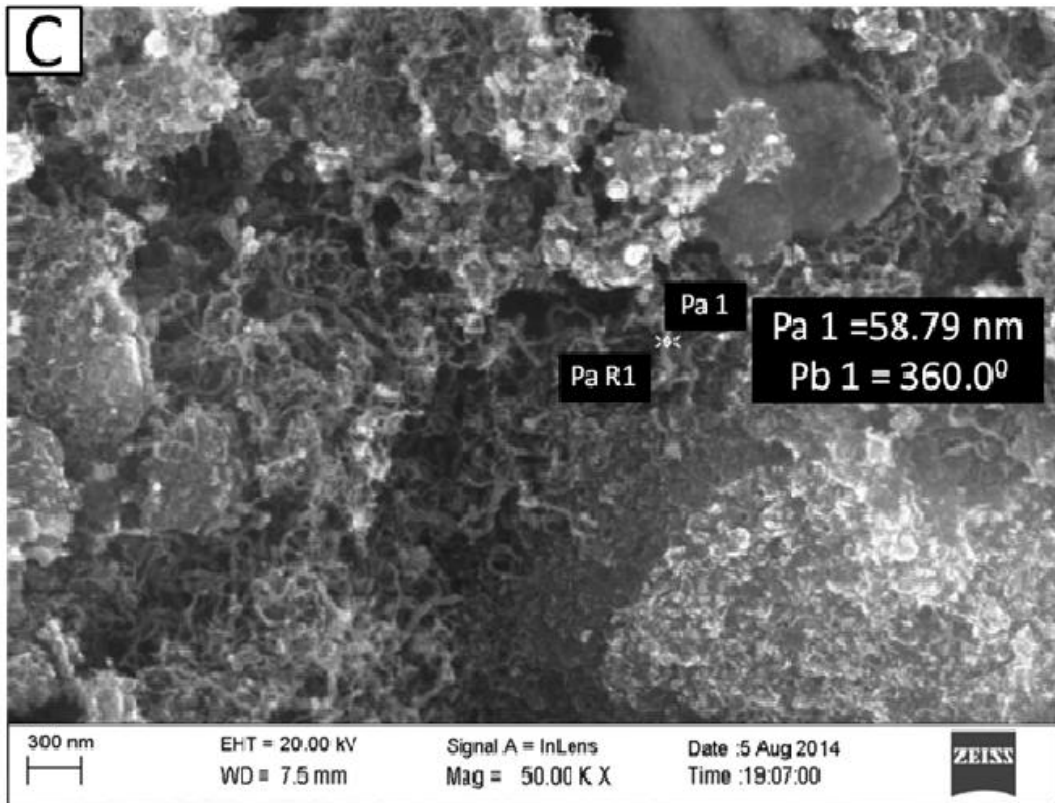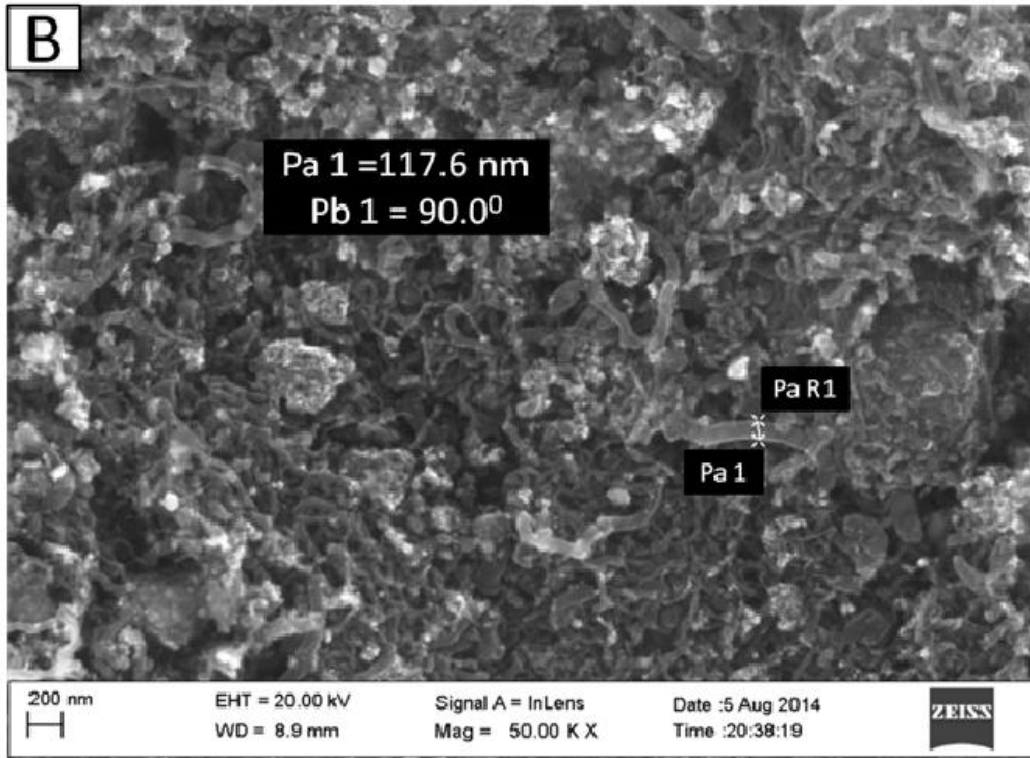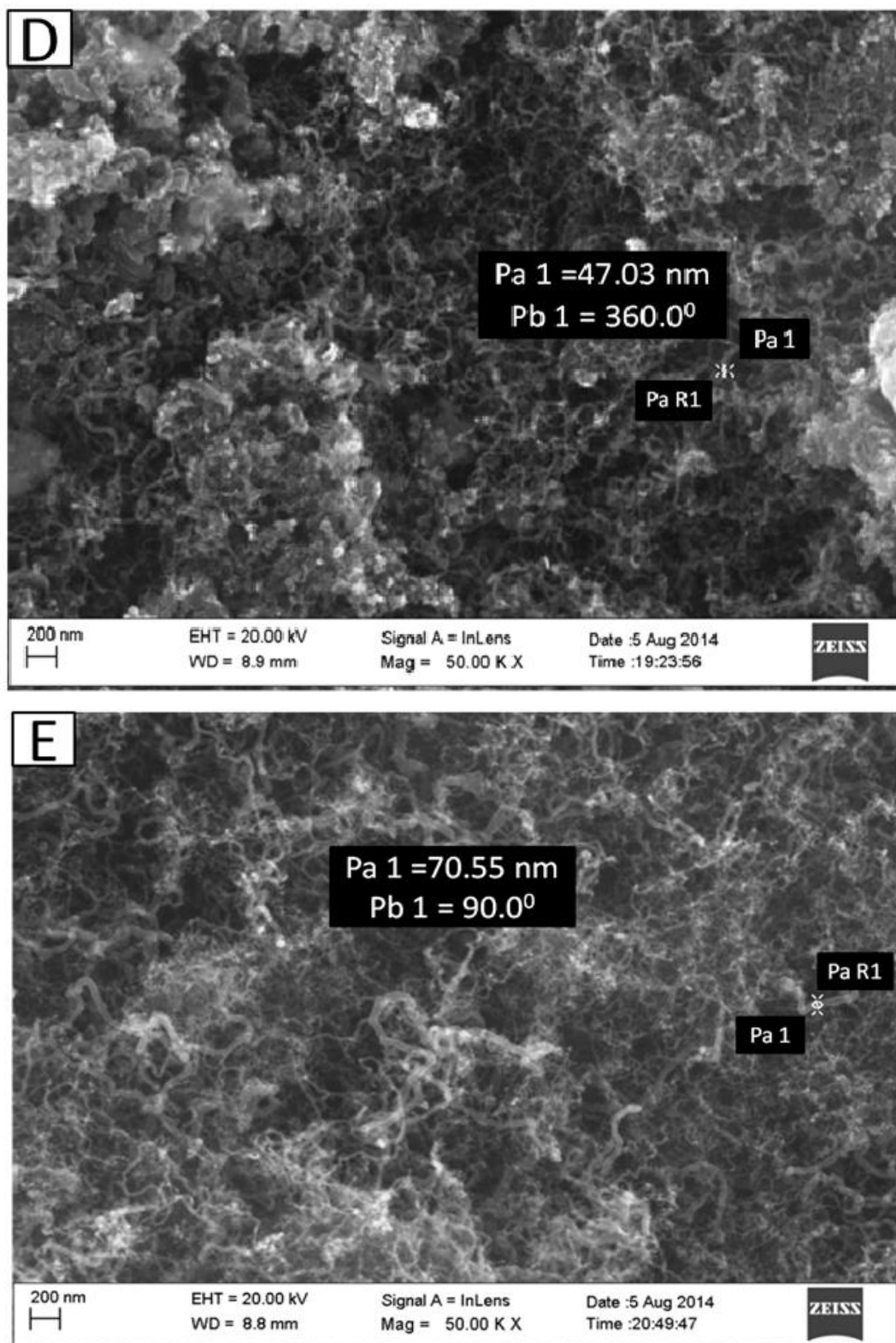
Figure 5.9: SEM images of spent catalysts. A. 4.3NiAl (SR) B. 7.3NiAl (SR) C. 4.3NiAl with OCMR=0.8 D. 4.3NiAl with OCMR=1.7 E. 7.3NiAl with OCMR=0.8.

3μm　　Electron Image 1

3μm　　Electron Image 1

(86)
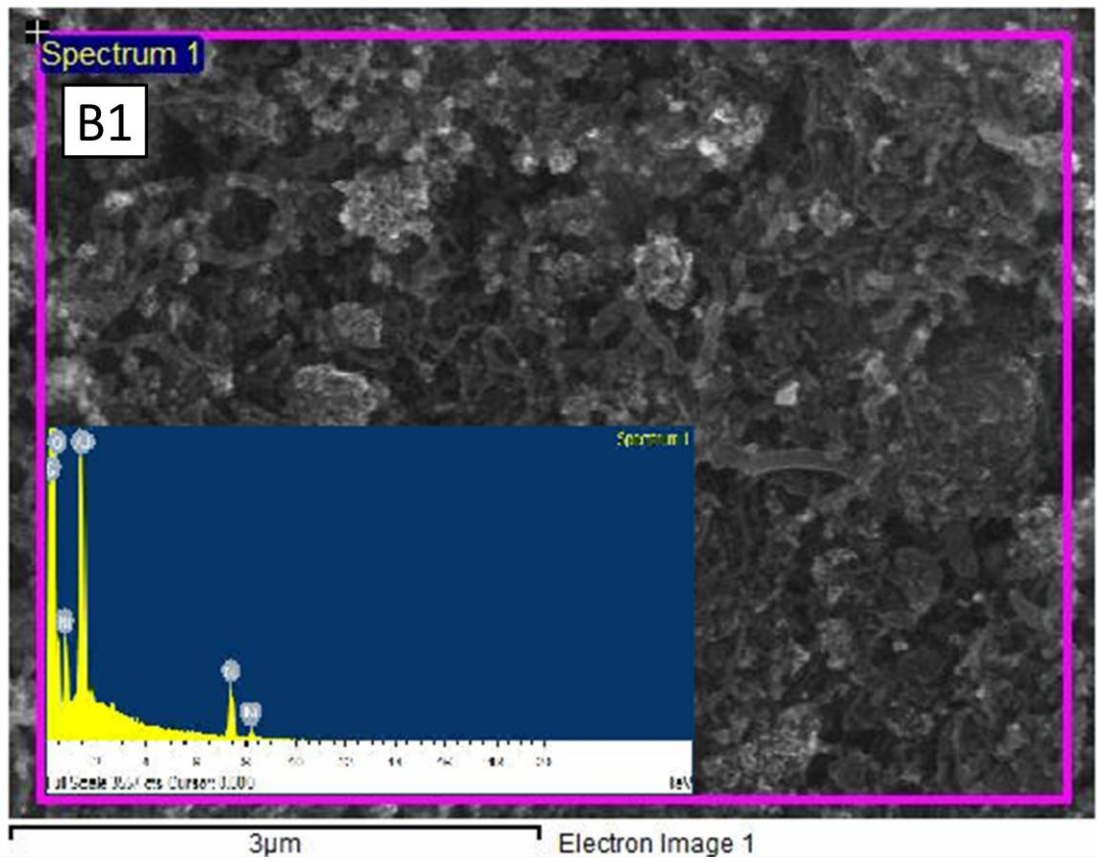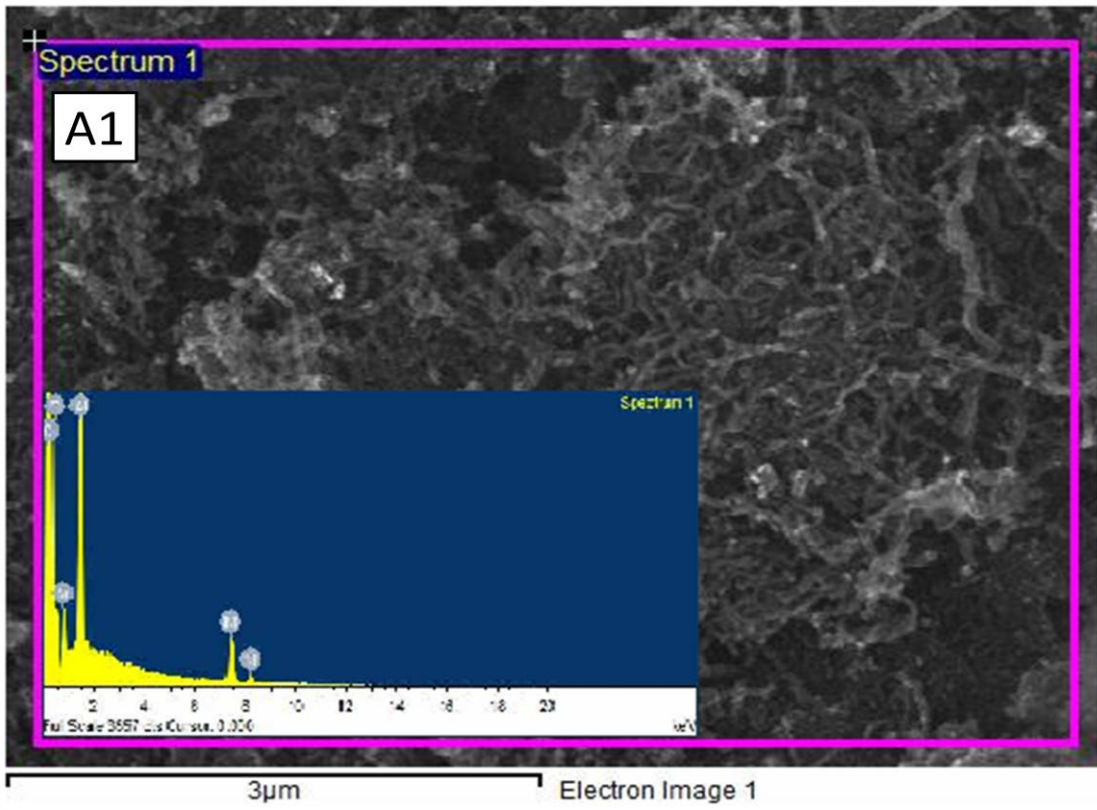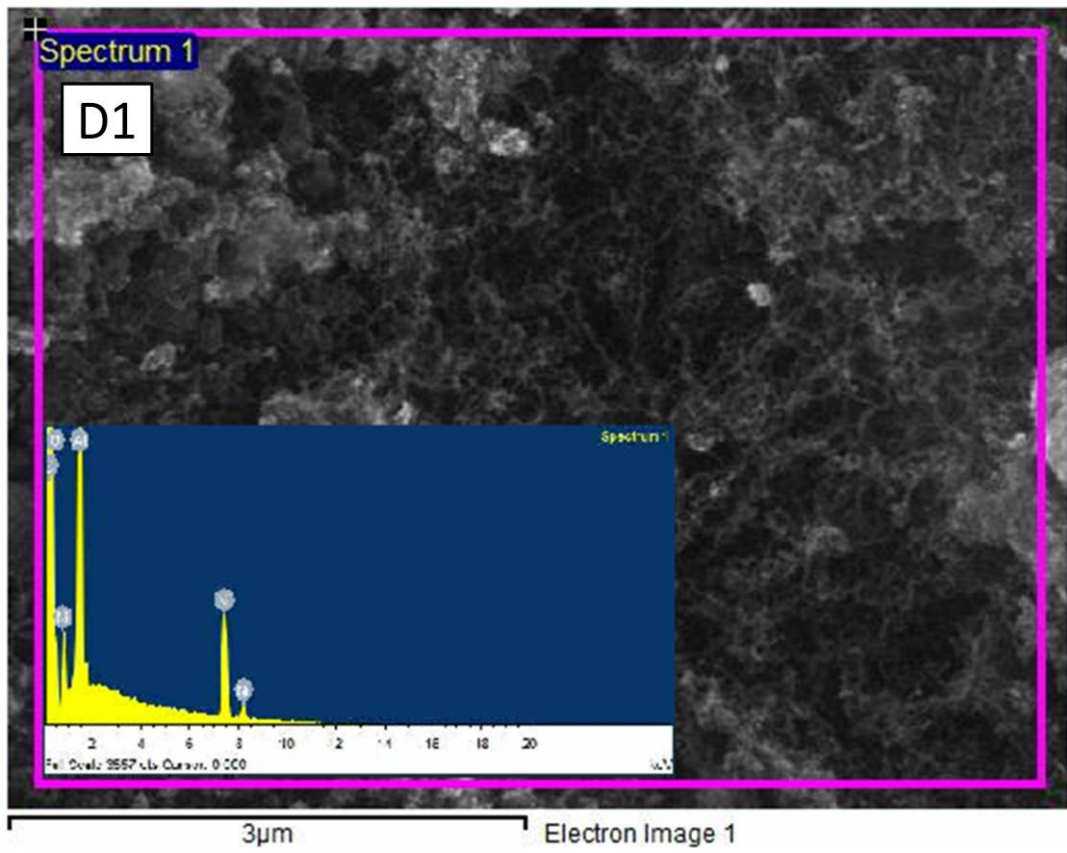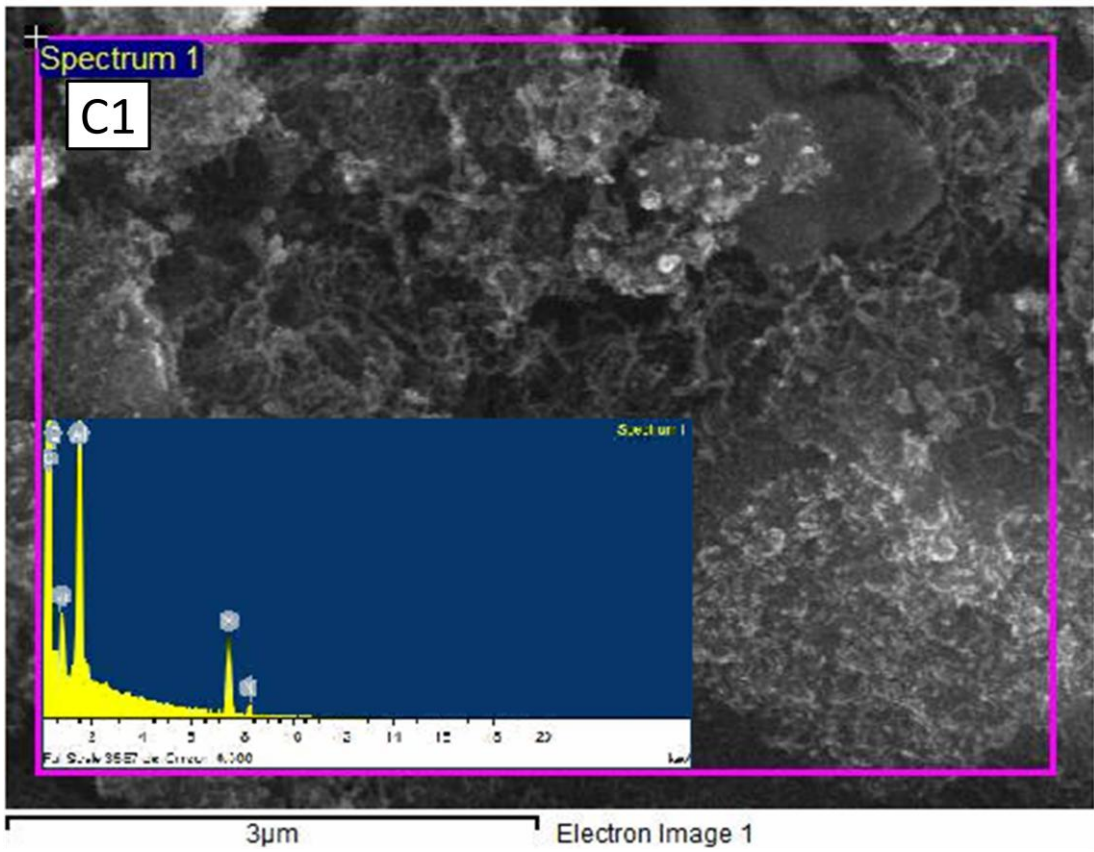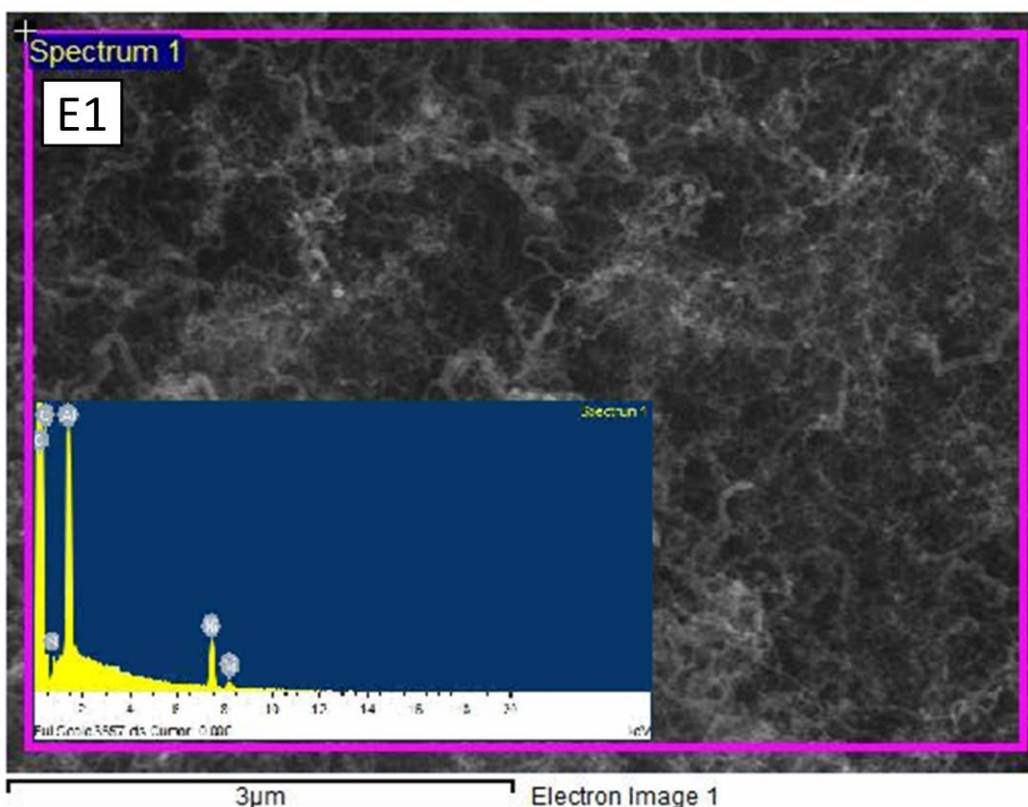
Figure 5.10: EDX spectrum of selected spent catalysts. A1. 4.3NiAl (SR) B1. 7.3NiAl (SR) C1. 4.3NiAl with OCMR=0.8 D1. 4.3NiAl with OCMR=1.7 E1. 7.3NiAl with OCMR=0.8.

Some researchers however reported that diameter of carbon nano-fibers is independent of initial nickel crystallite size and depends mainly on structural transformations during carbon growth process [107,108]. The density of carbon nano-fibers and their diameter were however lesser for OSR compared to SR. The diameter of carbon nano-fibers decreased to 70.5 nm for OSR at 0.8 OCMR from 117.6 nm for SR for spent 7.3NiAl. For spent 4.3NiAl, diameter of carbon nano-fibers was 64.7 nm for SR and decreased to 58.8 nm for OSR at 0.8 OCMR. The diameter of carbon nano-fibers further decreased with increasing OCMR. For OSR over 4.3NiAl, diameter of carbon nano-fibers decreased from 58.8 nm to 47 nm by increasing OCMR from 0.8-1.7. The decrease of diameter of carbon nano-fibers may be due to increased oxidation of carbon deposited on the catalysts at elevated OCMR. The EDX spectrums of the spent catalysts are shown in Figure 5.10.

Chapter 6

Conclusions

The SR and OSR of isobutanol were investigated in a computer controlled down-flow FBR over various supported metal catalysts prepared by incipient wetness impregnation method. The catalysts were characterized by BET, chemisorption, TPR, and powder XRD.

- The nature of metals and supports strongly influenced metal-support interaction which in turn influenced catalytic activity significantly. Higher metal-support interaction promotes activity of catalysts. The 4.3NiAl (~98% CCGP) exhibited highest catalytic activity followed by 4.3NiSi (~88% CCGP), 4.3CoAl (~86% CCGP), 4.3NiZr (~39% CCGP), and 4.3MoAl (~36% CCGP) under identical experimental conditions. The surface oxygen mobility characteristic of zirconia led to slightly lower selectivity to methane and higher hydrogen yield for 4.3NiZr compared to 4.3NiAl and 4.3NiSi. Ni and Co are thus highly active metal and γ-Al_2O_3 is a suitable support for SR of isobutanol.

- The nickel and cobalt supported on γ-Al_2O_3 catalysts were quite stable and active for SR of isobutanol. The detailed study was thus performed to comprehend the effects of various process parameters such as nickel and cobalt loading on γ-Al_2O_3, WHSV, SCMR, and temperature on CCGP, hydrogen yield, and selectivity to CO, CO_2, and methane. The CCGP increased with increasing nickel and cobalt loading on γ-Al_2O_3 and temperature. The hydrogen yield increased with increasing nickel and cobalt loading on γ-Al_2O_3, temperature, and SCMR. The desired low selectivity to methane was favored at higher reaction temperature and SCMR. The selectivity to CO dropped with increasing SCMR and decreasing temperature. The trends of experimental results were found to be in good agreement with thermodynamic equilibrium results. Optimum SR conditions for high hydrogen yield with minimum selectivity to methane were identified as T= 900 K, SCMR= 2.5-3.0.

- The present work further provides comprehensive investigation of OSR and comparisons with SR of isobutanol over γ-Al_2O_3 supported nickel catalysts. The rise of OCMR led to decline of hydrogen yield and selectivity to CO and methane. The hydrogen yield dropped to 68% from 80%; while selectivity to methane reduced to 1.7% from 4.8% with increasing OCMR from 0 to 2.5 at 923 K and SCMR of 2.5. The hydrogen yield and selectivity to CO increased with concurrent decrease of selectivity to methane with rise of temperature for both SR and OSR. With increasing SCMR, hydrogen yield boosted and selectivity to CO and methane reduced for both SR and OSR. The H_2/CO mole ratio was consistent for both SR and OSR and enhanced with increasing SCMR. The H_2/CO mole ratio of 7-8 was obtained at 923 K and SCMR of 2.5. The trends of experimental results displayed good agreements with equilibrium products composition for both SR and OSR. The hydrogen yield and selectivity to CO and methane was however somewhat lesser for OSR compared to SR. Higher oxygen concentrations in the feed showed adverse impact on the hydrogen yield and active component of the catalyst. It was concluded that OCMR of 0.8 was suitable to operate OSR under thermoneutral condition.

- The shape and quantity of carbon formed on spent catalysts depends strongly on nature of metals. The powder XRD patterns of spent catalysts showed that cobalt and molybdenum transformed to oxides form during SR of isobutanol. The powder XRD patterns of spent catalysts exhibited oxidation of nickel to nickel oxide during OSR. The FESEM images of spent catalysts showed that diameter carbon nano-fibers were reduced with increasing OCMR.

Chapter 7

Future scope of work

7.1   Future scope

The present study was focused on SR and OSR of isobutanol on γ-Al_2O_3 supported metal catalysts. The complete conversion of isobutanol to gaseous products was achieved with about 80% hydrogen yield. The deactivation of the catalyst by coke deposition is the primary bottleneck of SR and OSR. To develop highly active coke resistant catalysts for SR and OSR of bio-butanol, further research is thus needed to modify the catalyst support, active components and catalyst preparation methods. The present work can therefore be extended to SR and OSR of bio-butanol over CeO_2-ZrO_2 supported metal catalysts.

7.1.1   SR of bio-butanol over Ni/CeO$_2$-ZrO$_2$ and Ni/Al$_2$O$_3$-CeO$_2$-ZrO$_2$ catalysts

Ceria-zirconia (CZ) solid solution containing (20% ZrO_2 in CeO_2) plays an important role in variety of application in the chemical industry. It facilitates the zero emission of automotive exhaust gas due to its redox properties [109]. Distinctive character of ceria is oxygen storage/release property, i.c. it stores the oxygen in aerobic conditions and releases the oxygen in anaerobic conditions to maintain its stoichiometry by changing its oxidation states between +3 and +4. But, thermal stability characteristics of pure ceria are limited because of the less SA and sintering of crystallites at high temperature. Introduction of rare earth metal oxides like zirconia increases the ionic conductivity of ceria, moves the lattice oxygen from the bulk to surface and lowers the sintering of ceria crystallites. So, CZ solid solution has been considered as the propitious catalyst support for the production of hydrogen. And also, nowadays the third generation alumina-ceria-zirconia is gaining much importance as it overcomes the disadvantages associated with the CZ [110].

7.1.2 SR of bio-butanol over bimetallic Ni-Co/Ni-Mo/Co-Mo supported on Al$_2$O$_3$-CeO$_2$-ZrO$_2$ catalysts

Bimetallic catalysts exhibit specific characteristics depending on the composition which are different from mono metallic catalysts. So, the bimetallic catalysts have been gained much importance in the production of hydrogen because of their enhanced catalytic activity than the mono metallic catalysts [111]. The high SA alumina-ceria-zirconia decreases the coke deposition by its redox behaviour. The bimetallic catalysts increase the catalytic activity by synergistic effect. Further, the OSR of bio-butanol over alumina-ceria-zirconia supported bimetallic catalysts may also decrease the coke deposition even more.

Bibliography

[1]   S. Fernando, S. Adhikari, C. Chandrapal, N. Murali, Biorefineries: Current Status, Challenges, and Future Direction, Energy Fuels. 20 (2006) 1727–1737.

[2]   S.K. Maity, Opportunities, recent trends and challenges of integrated biorefinery: Part I, Renew. Sustain. Energy Rev. 43 (2015) 1427–1445.

[3]   B. Kamm, M. Kamm, Principles of biorefineries, Appl. Microbiol. Biotechnol. 64 (2004) 137–45.

[4]   M. Mascal, Chemicals from biobutanol: technologies and markets, Bio Fuels, Bio Prod. Biorefining. 6 (2012) 483–493.

[5]   M. Kumar, K. Gayen, Developments in biobutanol production: New insights, Appl. Energy. 88 (2011) 1999–2012.

[6]   V. Hönig, M. Kotek, J. Mařík, Use of butanol as a fuel for internal combustion engines, Agron. Res. 12 (2014) 333–340.

[7]   T.A. Milne, R.J. Evans, N. Abatzoglou, Biomass Gasifier "Tars": Their Nature , Formation, and Conversion, NREL. (1998) Available from: http://www.nrel.gov/docs/fy99osti/.

[8]   S.K. Maity, Opportunities, recent trends and challenges of integrated biorefinery: Part II, Renew. Sustain. Energy Rev. 43 (2014) 1446–1466.

[9]   J.G. Speight, The Chemistry and Technology of Petroleum, Fourth edition, CRC Press, 2006.

[10]   P. Dürre, Fermentative production of butanol — the academic perspective, Curr. Opin. Biotechnol. 22 (2011) 331–336.

[11] R. Kolodziej, J. Scheib, Bio-isobutanol : The next-generation biofuel, Hydrocarb. Process. (2012) 79–85.

[12] J. Urano, Second-Generation Isobutanol Producing Biocatalyst, (2008) 24.

[13] P. Biswas, D. Kunzru, Steam reforming of ethanol for production of hydrogen over Ni/CeO$_2$–ZrO$_2$ catalyst: Effect of support and metal loading, Int. J. Hydrogen Energy. 32 (2007) 969–980.

[14] N. Laosiripojana, S. Assabumrungrat, Catalytic steam reforming of methane, methanol, and ethanol over Ni/YSZ: The possible use of these fuels in internal reforming SOFC, J. Power Sources. 163 (2007) 943–951.

[15] J.D.A. Bellido, E.M. Assaf, Nickel catalysts supported on ZrO$_2$, Y$_2$O$_3$-stabilized ZrO$_2$ and CaO-stabilized ZrO$_2$ for the steam reforming of ethanol: Effect of the support and nickel load, J. Power Sources. 177 (2008) 24–32.

[16] W. Xu, Z. Liu, A.C. Johnston-Peck, S.D. Senanayake, G. Zhou, D. Stacchiola, et al., Steam Reforming of Ethanol on Ni/CeO$_2$: Reaction Pathway and Interaction between Ni and the CeO$_2$ Support, ACS Catal. 3 (2013) 975–984.

[17] H. Inokawa, S. Nishimoto, Y. Kameshima, M. Miyake, Difference in the catalytic activity of transition metals and their cations loaded in zeolite Y for ethanol steam reforming, Int. J. Hydrogen Energy. 35 (2010) 11719–11724.

[18] Y. Yang, J. Ma, F. Wu, Production of hydrogen by steam reforming of ethanol over a Ni/ZnO catalyst, Int. J. Hydrogen Energy. 31 (2006) 877–882.

[19] C. Zhang, H. Yue, Z. Huang, S. Li, G. Wu, X. Ma, et al., Hydrogen Production via Steam Reforming of Ethanol on Phyllosilicate-Derived Ni/SiO$_2$: Enhanced Metal−Support Interaction and Catalytic Stability, ACS Sustain. Chem. Eng. 1 (2013) 161−173.

[20] S. Li, C. Zhang, Z. Huang, G. Wu, J. Gong, A Ni@ZrO$_2$ nanocomposite for ethanol steam reforming: enhanced stability via strong metal-oxide interaction., Chem. Commun. 49 (2013) 4226–4228.

[21] L.P.R. Profeti, J.A.C. Dias, J.M. Assaf, E.M. Assaf, Hydrogen production by steam reforming of ethanol over Ni-based catalysts promoted with noble metals, J. Power Sources. 190 (2009) 525–533.

[22] R. Buitrago-Sierra, J. Ruiz-Martínez, J.C. Serrano-Ruiz, F. Rodríguez-Reinoso, A. Sepúlveda-Escribano, Ethanol steam reforming on Ni/Al_2O_3 catalysts: effect of the addition of Zn and Pt., J. Colloid Interface Sci. 383 (2012) 148–154.

[23] C.K.S. Choong, Z. Zhong, L. Huang, Z. Wang, T.P. Ang, A. Borgna, et al., Effect of calcium addition on catalytic ethanol steam reforming of Ni/Al_2O_3: I. Catalytic stability, electronic properties and coking mechanism, Appl. Catal. A Gen. 407 (2011) 145–154.

[24] I.P. Hernández, Y. Gochi-Ponce, J.L. Contreras Larios, a. M. Fernández, Steam reforming of ethanol over nickel-tungsten catalyst, Int. J. Hydrogen Energy. 35 (2010) 12098–12104.

[25] K.F.M. Elias, A.F. Lucrédio, E.M. Assaf, Effect of CaO addition on acid properties of $Ni–Ca/Al_2O_3$ catalysts applied to ethanol steam reforming, Int. J. Hydrogen Energy. 38 (2013) 4407–4417.

[26] V.V. Galvita, G.L. Semin, V.D. Belyaev, V.A. Semikolenov, P. Tsiakaras, V.A. Sobyanin, Synthesis gas production by steam reforming of ethanol, Appl. Catal. A Gen. 220 (2001) 123–127.

[27] F. Wang, Y. Li, W. Cai, E. Zhan, X. Mu, W. Shen, Ethanol steam reforming over Ni and Ni–Cu catalysts, Catal. Today. 146 (2009) 31–36.

[28] F.J. Mariño, E.G. Cerrella, S. Duhalde, M. Jobbagy, M.A. Laborde, Hydrogen from steam reforming of ethanol. characterization and performance of copper-nickel supported catalysts, Int. J. Hydrogen Energy. 23 (1998) 1095–1101.

[29] N. Homs, J. Llorca, P.R. de la Piscina, Low-temperature steam-reforming of ethanol over ZnO-supported Ni and Cu catalysts The effect of nickel and copper addition to ZnO-supported cobalt-based catalysts, Catal. Today. 116 (2006) 361–366.

[30] A.J. Vizcaíno, A. Carrero, J.A. Calles, Hydrogen production by ethanol steam reforming over Cu–Ni supported catalysts, Int. J. Hydrogen Energy. 32 (2007) 1450–1461.

[31] A. Carrero, J.A. Calles, A.J. Vizcaíno, Effect of Mg and Ca addition on coke deposition over Cu–Ni/SiO2 catalysts for ethanol steam reforming, Chem. Eng. J. 163 (2010) 395–402.

[32] A.J. Vizcaíno, A. Carrero, J.A. Calles, Ethanol steam reforming on Mg- and Ca-modified Cu–Ni/SBA-15 catalysts, Catal. Today. 146 (2009) 63–70.

[33] B. Zhang, W. Cai, Y. Li, Y. Xu, W. Shen, Hydrogen production by steam reforming of ethanol over an Ir/CeO_2 catalyst: Reaction mechanism and stability of the catalyst, Int. J. Hydrogen Energy. 33 (2008) 4377–4386.

[34] P. Biswas, D. Kunzru, Steam reforming of ethanol on $Ni–CeO_2–ZrO_2$ catalysts: Effect of doping with copper, cobalt and calcium, Catal. Letters. 118 (2007) 36–49.

[35] M. Ni, D.Y.C. Leung, M.K.H. Leung, A review on reforming bio-ethanol for hydrogen production, Int. J. Hydrogen Energy. 32 (2007) 3238–3247.

[36] M. Patel, T.K. Jindal, K.K. Pant, Kinetic Study of Steam Reforming of Ethanol on Ni-Based Ceria−Zirconia Catalyst, Ind. Eng. Chem. Res. 52 (2013) 15763–15771.

[37] B.A. Peppley, J.C. Amphlett, L.M. Kearns, R.F. Mann, Methanol—steam reforming on $Cu/ZnO/Al_2O_3$. Part 1: the reaction network, Appl. Catal. A Gen. 179 (1999) 21–29.

[38] C. Cao, G. Xia, J. Holladay, E. Jones, Y. Wang, Kinetic studies of methanol steam reforming over Pd/ZnO catalyst using a microchannel reactor, Appl. Catal. A Gen. 262 (2004) 19–29.

[39] R.O. Idem, N.N. Bakhshi, Production of Hydrogen from Methanol over Promoted Coprecipitated Cu-Al Catalysts: The Effects of Various Promoters and Catalyst Activation Methods, Ind. Eng. Chem. Res. 34 (1995) 1548–1557.

[40] B. Lindström, L.J. Pettersson, Hydrogen generation by steam reforming of methanol over copper-based catalysts for fuel cell applications, Int. J. Hydrogen Energy. 26 (2001) 923–933.

[41] S. Sá, J.M. Sousa, A. Mendes, Steam reforming of methanol over a $CuO/ZnO/Al_2O_3$ catalyst, part I: Kinetic modelling, Chem. Eng. Sci. 66 (2011) 4913–4921.

[42] H.-M. Yang, P.-H. Liao, Preparation and activity of Cu/ZnO-CNTs nano-catalyst on steam reforming of methanol, Appl. Catal. A Gen. 317 (2007) 226–233.

[43] H. Purnama, F. Girgsdies, T. Ressler, J.H. Schattka, R.A. Caruso, R. Schomäcker, et al., Activity and selectivity of a nanostructured CuO/ZrO_2 catalyst in the steam reforming of methanol, Catal. Letters. 94 (2004) 61–68.

[44] S. Sá, H. Silva, L. Brandão, J.M. Sousa, A. Mendes, Catalysts for methanol steam reforming—A review, Appl. Catal. B Environ. 99 (2010) 43–57.

[45] D.R. Palo, R.A. Dagle, J.D. Holladay, Methanol steam reforming for hydrogen production., Chem. Rev. 107 (2007) 3992–4021.

[46] G.-S. Wu, D.-S. Mao, G.-Z. Lu, Y. Cao, K.-N. Fan, The Role of the Promoters in Cu Based Catalysts for Methanol Steam Reforming, Catal. Letters. 130 (2009) 177–184.

[47] R.J. Galdámez, L. García, R. Bilbao, Hydrogen Production by Steam Reforming of Bio-Oil Using Coprecipitated Ni - Al Catalysts. Acetic Acid as a Model Compound, Energy Fuels. 19 (2005) 1133–1142.

[48] L. An, C. Dong, Y. Yang, J. Zhang, L. He, The influence of Ni loading on coke formation in steam reforming of acetic acid, Renew. Energy. 36 (2011) 930–935.

[49] S. Thaicharoensutcharittham, V. Meeyoo, B. Kitiyanan, P. Rangsunvigit, T. Rirksomboon, Hydrogen production by steam reforming of acetic acid over Ni-based catalysts, Catal. Today. 164 (2011) 257–261.

[50] M. Patel, K.K. Pant, P. Mohanty, Renewable Hydrogen Generation by Steam Reforming of Acetic Acid over Cu-Zn-Ni Supported Calcium Aluminate Catalysts, Nanocatalysis Fuels Chem. 9 (2012) 111–137.

[51] P. Mohanty, M. Patel, K.K. Pant, Hydrogen production from steam reforming of acetic acid over Cu–Zn supported calcium aluminate, Bioresour. Technol. 123 (2012) 558–565.

[52] N. Goyal, K.K. Pant, R. Gupta, Hydrogen production by steam reforming of model bio-oil using structured Ni/Al$_2$O$_3$ catalysts, Int. J. Hydrogen Energy. 38 (2013) 921–933.

[53] K.K. Pant, P. Mohanty, S. Agarwal, A.K. Dalai, Steam reforming of acetic acid for hydrogen production over bifunctional Ni–Co catalysts, Catal. Today. 207 (2013) 36–43.

[54] N. Wang, N. Perret, A. Foster, Sustainable hydrogen production for fuel cells by steam reforming of ethylene glycol: A consideration of reaction thermodynamics, Int. J. Hydrogen Energy. 36 (2011) 5932–5940.

[55] K. Takeishi, H. Suzuki, Steam reforming of dimethyl ether, Appl. Catal. A Gen. 260 (2004) 111–117.

[56] M.C. Ramos, A.I. Navascués, L. Gracía, R. Bilbao, Hydrogen Production by Catalytic Steam Reforming of Acetol, a Model Compound of Bio-Oil, Ind. Eng. Chem. Res. 46 (2007) 2399–2406.

[57] C. Wu, R. Liu, Hydrogen Production from Steam Reforming of m-Cresol, a Model Compound Derived from Bio-oil: Green Process Evaluation Based on Liquid Condensate Recycling, Energy Fuels. 24 (2010) 5139–5147.

[58] X. Hu, G. Lu, Investigation of the steam reforming of a series of model compounds derived from bio-oil for hydrogen production, Appl. Catal. B Environ. 88 (2009) 376–385.

[59] P.D. Vaidya, A.E. Rodrigues, Glycerol Reforming for Hydrogen Production: A Review, Chem. Eng. Technol. 32 (2009) 1463–1469.

[60] C.D. Dave, K.K. Pant, Renewable hydrogen generation by steam reforming of glycerol over zirconia promoted ceria supported catalyst, Renew. Energy. 36 (2011) 3195–3202.

[61] C.M. Jeong, G.W. Park, J. Choi, J.W. Kang, S.M. Kim, W.-H. Lee, et al., Steam reforming of volatile fatty acids (VFAs) over supported Pt/Al_2O_3 catalysts, Int. J. Hydrogen Energy. 36 (2011) 7505–7515.

[62] M. Marquevich, R. Coll, D. Montané, Steam Reforming of Sunflower Oil for Hydrogen Production., Ind. Eng. Chem. Res. 39 (2000) 2140–2147.

[63] M. Marquevich, X. Farriol, F. Medina, D. Montané, Hydrogen Production by Steam Reforming of Vegetable Oils Using Nickel-Based Catalysts, Ind. Eng. Chem. Res. 40 (2001) 4757–4766.

[64] G.A. Nahar, S.S. Madhani, Thermodynamics of hydrogen production by the steam reforming of butanol: Analysis of inorganic gases and light hydrocarbons, Int. J. Hydrogen Energy. 35 (2010) 98–109.

[65] W. Wang, Hydrogen production via dry reforming of butanol: Thermodynamic analysis, Fuel. 90 (2011) 1681–1688.

[66] A.L.D. Silva, I.L. Müller, Hydrogen production by sorption enhanced steam reforming of oxygenated hydrocarbons (ethanol, glycerol, n-butanol and methanol): Thermodynamic modelling, Int. J. Hydrogen Energy. 36 (2011) 2057–2075.

[67] W. Wang, Y. Cao, Hydrogen production via sorption enhanced steam reforming of butanol: Thermodynamic analysis, Int. J. Hydrogen Energy. 36 (2011) 2887–2895.

[68] W. Wang, Y. Cao, Hydrogen-rich gas production for solid oxide fuel cell (SOFC) via partial oxidation of butanol: Thermodynamic analysis, Int. J. Hydrogen Energy. 35 (2010) 13280–13289.

[69] F. Bimbela, M. Oliva, J. Ruiz, L. García, J. Arauzo, Catalytic steam reforming of model compounds of biomass pyrolysis liquids in fixed bed: Acetol and n-butanol, J. Anal. Appl. Pyrolysis. 85 (2009) 204–213.

[70] F. Bimbela, D. Chen, J. Ruiz, L. García, J. Arauzo, Ni/Al coprecipitated catalysts modified with magnesium and copper for the catalytic steam reforming of model compounds from biomass pyrolysis liquids, Appl. Catal. B Environ. 119-120 (2012) 1–12.

[71] B. Roy, H. Sullivan, C.A. Leclerc, Effect of variable conditions on steam reforming and aqueous phase reforming of n-butanol over Ni/CeO_2 and Ni/Al_2O_3 catalysts, J. Power Sources. 267 (2014) 280–287.

[72] W. Cai, P.R. de la Piscina, N. Homs, Hydrogen production from the steam reforming of bio-butanol over novel supported Co-based bimetallic catalysts., Bioresour. Technol. 107 (2012) 482–486.

[73] W. Cai, N. Homs, P.R. de la Piscina, Efficient hydrogen production from bio-butanol oxidative steam reforming over bimetallic Co–Ir/ZnO catalysts, Green Chem. 14 (2012) 1035–1043.

[74] W. Cai, P.R. de la Piscina, K. Gabrowska, N. Homs, Hydrogen production from oxidative steam reforming of bio-butanol over CoIr-based catalysts: effect of the support., Bioresour. Technol. 128 (2013) 467–471.

[75] W. Cai, P.R. de la Piscina, N. Homs, Oxidative steam reforming of bio-butanol for hydrogen production: effects of noble metals on bimetallic CoM/ZnO catalysts (M=Ru, Rh, Ir, Pd), Appl. Catal. B Environ. 145 (2014) 56–62.

[76] W. Cai, N. Homs, P.R. de la Piscina, Renewable hydrogen production from oxidative steam reforming of bio-butanol over $CoIr/CeZrO_2$ catalysts: Relationship between catalytic behaviour and catalyst structure, Appl. Catal. B Environ. 150-151 (2014) 47–56.

[77] R. Chakrabarti, J.S. Kruger, R.J. Hermann, L.D. Schmidt, Autothermal reforming of isobutanol, RSC Adv. 2 (2012) 2527–2533.

[78] I.C. Lee, J.G. St. Clair, A.S. Gamson, Catalytic partial oxidation of isobutanol for the production of hydrogen, Int. J. Hydrogen Energy. 37 (2012) 1399–1408.

[79] M. Fadoni, L. Lucarelli, Temperature programmed desorption , reduction , oxidation and flow chemisorption for the characterisation of heterogeneous catalysts . Theoretical aspects , instrumentation and applications, (n.d.) 1–45.

[80] K. Nakai, K. Nakamura, Pulse chemisorption measurement <Metal dispersion measurement> 6, Adsorpt. J. Int. Adsorpt. Soc. (2003) 1–6.

[81] J.D. Holladay, J. Hu, D.L. King, Y. Wang, An overview of hydrogen production technologies, Catal. Today. 139 (2009) 244–260.

[82] S.R. Yenumala, S.K. Maity, Reforming of vegetable oil for production of hydrogen: A thermodynamic analysis, Int. J. Hydrogen Energy. 36 (2011) 11666–11675.

[83] S.R. Yenumala, S.K. Maity, Thermodynamic evaluation of dry reforming of vegetable oils for production of synthesis gas, J. Renew. Sustain. Energy. 4 (2012) 043120.

[84] M. Benito, R. Padilla, L. Rodríguez, J.L. Sanz, L. Daza, Zirconia supported catalysts for bioethanol steam reforming: Effect of active phase and zirconia structure, J. Power Sources. 169 (2007) 167–176.

[85] L. Wang, D. Li, M. Koike, H. Watanabe, Y. Xu, Y. Nakagawa, et al., Catalytic performance and characterization of Ni–Co catalysts for the steam reforming of biomass tar to synthesis gas, Fuel. 112 (2013) 654–661.

[86] H. Vantbilk, Characterization of supported cobalt and cobalt-rhodium catalysts I. Temperature-programmed reduction (TPR) and oxidation (TPO) of Co-Rh/Al$_2$O$_3$, J. Catal. 97 (1986) 188–199.

[87] V.A.D.L.P. O'shea, R. Nafria, P.R. de la Piscina, N. Homs, Development of robust Co-based catalysts for the selective H$_2$-production by ethanol steam-reforming. The Fe-promoter effect, Int. J. Hydrogen Energy. 33 (2008) 3601–3606.

[88] J. Zhu, X. Peng, L. Yao, J. Shen, D. Tong, C. Hu, The promoting effect of La, Mg, Co and Zn on the activity and stability of Ni/SiO$_2$ catalyst for CO$_2$ reforming of methane, Int. J. Hydrogen Energy. 36 (2011) 7094–7104.

[89] B.M. Güell, I. Babich, K.P. Nichols, J.G.E. Gardeniers, L. Lefferts, K. Seshan, Design of a stable steam reforming catalyst—A promising route to sustainable hydrogen from biomass oxygenates, Appl. Catal. B Environ. 90 (2009) 38–44.

[90] A.L. Alberton, M.M.V.M. Souza, M. Schmal, Carbon formation and its influence on ethanol steam reforming over Ni/Al$_2$O$_3$ catalysts, Catal. Today. 123 (2007) 257–264.

[91] X. Hu, G. Lu, Comparative study of alumina-supported transition metal catalysts for hydrogen generation by steam reforming of acetic acid, Appl. Catal. B Environ. 99 (2010) 289–297.

[92] J. Vicente, C. Montero, J. Ereña, M.J. Azkoiti, J. Bilbao, A.G. Gayubo, Coke deactivation of Ni and Co catalysts in ethanol steam reforming at mild temperatures in a fluidized bed reactor, Int. J. Hydrogen Energy. 39 (2014) 12586–12596.

[93] I.E. Achouri, N. Abatzoglou, C. Fauteux-Lefebvre, N. Braidy, Diesel steam reforming: Comparison of two nickel aluminate catalysts prepared by wet-impregnation and co-precipitation, Catal. Today. 207 (2013) 13–20.

[94] M.N. Barroso, A.E. Galetti, M.C. Abello, Ni catalysts supported over MgAl$_2$O$_4$ modified with Pr for hydrogen production from ethanol steam reforming, Appl. Catal. A Gen. 394 (2011) 124–131.

[95] G. Garbarino, P. Riani, M.A. Lucchini, F. Canepa, S. Kawale, G. Busca, Cobalt-based nanoparticles as catalysts for low temperature hydrogen production by ethanol steam reforming, Int. J. Hydrogen Energy. 38 (2013) 82–91.

[96] D. Shee, G. Deo, Adsorption and ODH reaction of alkane on sol–gel synthesized TiO$_2$–WO$_3$ supported vanadium oxide catalysts: In situ DRIFT and structure–reactivity study, J. Mol. Catal. A Chem. 308 (2009) 46–55.

[97] D. Shee, A. Sayari, Light alkane dehydrogenation over mesoporous Cr$_2$O$_3$/Al$_2$O$_3$ catalysts, Appl. Catal. A Gen. 389 (2010) 155–164.

[98] R.B.C.P. D, Determining Volatiles in Polyethylene Terephthalate Using the Q5000 IR Thermogravimetric Analyzer, (n.d.) 1–6.

[99] A.J. Akande, R.O. Idem, A.K. Dalai, Synthesis, characterization and performance evaluation of Ni/Al$_2$O$_3$ catalysts for reforming of crude ethanol for hydrogen production, Appl. Catal. A Gen. 287 (2005) 159–175.

[100] P. Biswas, D. Kunzru, Oxidative steam reforming of ethanol over Ni/CeO$_2$-ZrO$_2$ catalyst, Chem. Eng. J. 136 (2008) 41–49.

[101] J.G. Seo, M.H. Youn, Y. Bang, I.K. Song, Effect of Ni/Al atomic ratio of mesoporous Ni–Al$_2$O$_3$ aerogel catalysts on their catalytic activity for hydrogen production by steam reforming of liquefied natural gas (LNG), Int. J. Hydrogen Energy. 35 (2010) 12174–12181.

[102] N.R. Peela, D. Kunzru, Oxidative steam reforming of ethanol over Rh based catalysts in a micro-channel reactor, Int. J. Hydrogen Energy. 36 (2011) 3384–3396.

[103] N. Srisiriwat, S. Therdthianwong, A. Therdthianwong, Oxidative steam reforming of ethanol over Ni/Al$_2$O$_3$ catalysts promoted by CeO$_2$, ZrO$_2$ and CeO$_2$–ZrO$_2$, Int. J. Hydrogen Energy. 34 (2009) 2224–2234.

[104] P.N. Kechagiopoulos, S.S. Voutetakis, A.A. Lemonidou, I.A. Vasalos, Hydrogen Production via Steam Reforming of the Aqueous Phase of Bio-Oil in a Fixed Bed Reactor, Energy Fuels. 20 (2006) 2155–2163.

[105] M.L. Toebes, J.H. Bitter, A. Jos Van Dillen, K.P. de Jong, Impact of the structure and reactivity of nickel particles on the catalytic growth of carbon nanofibers, Catal. Today. 76 (2002) 33–42.

[106] M.A. Nieva, M.M. Villaverde, A. Monzón, T.F. Garetto, A.J. Marchi, Steam-methane reforming at low temperature on nickel-based catalysts, Chem. Eng. J. 235 (2014) 158–166.

[107] N. Jeong, J. Lee, Growth of filamentous carbon by decomposition of ethanol on nickel foam: Influence of synthesis conditions and catalytic nanoparticles on growth yield and mechanism, J. Catal. 260 (2008) 217–226.

[108] C. Pham-Huu, R. Vieira, B. Louis, A. Carvalho, J. Amadou, T. Dintzer, et al., About the octopus-like growth mechanism of carbon nanofibers over graphite supported nickel catalyst, J. Catal. 240 (2006) 194–202.

[109] M. Pudukudy, Z. Yaakob, Catalytic aspects of ceria-zirconia solid solution: Part-I An update in the synthesis, properties and chemical reactions of ceria zirconia solid solution, Der Pharma Chem. 6 (2014) 188–216.

[110] H. Sobukawa, Development of Ceria-Zirconia Solid Solutions and Future Trends, R&D Rev. Toyota CRDL. 37 (2002) 1–5.

[111] Z. Wei, J. Sun, Y. Li, A.K. Datye, Y. Wang, Bimetallic catalysts for hydrogen generation., Chem. Soc. Rev. 41 (2012) 7994–8008.